SLD DESIGN REPORT

In the spring of 1983, *SLAC* and its Experimental Policy Advisory Committee *(EPAC)* endorsed the concept of building a *LEP*-competitive detector for installation at the *SLAC* Linear Collider in 1988. This new detector should follow the upgraded *PEP* detector, the Mark II, which will have been exploiting the early physics at the collider.
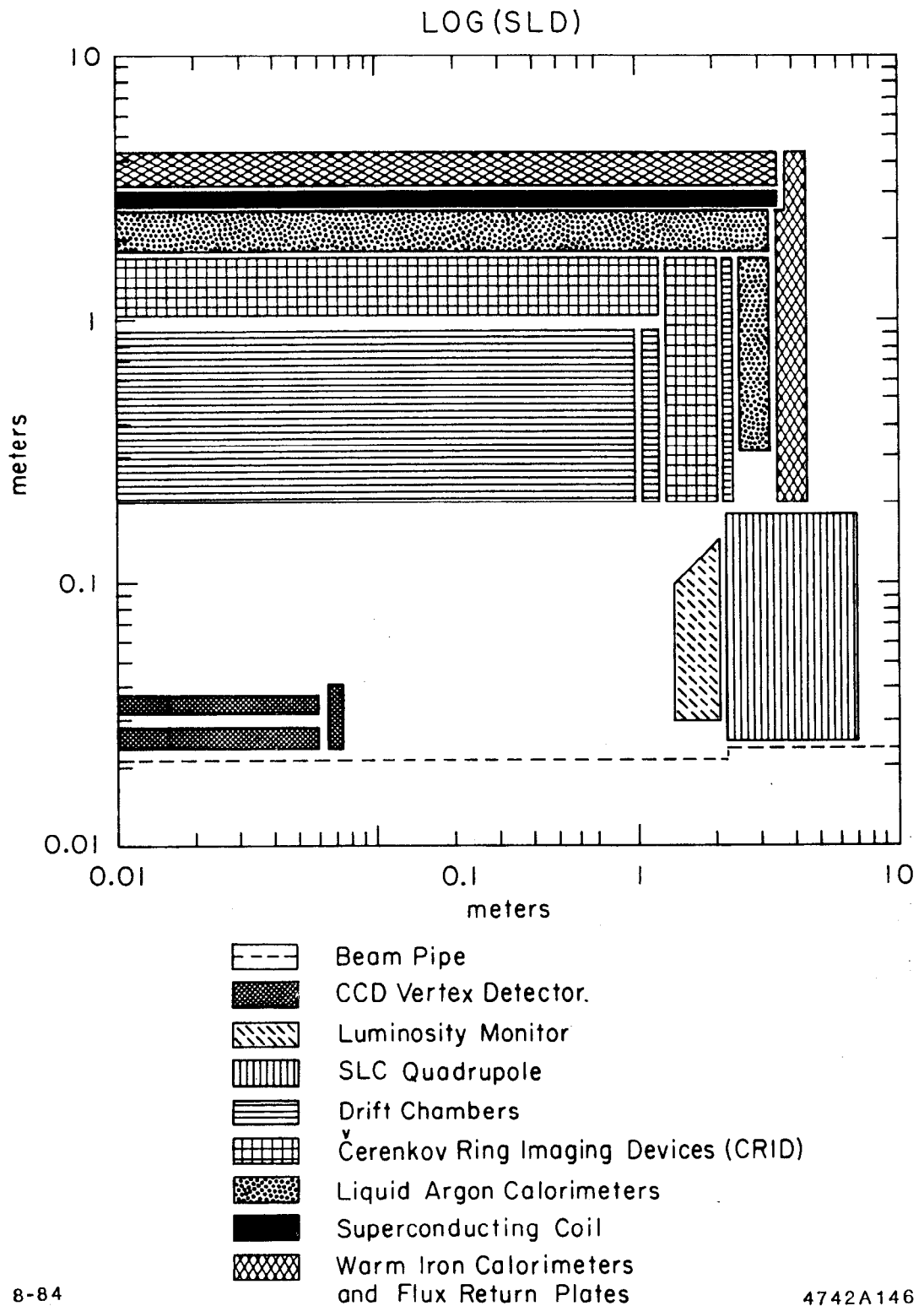
A collaboration of 20 institutions and 100 physicists recently completed the Design Report for such a detector, called the *SLD*. This report was accepted by the laboratory with the recommendation of the *EPAC* in May 1984.

May 1984

LOG (SLD)

Legend:
- Beam Pipe
- CCD Vertex Detector.
- Luminosity Monitor
- SLC Quadrupole
- Drift Chambers
- Čerenkov Ring Imaging Devices (CRID)
- Liquid Argon Calorimeters
- Superconducting Coil
- Warm Iron Calorimeters and Flux Return Plates

8-84

4742A146

Traditional detector schematics give short shrift to the precision components near the collision point. This logarithmic sketch strikes a different balance.

TABLE OF CONTENTS

1. INTRODUCTION

This Design Report describes the plans for the construction of the second detector for the *SLAC* Linear Collider to study e^+e^- collisions at energies of up to 100 GeV in the center-of-mass.

1.1 GENERAL MOTIVATION AND SCOPE

The study of e^+e^- collisions near 100 GeV in the center-of-mass promises to be very fruitful in testing the standard model in several ways:

- the detailed measurement of the mass, width, and decay modes of the recently discovered neutral weak intermediate boson, the Z^o;

- the search for, and possible study of, the *t*-quark, both in Z^o decays and in the toponium resonance;

- the study of the production and weak decay of heavy quarks;

- the search for the standard Higgs boson;

- counting the number of neutrino generations;

- the study of lepton and quark couplings, quark and gluon jets, and polarization effects.

High-energy e^+e^- collisions will also provide one of the cleanest and most powerful tools in looking for new physics beyond the standard model, such as the search for additional anomalous Z^os, nonstandard Higgs bosons, new technicolor or supersymmetric particles, new unexpected heavy leptons, anomalous quark or lepton couplings and anomalous polarization effects.

Two facilities to study e^+e^- collisions at high energies are presently under construction: the *SLAC* Linear Collider *(SLC)* at the Stanford Linear Accelerator Center and *LEP* at *CERN*. The projected completion date of the *SLC* is late 1986 or early 1987 and that of *LEP* is late 1988 or early 1989. *SLAC*, with the advice of its Experimental Program Advisory Committee (the *EPAC*), decided to exploit the early physics at the *SLC* by having a working and *PEP*-tested detector, the Mark II, ready and installed at the turnon of the *SLC*.

The continuing effectiveness of the SLC program when LEP turns on will depend on the relative luminosities of the two machines and on the power of the detectors. The peak luminosity at LEP is expected to be $(1\text{-}2) \times 10^{31}$ $(\text{cm}^2 \text{ sec})^{-1}$, with an average luminosity between 1/3 and 1/2 of the peak. The expected average luminosity of SLC is expected to be 6×10^{30} $(\text{cm}^2 \text{ sec})^{-1}$, which is similar to the average luminosity of LEP. LEP, however, will begin with four new detectors, each designed for these higher energies and the expected physics.

The SLC should be in a good position to compete with LEP, provided that there is a detector comparable to those being built for LEP and optimized for the physics in this energy region. Such a detector should have the following features:

1. good electromagnetic and hadronic calorimetry covering the complete solid angle with projective geometry, fine segmentation, and compensation of the hadronic energy loss for good energy resolution;

2. full instrumental capability over the complete solid angle, not only in the 'standard' central region;

3. powerful and robust particle identification over a wide range of momentum;

4. uniform technology throughout the full solid angle.

A clear difference between the e^+e^- detectors of the previous generation and the new detectors being planned for SLC and LEP is the presence of hadron calorimetry: all new detectors have taken pains to provide it and few of the previous generation detectors have it. The technique played a very important role in the discovery of the W boson at the $CERN$ $\bar{p}p$ collider.

Hadron calorimetry will provide a large qualitative improvement in the power of e^+e^- experiments at high energies. Total energy and missing momentum measurements are very effective ways of tagging heavy quark events. They are also a very powerful means of reducing backgrounds in a Higgs search. The searches for exotic particles such as Higgs mesons or supersymmetric particles are considerably enhanced by total calorimetric methods since a complete calorimeter 'detects' neutrinos and other noninteracting particles. In addition, calorimetric techniques can be used to reconstruct properties of whole jets, allowing access

to more abundant decay modes and providing information on the decay mode of the Higgs itself. The possibility of new particle searches using jet-jet effective mass spectroscopy is another reason for good hadronic calorimetry.

Some features of the *SLC* itself may be exploited in ways not possible at *LEP*. The ability to use a very small beam pipe allows the construction of ultra-precise vertex detectors using new technology. The small size means extrapolation errors are minimized and that solid state *CCD* technology, which would otherwise be prohibitively expensive, may be employed. The *SLC* will provide longitudinally polarized electrons, making possible detailed measurements of the structure of weak interactions. Some of these measurements are not possible without polarization; others that are possible without polarization have a sensitivity enhanced by as much as an order of magnitude by the use of polarization. The possibility of a major upgrade of an existing detector like the Mark II to be similar to the *LEP* detectors has received much attention. A completely new detector is preferable to such an upgrade for two reasons:

1. The scale of the Mark II is such that much of the detector would have to be rebuilt, making an upgrade comparable in cost with a new detector. It is then preferable to start without the constraints inherent in an upgrade.

2. The time scale implies that a very major upgrade of Mark II could not be completed by *SLC* turn-on time. The combination of a *PEP*-tested Mark II with minor modifications ready at *SLC* turn-on followed by a *LEP*-competitive new detector later is very powerful.

The *SLAC EPAC* recognized the need for a powerful, new detector and recommended that such a detector should be built, that it have hadron calorimetry, and that it should be "ready for data taking by 1988." This Design Report describes our plans for meeting these goals with a new detector, the *SLD*.

1.2 SUMMARY DESCRIPTION OF DETECTOR

The detector is shown schematically in Figures 2.1, 2.2, 2.3 and 2.4, and the performance parameters are summarized in Tables 2.1 and 2.2. Particle tracking and momentum measurement are provided by a vertex detector, a high-precision

central drift chamber, and pairs of endcap drift chambers, all in a 1 Tesla magnetic field produced by a superconducting solenoid. Particle identification is provided by *CRIDs* (Čerenkov Ring Imaging Detectors). Calorimetry is done in two parts; a liquid argon calorimeter *(LAC)* with uranium and iron radiators is located inside the coil, and the laminated iron of the flux return is instrumented with limited-streamer-mode tubes to complete the hadron calorimetry. The streamer tubes of this warm-iron calorimeter, called the *WIC*, are instrumented with strip readout to provide muon tracking in addition to calorimetry. The same technology is used on the end structures of the detector and the central region, thus providing uniform response in both regions.

1.2.1 Vertex Detection — CCDs

The vertex detector is a cylindrical mosaic of *CCDs* on a ceramic frame. The present design for the *CCD* vertex detector consists of cylinders at 1- and 2-centimeter radii with two disk-shaped endplates. The *CCDs* offer spatial resolution of $\sim$ 5 μm in unambiguous space points with very high efficiency. The *CCDs* are practical at the *SLC* because of the very small beam pipe and the machine properties which permit resetting of the devices during the 5.6 ms interpulse period along with suppression of the beam during readout. The resolution in the distance of closest approach varies between 4 and 20 μm, depending upon the momentum of the particle.

R&D by the subgroup working on *CCDs* is proceeding. The 22-micron-square pixels are found to be 98% efficient for minimum ionizing particles. In beam tests 17 tracks per square millimeter have been resolved.

1.2.2 Tracking — Central Drift Chamber

The central drift chamber has 80 layers of sense wires arranged in a vector cell geometry. Guard wire doublets are used between the sense wires to straighten the drift paths. Detailed computations simulating this cell structure with a slow gas (CO_2 + 8% isobutane is being investigated) indicate that a spatial resolution of about 100μm can be achieved. This translates into a momentum resolution of $\sigma(1/p) \le 1 \times 10^{-3}$ (GeV/c)$^{-1}$ over most of the useful solid angle. The tracking coverage extends to 97% of 4π by the use of endcap chambers. Charge division

and 50 mrad stereo provide z resolution of 1.3 mm at the vertex and 2×10^{-3} in the tangent of the dip angle.

A full-length prototype of the central drift chamber has been tested with a slow CO_2-isobutane gas. Although about 30% higher than the computer simulation, the resolution is still better than 100μm and threshold effects in the electronics may explain the discrepancy. The guard wire doublet scheme, which should improve performance, is also being tested.

1.2.3 Particle Detection — the CRIDs

The CRIDs have both a liquid freon radiator, whose light is proximity focused on the photon detector, and an isobutane radiator whose light is focused by mirrors on the opposite side of the photon detector. The photon detector itself is a quartz box containing TMAE to convert the photons. The photoelectrons then drift towards a set of proportional wires for readout. The Čerenkov circles will be looked for in locations determined using information from the central drift chamber, simplifying the pattern recognition problem. This system provides essentially complete particle identification for momenta from 0.2 to 30 GeV/c.

The CRIDs face three challenges: transporting the Čerenkov photons to the detector in the presence of aberrations and ultraviolet absorption, transporting the photoelectrons to the proportional chamber over a long drift region, and detecting the electrons in the proportional chamber without introducing photon feedback. A preamplification section with a gain of 25 is planned to screen out undesired positive ions and reduce photon feedback.

Current results from beam tests show clear Čerenkov circles with nearly 20 photoelectrons per incident track, indicating a quantum efficiency for the photon detection system of more than 90% of the ideal value.

1.2.4 Calorimetry

The LAC consists of about 3 interaction lengths and 20 radiation lengths with a readout in the form of projective towers of approximately 33 mrad on a side at $\theta = 90°$ in the electromagnetic section and 66 mrad in the hadronic section. The electromagnetic energy resolution is $\sigma(E) = 0.08 \times \sqrt{E\,(\text{GeV})}$. The

5-interaction-length *WIC* serves as a 'tail catcher' for the hadron showers which escape the *LAC*.

The presence of substantial calorimetry inside the coil relaxes the constraints on the thickness of the coil, as only about 15% of the energy of a 50 GeV jet is expected to escape the cryogenic calorimeter. The expected hadronic energy resolution is about $\sigma(E) = 0.45 \times \sqrt{E(\text{GeV})}$. The liquid argon calorimeter is segmented 4 times in depth, and the iron calorimeter provides 2 additional samples. The streamer tube readout of the warm iron calorimeter is in the form of cathode pads arranged in projective towers to follow those in the liquid argon. The streamer tubes are also equipped with strip readout for muon tracking, so that the iron also serves as a muon detector.

A prototype calorimeter using the liquid-argon uranium stack followed by a warm iron system has been installed in the test beam and will test the expected electromagnetic energy resolution, energy compensation in a hybrid calorimeter, and the efficiency of the tail catcher.

1.2.5 *Superconducting Coil*

There are now three practical options for the superconducting coil: the indirectly cooled system used now in several existing and planned detectors, a new internally cooled system proposed by the *MIT* Magnet Laboratory, and the traditional 'bath-cooling' technique.

The internally cooled method is a new technique in which liquid helium flows through the void spaces of an encapsulated superconductor (a 'rope in a pipe'). Five kilometers of this kind of conductor have been manufactured by industry using niobium-tin. Niobium-titanium is being considered for the *SLD* and the problems associated with the change in material are being studied.

A design comparison of the indirectly cooled high purity aluminum stabilized conductor and bath cooled copper stabilized conductor is underway.

The coil is the pacing item for the project. The conductor should be ordered in *FY85* and magnetic measurements should be completed in *FY87*. The collaboration expects to procure the coil commercially.

1.2.6 Data Acquisition

The very large number of readout channels needed to cope with the complicated Z^o event topologies requires a new generation of readout electronics. The detector will have about 200k channels of instrumentation feeding 81 crates of Fastbus electronics. The 180 Hz repetition rate of the collider allows 5 milliseconds for trigger processing without incurring deadtime.

New *VLSI* electronics for waveform sampling for calorimetry data storage are being developed in collaboration with the Stanford Electronics Laboratory. The sampling memory will have 256 sample-and-hold units which will sample at 200 MHz with an 11-bit dynamic range.

1.3 BUDGET AND SCHEDULE SUMMARY

A detailed analysis of the costs and time schedules has been carried out. The total cost of the detector without contingency is estimated to be $39.8M in *FY84* dollars. A breakdown of the costs by major components is as follows:

		$ M
1.1	Magnet and support structure	11.5
1.2	Vertex detector	0.9
1.3	Tracking system	2.3
1.4	Particle identification system	5.9
1.5	Liquid argon calorimeter	13.4
1.6	Warm iron calorimeter	2.1
1.7	General purpose electronics	1.4
1.8	Beamline equipment	0.7
1.9	Related costs	1.7
		$39.8 M

The funding is distributed among four sources: $34.5M from the Department of Energy *(DOE)*, $0.6M from *INFN* in Italy, $2M from Canada, and $2.7M from the National Science Foundation *(NSF)*. Contingency is 25% , bringing the total cost to just under $50M in *FY84* dollars.

The anticipated time schedule for the design, construction, testing, and installation of the detector is shown in Figure 2.5, broken down by major com-

ponents. The superconducting coil is the pacing item; it is hoped to present a Request for Proposal for the conductor in 3 to 4 months with ordering in 1985. Tests would start in the beginning of 1987.

As can be seen from this schedule, the goal is to have the detector ready for data taking in calendar year 1988, as recommended by the *EPAC*. This time schedule is obviously critically dependent on the funding profile available. This goal has been accepted by the US Department of Energy, the principal source of funding.

A more detailed discussion of the budget and schedule is given in Chapter 13.

2. DETECTOR SPECIFICATION

The proposed performance parameters of the detector are summarized in Table 2.1. Some characteristics of the major detector components, such as spatial dimensions and number of readout channels, are summarized in Table 2.2. All of these quantities are described in much more detail in the following sections of this Design Report.

The general features of the detector are shown in Figures 2.1, 2.2, 2.3 and 2.4.

Table 2.1.
Summary of Proposed Performance Parameters

Drift Chamber System	
Spatial Resolution	$\sim 100\ \mu$m
Magnetic Field	1.0 Tesla
Momentum Resolution	
$\sigma(1/p)$ measurement limit	$1 \times 10^{-3}\ (\text{GeV}/c)^{-1}$
$\sigma(p)/p$ Coulomb scattering limit	$(1-2) \times 10^{-2}$
Two-Track Separation	2 mm
Calorimetry	
Electromagnetic	
Energy Resolution $\Delta E/E$	$8\%/\sqrt{E\,(\text{GeV})}$
Segmentation	~ 33 mrad $\times$ 33 mrad
Angular Resolution	~ 5 mrad
Hadronic	
Energy Resolution $\Delta E/E$	$45\%/\sqrt{E\,(\text{GeV})}$
Segmentation	~ 66 mrad $\times$ 66 mrad
Angular Resolution	~ 10 mrad
Vertex Detector	
Segmentation	$22\ \mu$m $\times 22\ \mu$m
Precision Transverse to Line of Flight	$4 - 20\ \mu$m
Two-Track separation	$40\ \mu$m
Particle Identification	
e/π	1×10^{-3}
μ/π (above 1 GeV)	2×10^{-3}
K/π (up to 30 GeV)	1×10^{-3}
K/p (up to 50 GeV)	1×10^{-3}
Solid Angle Coverage	
Tracking	97%
Particle Identification	97%
EM Calorimeter	$\geq 99\%$
Hadron Calorimeter	97%

Table 2.2.
Some Characteristics of the Main Detector Components

Component	Size in Centimeters				Readout
	R_{min}	R_{max}	Z_{min}	Z_{max}	Channels
Vertex Detector	1	10	—	10	220
Luminosity Monitor	3	18	180	200	2048
Drift Chamber – Barrel	20	100	—	100	10,240
Inner Endcap	20	98	102	122	1,280
Outer Endcap	20	173	195	215	2,048
CRIDs – Barrel	102	175	—	193	23,700
Endcap	20	132	122	195	9,300
Liquid Argon Cal – Barrel	177	278	—	314	34,400
Endcap	20	173	215	316	9,600
Superconducting Coil	280	328	—	342	- - -
Warm Iron Cal – Barrel	330	450	—	344	9,800 [a]
Endcap (door)	20	450	316	436	110,800 [b]

R – Radius around $e^{\pm}$ beams.
Z – Distance along $e^{\pm}$ beams.
[a] Towers.
[b] Strips (digital shift register readout only).
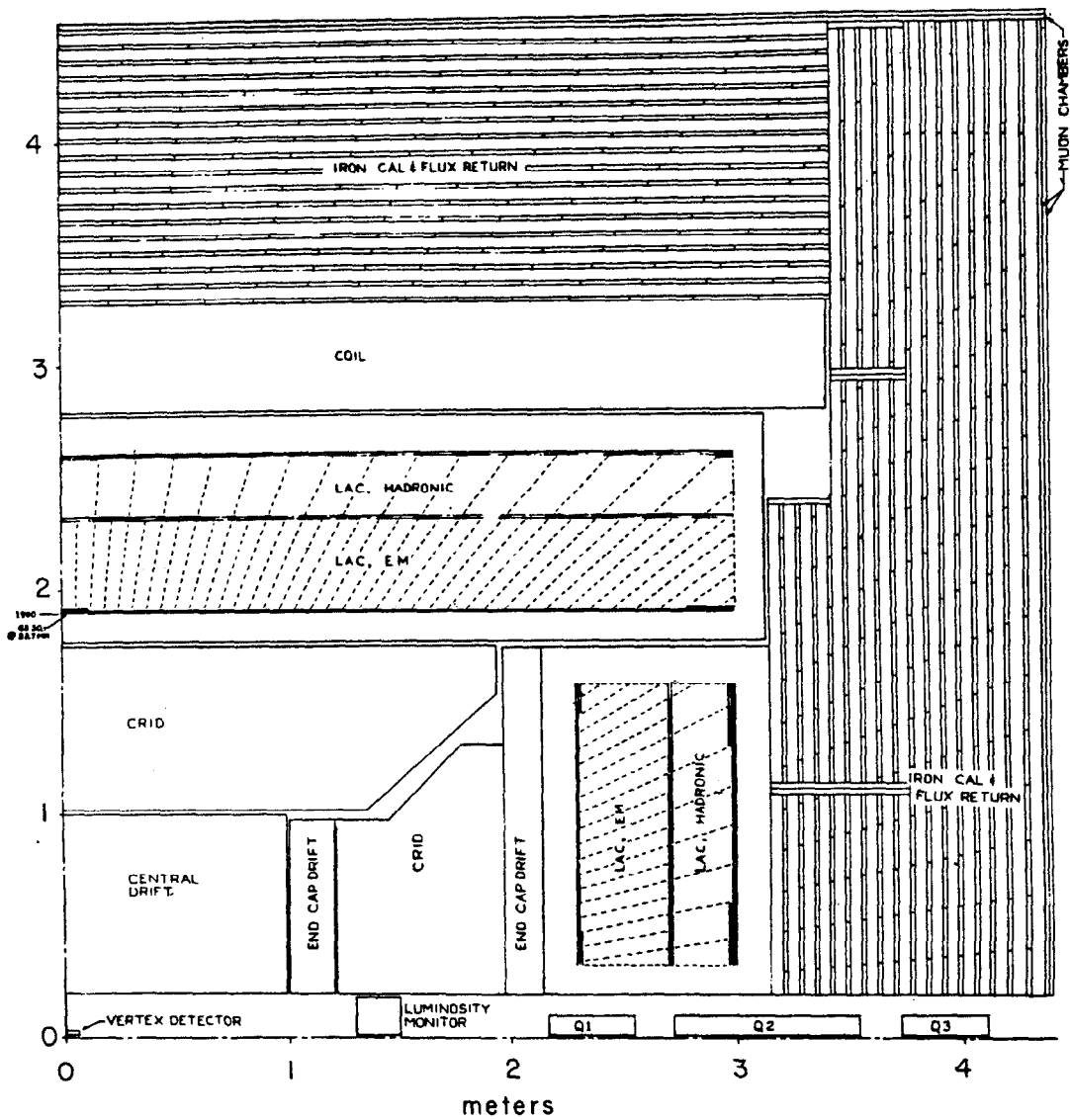
Figure 2.1. Vertical section in the plane including the $e^\pm$ beams of one quadrant of the detector.
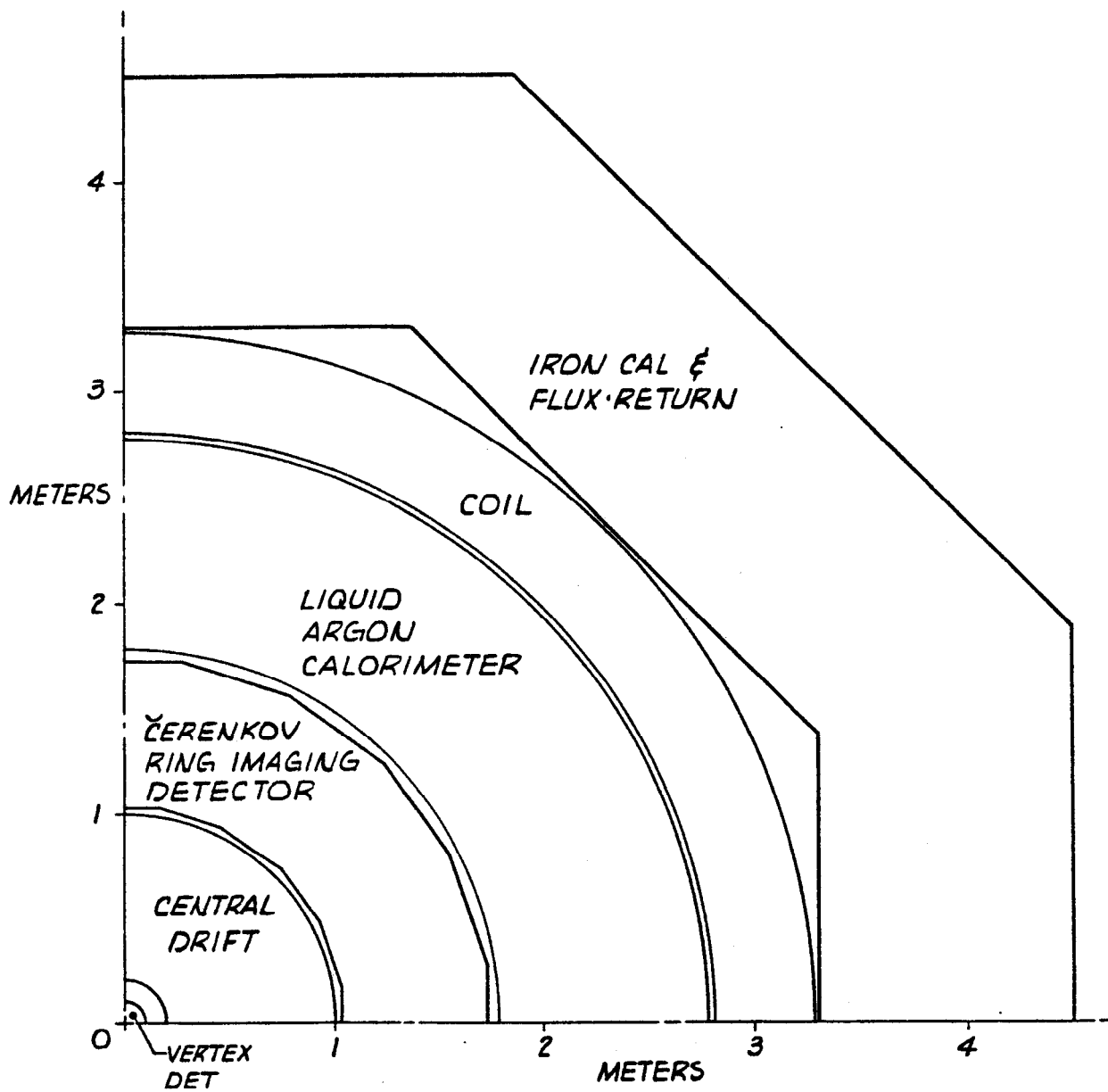
Figure 2.2. Vertical section in the plane perpendicular to the $e^{\pm}$ beams of one quadrant of the detector.
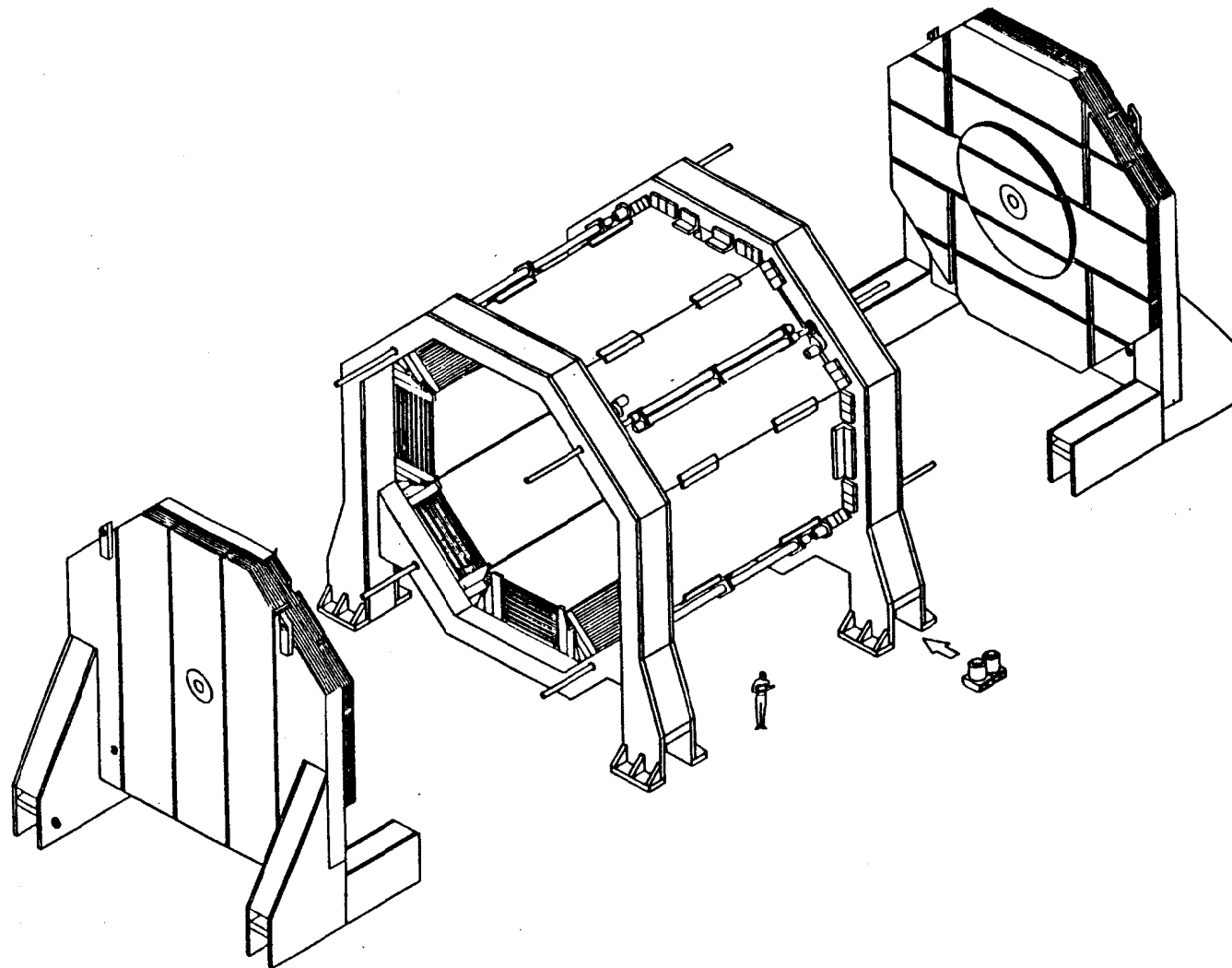
Figure 2.3. Isometric view of the detector.
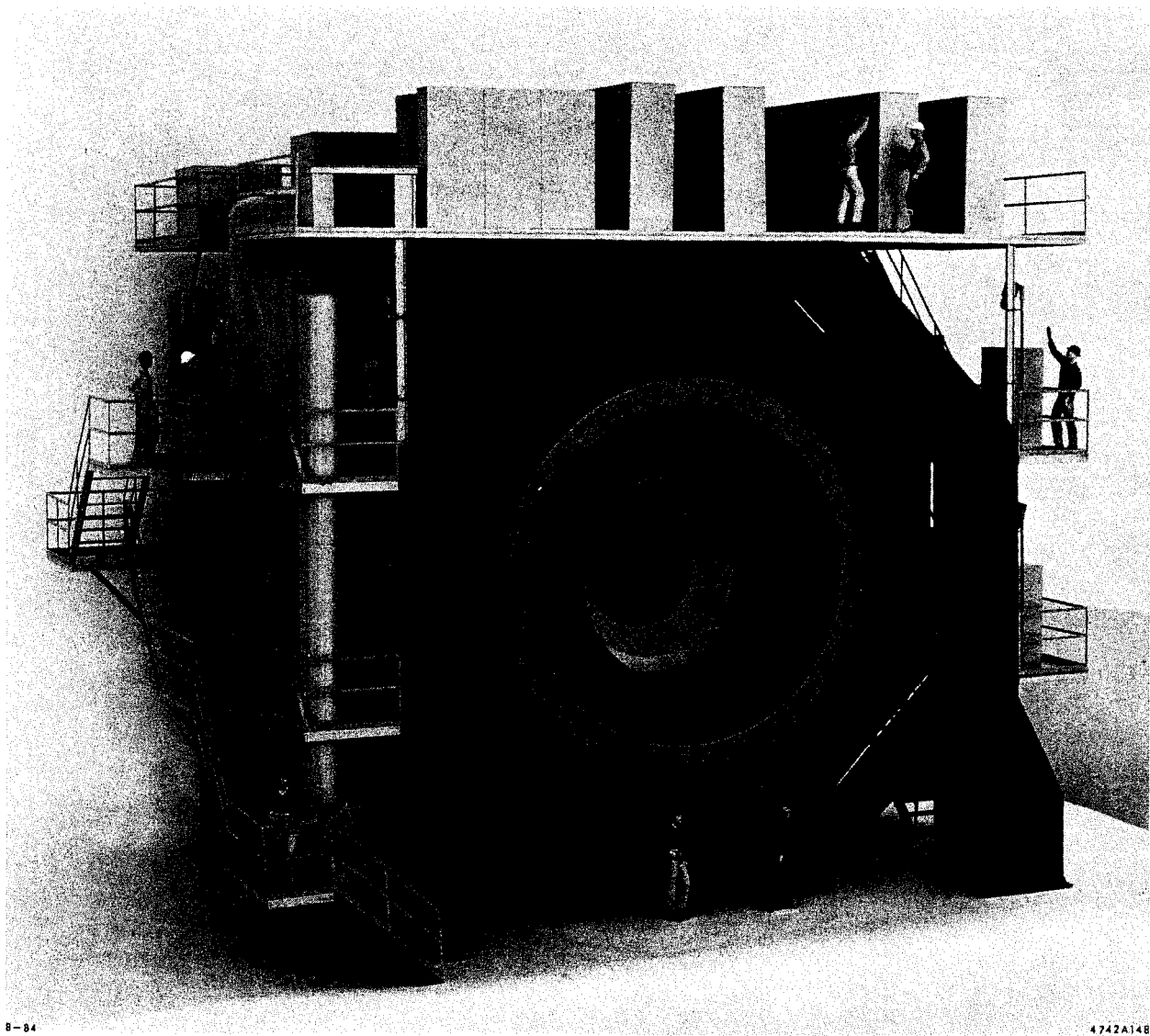
Figure 2.4.   Overview of the assembled detector.

3. PHYSICS MOTIVATION

The physics of e^+e^- collisions near 100 GeV has been widely discussed both in the literature and at numerous summer studies. Thus an exhaustive and general discussion of these topics will not be included in this Design Report. Instead, the physics is considered from several specific points of view that are relevant to the design of the *SLD*.

Section 3.1 lists some of the topics which are likely to be important and indicate how they influence the choice of detector components.

Section 3.2 treats the capabilities of the detector compared to the other detectors that will be doing e^+e^- physics in this energy range, such as the Mark II at the *SLC* and the four new detectors at *LEP*.

3.1 LIST OF PHYSICS TOPICS AT THE *SLC*

3.1.1 Testing the Standard Model

Z^o Mass and Width

These measurements do not place very stringent requirements on the detector, but require good energy resolution and calibration of the $e^{\pm}$ beam in the accelerator.

Z^o Decay Branching Ratios

Since the Z^o decay modes will be very rich, their detailed study will require good charged particle tracking, electromagnetic calorimetry and muon identification for the leptonic modes, and particle identification and a vertex detector to identify strange, charmed, and bottom particles in the hadronic decay modes.

Weak Neutral Current Couplings of Leptons and Quarks

These will in large part come from the Z^o decay rates into particular two-body modes and from charge asymmetries and polarization measurements.

Weak Charged Current Couplings of Heavy Quarks – the *KM* Mixing Angles

This information comes mainly from branching ratio measurements such as $(t \rightarrow b)/(t \rightarrow s)/(t \rightarrow d)$ in hadron decays. Thus the vertex detector and good

particle identification are very important in efficiently identifying heavy quarks with low backgrounds.

Search for t-Quarks in Z^o Decays

This search would depend on semileptonic decays like $t \rightarrow be\nu_e$ or $t \rightarrow b\mu\nu_\mu$, where the signature is a large p_T lepton and missing energy carried off by the neutrino. Large jet effective masses and peculiar event topologies may also be useful in identifying t-quark jets. Thus electromagnetic calorimetry, muon identification, and 4π solid angle hadron calorimetry to detect the missing energy carried off by the neutrinos are important.

Spectroscopy of Mesons and Baryons with t or b Quarks

These studies will rely on the reconstruction of effective masses of hadrons with identified strange and charmed particle content. The vertex detector and good particle identification will be important as well as precision measurement of charged particle momenta in the tracking chambers.

Study of QCD and Gluon Jets

Finely segmented hadron calorimetry will play an important role in these studies. It will also be desirable to identify the flavor of the quark initiating the jets. This can be done by charm tagging in the vertex detector, identifying strange particles in the $CRIDs$, or tagging high-p_T electrons or muons in the electromagnetic calorimeter or the muon system.

Toponium Spectroscopy

This could be quite an important topic at the SLC if the toponium mass is below the Z^o mass, especially if it is also above the masses accessible to $TRISTAN$. Decays into $e^\pm$ and $\mu^\pm$ pairs, as well as measurement of single photons, will be important in these studies, requiring good electromagnetic calorimetry and muon identification. High precision charged particle tracking will also be crucial.

Counting of Neutrino Generations via the Reaction $e^+ + e^- \rightarrow Z^o + \gamma$, $Z^o \rightarrow \nu + \bar{\nu}$

Good electromagnetic calorimetry to measure the photon is obviously important. In order to keep the formidable backgrounds under control, it will

be important to have essentially 4π solid angle calorimetry with a minimum of cracks or dead spaces to reject background events with additional particles.

Search for the Standard Higgs Boson (the H^o)

The most promising reaction for this search is $e^+e^- \to Z^o \to H^o + e^+ + e^-$ or $H^o + \mu^+ + \mu^-$, where the H^o mass is calculated from the measured e^+e^- or $\mu^+\mu^-$ mass. Thus high resolution electromagnetic calorimetry and muon identification with precision charged particle momentum measurement are important. Hermetic hadron calorimetry might also allow the more abundant reactions $e^+e^- \to Z^o \to H^o + \nu + \bar{\nu}$, where the signature is the missing energy of the neutrinos and the H^o mass would be reconstructed from its decay into hadron jets (jet-jet mass spectroscopy).

Asymmetries and Polarization Studies

Measurement of angular distributions of e^+e^- or $\mu^+\mu^-$ pairs will be important, requiring electromagnetic calorimetry and muon detection especially near small angles. Angular distributions of hadron jets in two-jet events may also be interesting, requiring finely segmented hadron calorimetry, again especially at small angles.

3.1.2 New Phenomena

Search for Additional Anomalous Zs

An additional Z would manifest itself in a peak in the total cross section above the Z^o mass. However, in view of the energy limit of the *SLC*, a more sensitive search might be to look for anomalies in decay angular distributions of the Z^o.

Search for Nonstandard Higgs Bosons

Nonstandard Higgs bosons, such as the charged Higgs, are predicted by some models. These would presumably be pair-produced at the Z^o, $e^+e^- \to Z^o \to H^+ + H^-$. Each Higgs can decay into a $q\bar{q}$ pair, in which case the event will have four hadron jets, and a finely segmented large solid angle hadron calorimeter is crucial in detecting the jets and reconstructing the jet-jet effective masses. Another possibility would be one Higgs decaying into $q\bar{q}$ while the other goes

into $\tau + \nu_\tau$. In this case a large-solid-angle hadron calorimeter is crucial to detect the signature of the missing energy carried off by the neutrinos, combined with electromagnetic calorimetry or muon detection to see the charged e or μ from the τ decay.

Search for Technicolor or Supersymmetric Particles

The technicolor particles are expected to decay preferentially into the heaviest allowed decay products. Thus decays into heavy quark pairs, such as $b\bar{b}$ or $t\bar{t}$, are expected to dominate over decays into lepton pairs. In this case, finely segmented hadron calorimetry will be very important in reconstructing these jet-jet effective masses. In the case of supersymmetry (SUSY) there is expected to be a conserved quantum number so that supersymmetric quarks or leptons will have a neutral photino, gluino, or Goldstino among their decay products which presumably do not interact in the detector. Thus a large-solid-angle hadron calorimeter is crucial in these searches to provide the signature of large missing energy carried off by these neutrals.

Search for New Heavy Leptons

A powerful signature for new heavy leptons pair-produced in $e^+ e^-$ collisions would be provided if one heavy lepton decayed into an $e^\pm$ while the other decayed into a $\mu^\mp$, as was the case in the discovery of the τ lepton. At these high energies care must be taken to avoid confusing such events with other heavy-particle decays by semileptonic modes. Good electromagnetic calorimetry combined with muon detection is necessary for this search.

Search for New Heavy Quarks

Searches for new heavy quarks can be made by looking for narrow resonances ("onia") in the $e^+ e^-$ total cross section (as well as in Z^0 decays). Such searches do not require a very sophisticated detector, but rest mostly on good energy resolution in the $e^\pm$ beams from the accelerator.

3.2 *SLD* CAPABILITIES COMPARED TO OTHER DETECTORS AT THE *SLC* AND *LEP*

3.2.1 *Comparison with Mark II*

The Mark II detector was originally designed to study lower energy e^+e^- collisions at *SPEAR* and *PEP*, where it has demonstrated excellent performance on a wide range of physics topics. With some upgrades, which will also be tested at *PEP*, it will be the first detector to study Z^o physics in e^+e^- collisions. The main advantage of this arrangement will be to have a fully tested detector ready to study new physics rapidly after *SLC* turn-on.

The second detector, the *SLD*, has been optimized in its design for the higher energy region and more challenging performance requirements of 100 GeV e^+e^- physics, as discussed in the previous section. The main improvements over Mark II consist of a fine-grained, energy-compensated 4π solid angle electromagnetic and hadronic calorimeter with projective geometry, essentially full 4π coverage in tracking and muon detection, and a very effective, full-solid-angle particle identification system.

Some of the physics topics listed in the previous section can be done well with Mark II; others can be done considerably better with the increased capabilities of the *SLD*; and others are feasible only with the full power of the *SLD*. A few examples of each of these follow.

Physics Topics that can be Done with Mark II

The early experiments at the *SLC* are likely to consist of energy scans by the machine. Mark II can easily measure the mass and the width of the Z^o by simply counting events as the energy is increased over the Z^o peak and normalizing to the accumulated luminosity at each energy point. Accuracies in mass and width will most likely be limited not by statistics but by systematic effects arising from finite energy spread, beam energy calibration, and radiative processes which effectively increase the energy spread of the incoming beam. Accuracies in $M(Z^o)$ to ± 0.1 GeV and in $\Gamma(Z^o)$ to ± 0.1 GeV seem feasible. The first measurement can provide a unique value for $\sin^2\theta_W$ (to approximately ± 0.0006, which is more than an

order of magnitude improvement over today's values). The width measurement provides an independent test of the standard model and measurement of the number of light neutrino species and should be sensitive to a few extra neutrino types, much better than any present limits. Mark II can perform certain other tasks well. A search for the t-quark in the decay products of the Z^o would be interesting, if the t-quark has not been found by other means. This search would consist of looking for high mass jets in two-jet decays of the Z^o, or for jets of high sphericity, augmented possibly by a high-p_T lepton tag coming from the leptonic decay modes of the decay chain quarks. A search for a light mass Higgs particle is still another example of an interesting and undemanding topic which Mark II may do well. The SLC Workshop studies showed that the neutral Higgs boson, the H^o, can be seen in $e^+e^- \rightarrow e^+e^-H^o$, for H^o masses below 20 GeV. This process has the unique signature of an e^+e^- pair accompanied by, but separated from, two jets from the H^o decay. The missing mass recoiling against the e^+e^- pair is the H^o mass.

Physics Topics for which *SLD* has an Advantage

There is a broad class of topics for which the full power of the *SLD* will be of great value, but which can be studied in a more limited way by Mark II. The advantage of full solid angle coverage, hadron calorimetry, and particle *ID* combined with very good vertex detection give *SLD* a much cleaner sample of data in most cases. The neutrino counting experiment is one example. The process $e^+e^- \rightarrow \gamma\nu\bar{\nu}$, where the energy of the beams is set above that needed for the Z^o peak, is detected by a single radiated photon. The rate of the process is proportional to the number of light neutrino types that couple to the Z^o. Backgrounds may be serious, however, and complete solid angle coverage is important to ensure a veto of unwanted processes such as $e^+e^- \rightarrow e^+e^-\gamma$ and $e^+e^- \rightarrow \gamma\gamma$. Both of these *QED* processes have large rates compared to the process of interest. Mark II's central electromagnetic calorimeter has approximately 10% missing coverage in the barrel region caused by the walls of the liquid argon cryostats. These cracks may allow unwanted processes such as the *QED* events to fake the signal of a single photon and thereby contaminate the signal. *SLD*

will have an electromagnetic calorimeter which is continuous in the barrel region and endcap regions, with only small regions for the beam pipe uncovered.

Jet studies can be carried out by Mark II, including measurement of α_s, jet topologies, energy flow, fragmentation, and correlations. Separation of jets into light and heavy quarks may be problematic for Mark II. The advantage *SLD* has for these studies lies in the heavy quark identification techniques through hadronic calorimetry, which can identify missing energy from escaping neutrinos, combined with vertex detection and particle identification information. Heavy quarks should be cleanly identified in *SLD* with reasonably high efficiency. Using the heavy quark flavor tagging, *SLD* can measure the standard quark couplings of the Z^o, and with them test the 'universality' relations of the standard model. Heavy quark flavor tagging also significantly enhances the studies of the *K-M* matrix elements.

Polarization studies at the *SLC* provide an area of physics that will not be investigated at *LEP*. Polarized beams are very useful in some specific measurements. Tests of the exactness of $SU(2) \times U(1)$ can be made with polarized beams by measuring rather precisely the parameter $\sin^2 \theta_W$ independently of that obtained from the $M(Z^o)$ measurement mentioned above. The accuracy that can be achieved requires that higher order electroweak corrections be made correctly, that is, the value of $\sin^2 \theta_W$ from polarization measurements must agree with the value from $M(Z^o)$ measurements. One of the preferred channels for these measurements is $Z^o \rightarrow \mu^+ \mu^-$. Small-angle coverage is important for these measurements, as about half of the information comes from angles below $40°$. Mark II lacks muon identification in the forward and backward angles; the *SLD* has complete identification in 97% of the solid angle. This increased coverage substantially improves the statistical and systematic accuracy for muon pair charge asymmetries.

Physics Topics that Require the Unique Capabilities of the *SLD*

Several Z^o physics topics require detector capabilities that are missing in Mark II, but exist in *SLD*. The hadron calorimeter with its good energy and spatial resolution serves as an identifier of missing energy. Missing energy signi-

fies neutrinos or neutrino-like objects escaping from the event undetected. Supersymmetry searches can be based on missing energy and unbalanced visible momentum. Typical processes include $Z^o \rightarrow \bar{\nu}\bar{\nu}$ which then decay into charged particles and unseen $SUSY$ particles such as the $\tilde{\gamma}$. The rate of these processes may be low, and searches for the rare decays depend on eliminating backgrounds caused by poor resolution and cracks in solid angle coverage.

Spectroscopy of particles produced in Z^o decays include studies of D^os, B^os, baryons, and other particles. These studies are greatly enhanced by particle identification and vertex reconstruction, as workshop studies have shown. $B^o - \bar{B}^o$ and $D^o - \bar{D}^o$ mixing studies require the full power of particle identification to eliminate combinatorial backgrounds. The full capabilities of the SLD give it considerable advantage in a number of topics listed above. Beyond lies the unknown territory open for new discoveries. The better calorimetric resolution, solid angle coverage, particle identification, and vertex reconstruction increase the probability for new discoveries and the confidence in any new discovery which may come its way.

3.2.2 Comparison with LEP Detectors

The most obvious competition for the physics which can be done with SLD will come from LEP and the four detectors under construction: $ALEPH$, $DELPHI$, $L3$ and $OPAL$. Since these experiments were approved in June 1982 and submitted detailed Technical Reports in April 1983, it would be surprising if they were not ready for LEP turnon, scheduled for early 1989. On this timescale, the SLC may have approximately a year and a half of running before LEP, and even though it is an ambitious machine, a modest luminosity should make a lot of conventional Z^o physics accessible before any physics at all is possible at LEP. The amount to which SLD can share this noncompetitive running with Mark II will depend on the state of readiness of the SLD detector.

LEP in its first phase is a conventional and rather conservative machine, and should come online quickly, most probably achieving something approaching the design luminosity within the first couple of years. This is then the real LEP competition which SLD must address, namely running in parallel with the early

years of *LEP* and its detectors.

As an accelerator, *SLC* will have two advantages over *LEP*. In order to achieve good luminosity the beam size at crossing must be small, $\lesssim 2~\mu$m in radius, and should permit a close distance of approach of ~ 1 cm for a vertex detector. There is also the realistic possibility of collisions with polarized beams, which are much more easily implemented at the *SLC* than at *LEP*.

If the conventional $SU(2) \times U(1)$ standard model is sufficient to describe the weak and electromagnetic interactions in detail, then the case for polarization is not overwhelming. If this were not the situation and if there appear to be unexpected features of Z^o decays emerging from the *CERN* $\bar{p}p$ collider, then polarization could be a very valuable tool for revealing unorthodox phenomena.

SLD plans to take the fullest advantage of the small beam spot as early as possible by including a high-resolution vertex detector (resolution $\sim 5~\mu$m) based on *CCD* devices within about 2 cm of the collision point. With this detector it should prove possible to tag events with taus, *c*-quarks and *b*-quarks (and *t*-quarks?) and to measure lifetimes down to $\sim 4 \times 10^{-14}$ sec. The ability to observe a decay vertex could be vital in searches for Higgs where decay modes like $H^o \rightarrow \tau\bar{\tau}$, $c\bar{c}$, $b\bar{b}$ should predominate. The power of the vertex detector is greatly enhanced when allied with hadron identification from the *CRID*s; kaon identification plus the secondary vertex requirement can yield a completely clean sample of reconstructed *D* and *B* mesons.

At *LEP* the closest distance of approach to the collision point will be about 8-10 cm and the lever arm for resolving a decay vertex is much larger. The volume of the required high resolution detector, in all probability involving frontier solid state technology, becomes prohibitively large. *DELPHI* is the only *LEP* detector planning to implement Čerenkov ring imaging for particle identification. *ALEPH* will have some particle identification from dE/dx in the *TPC*. These, when combined with proposed vertex detectors (silicon μ strips with one-dimensional resolution $\sim 5~\mu$m) should be able to isolate *D*-mesons, but not with the efficiency or the cleanliness of *SLD*. The small size of the *SLC* beam plus the *SLD* vertex detector and *CRID*s will allow identification of *D*s with virtually

no background, providing a unique physics advantage in looking for Bs and Ts over the *LEP* program.

The central tracking chambers of *SLD* and the *LEP* detectors, with the possible exception of $L3$, have similar capabilities for momentum measurement ($\Delta p/p^2 \sim 10^{-3}$ GeV/c^{-1}) but techniques vary. *ALEPH* and *DELPHI* both plan large *TPCs* with $\sigma(r\phi) \sim 250~\mu$m. They have profited greatly from the *TPC* experiment at *PEP*, and their prototype work is impressive, so both detectors should realize the full visual potential of the *TPC* method at turnon. *OPAL*, like *SLD*, plans a state-of-the-art drift chamber with $\sigma(r\phi) \lesssim 150~\mu$m. The momentum measurement in $L3$ is somewhat worse and depends on the realization of a spatial resolution of $\lesssim 30~\mu$m in a small volume chamber. $L3$, however, contains at large angles a dedicated muon spectrometer which should give a mass resolution at 90 GeV of $\Delta M/M \lesssim 1.7\%$.

All detectors plan to cover $\gtrsim 98\%$ of the solid angle with calorimetry readout in projective tower geometry, but significant differences exist in the methods used by the various experiments.

ALEPH plans an electromagnetic calorimeter based on 2 mm of lead sampling and readout by wire chambers in the high gain proportional mode. The calorimeter is inside the superconducting coil and the emphasis is on good position resolution ($\lesssim 17$ mrad) through the use of 'mini-towers,' with modest energy resolution $\sigma/E \sim 16\%/\sqrt{E}$. Outside the coil the iron return yoke has laminations of 5 cm, which form the hadron calorimeter yielding $\sigma/E \sim 80\%/\sqrt{E}$. *DELPHI* plans an electromagnetic calorimeter using the *HDP* (High Density Projection Chamber) technique. Ionization from the shower is drifted to a readout consisting of a single plane proportional chamber. The sampling material is lead (~ 2.8 mm), the drift is over ~ 60 cm, and the projected resolution is $\sigma/E \sim 15\%/\sqrt{E}$. The position resolution is potentially good because of the drift velocity of about 5 mm/μs. Outside the coil of the solenoid the ~ 5 cm laminations of the return yoke serve as a hadron calorimeter with $\sigma/E \sim 75\%/\sqrt{E}$. $L3$ is the only *LEP* detector with a dedicated ability to detect low-energy single photons by using an unobscured array of 12,000 *BGO* crystals. The intrinsic energy resolution is

claimed to be excellent: $\sigma/E = (0.5\%/\sqrt{E} + 0.3\%)$; for photon energies ≥ 1 GeV the spatial resolution is $\lesssim 3$ mm. Immediately behind the *BGO* is a hadron calorimeter using copper and uranium sampling to give $\sigma/E \sim 60\%/\sqrt{E}$. *OPAL* bases its electromagnetic calorimetry on an array of lead glass blocks behind the $1.5X_0$ thick magnet coil. A presampler is used between the coil and the array in order to detector electromagnetic showers initiated before the lead glass. The projected resolution for energies > 5 GeV is $\sigma/E \sim 4\%/\sqrt{E} + 1.5\%$. At energies below 5 GeV the resolution gets progressively worse, degraded by the coil. The magnet return yoke is sampled in 10-cm steps to provide hadron calorimetry with $\sigma/E \sim 130\%/\sqrt{E}$. These calorimeters will all be plagued by the same difficult systematic problem of measuring energy in a device which responds differently to hadronic and electromagnetic radiation. The so-called 'electromagnetic calorimeters' are approximately one interaction length thick at $90°$, and for typical events at the Z^0, on average, $\sim 80\%$ of the energy in the event will be deposited in this first interaction length of lead, *BGO* or lead glass, where the electromagnetic response at low energies is likely to be $\sim 40\%$ greater than the hadronic. This will introduce appreciable systematic uncertainties in determining missing energy and jet energies, thus compromising the ability to detect neutrinos and to use multi-jet masses in any search for rare particles dependent on the fluctuations in jet fragmentation.

SLD plans an integrated approach to calorimetry using the unique fission-derived property of depleted uranium to compensate for hadron energy expended in nuclear breakup. The combined uranium calorimeter will be situated inside the superconducting coil. It is approximately 3-interaction-lengths thick and has a liquid argon readout. The front section ($\sim 20X_0$) with fine sampling (1.6 mm) should give $\sigma/E \sim 8\%/\sqrt{E}$ for electrons and photons. The energy leaking beyond the coil will be measured in a second calorimeter based on 5-cm laminations in the iron return yoke. The overall hadron energy resolution should be $\sim 45\%/\sqrt{E}$.

This compensated calorimetry will give *SLD* an advantage in the analysis of events with missing energy, such as events with neutrinos and possible signa-

tures for supersymmetric particles. It will be especially powerful when neutrino detection can confirm the semileptonic decay of heavy quarks where there are major background problems, as in searches for Higgs. Jet energies will be measured independently of fragmentation, making mult-jet mass searches for exotic new particles a realistic possibility. Only *L3* of the *LEP* detectors has the real opportunity of an upgrade to a uranium calorimeter, but at the expense of *BGO*. Space restrictions make it very difficult for *ALEPH*, *DELPHI*, and *OPAL* to do this at this stage.

In summary, *SLD* compared to *LEP* detectors will retain two major unique advantages. One derives from exploiting fully the small beam size at *SLC* through a close microvertex detector whose information can be combined very effectively with the particle identification from the *CRIDs* to detect short-lived secondaries. The second derives from the compensated uranium calorimetry, which will enable the best possible exploitation of the well-defined initial energy of the e^+e^- collisions for detecting noninteracting particles in the final state through their missing energy.

4. MAGNET AND SUPPORT STRUCTURE

4.1 INTRODUCTION

The *SLD* magnet and support structure consists of four basic elements: the superconducting coil; the exoskeleton support frame; the barrel iron; and the endcaps or doors.

The superconducting coil is 5.8 meters in diameter and 6.2 meters long, and provides a solenoidal field of 1 Tesla in a magnetic volume of 162 m^3. The radial component of this field must be kept small to avoid interfering with the electron drift characteristics of the Čerenkov Ring Imaging Detectors that will be placed in the magnet. At a radius of 1.2 meters, the line integral of the radial component along a 1.5 meter path parallel to the beam direction must be less than 200 gauss-meters.

The iron in the barrel and endcaps provides the return flux path for the magnetic field. This iron structure consists of seventeen layers of 5-cm-thick plates with 2-cm gaps. Detector elements in these gaps convert this passive flux return into a calorimeter with an iron radiator. Figure 4.1 shows an isometric view of the assembly.

4.2 FIELD CALCULATIONS

4.2.1 Static Fields

The *SLD* magnetic field has been modeled in cylindrical geometry using the computer program Poisson, modified to handle up to 15,000 mesh points and 50 separate regions. The 'iron table' used in these calculations is a combination of measured permeability values and the saturation properties of typical steels used in *SLAC* magnets.

The computer model is shown in Figure 4.2. The Poisson generated mesh for this model is shown in Figure 4.3. The fact that the outer iron configuration is octagonal rather than cylindrically symmetric is not thought to be a serious problem. The end doors, however, present a different problem. The manufacturing process introduces a magnetic coupling between the laminations in certain parallel planes. Since there are only a few such planes and their area is small
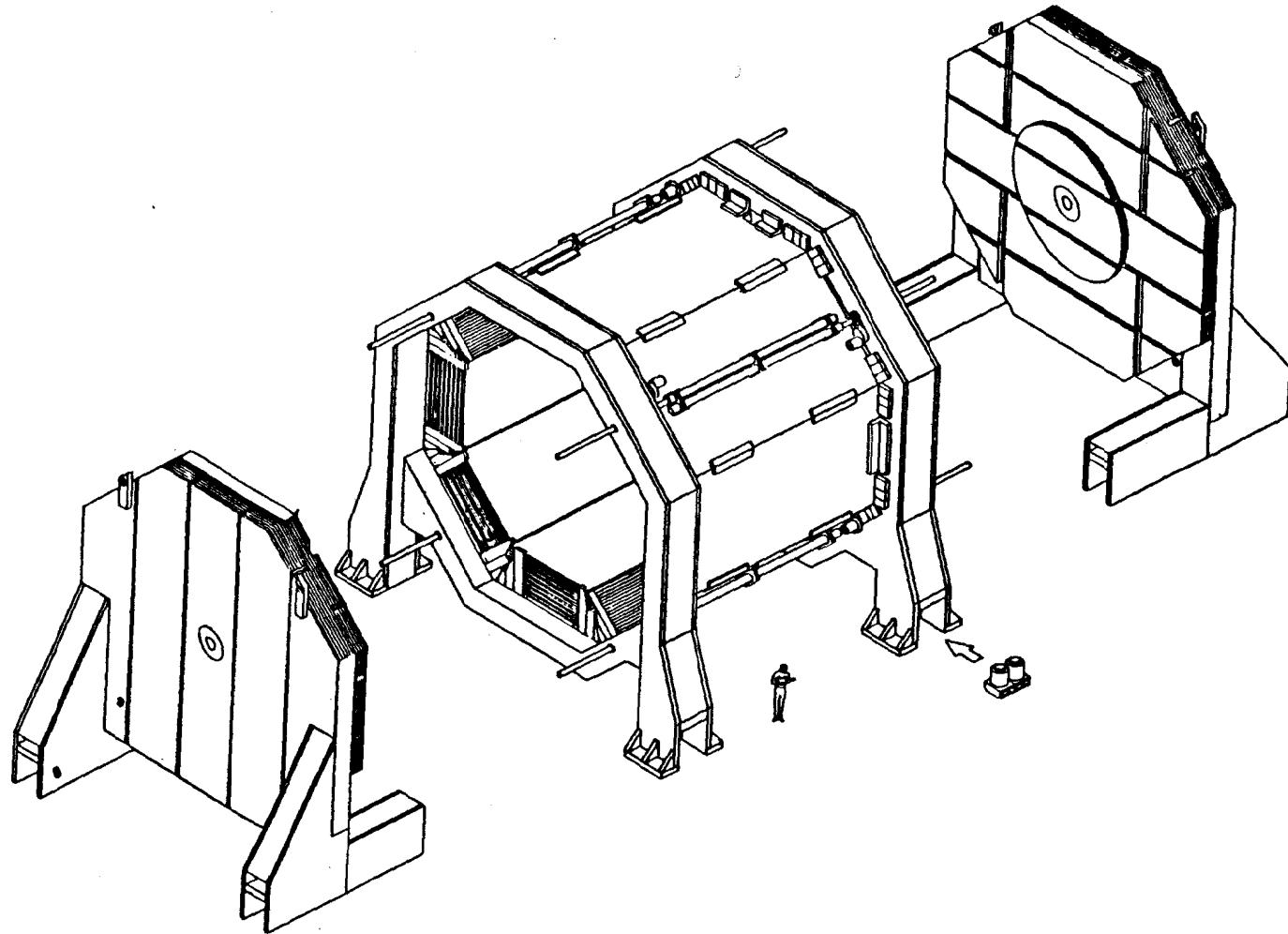
Figure 4.1. Isometric view of the *SLD*.
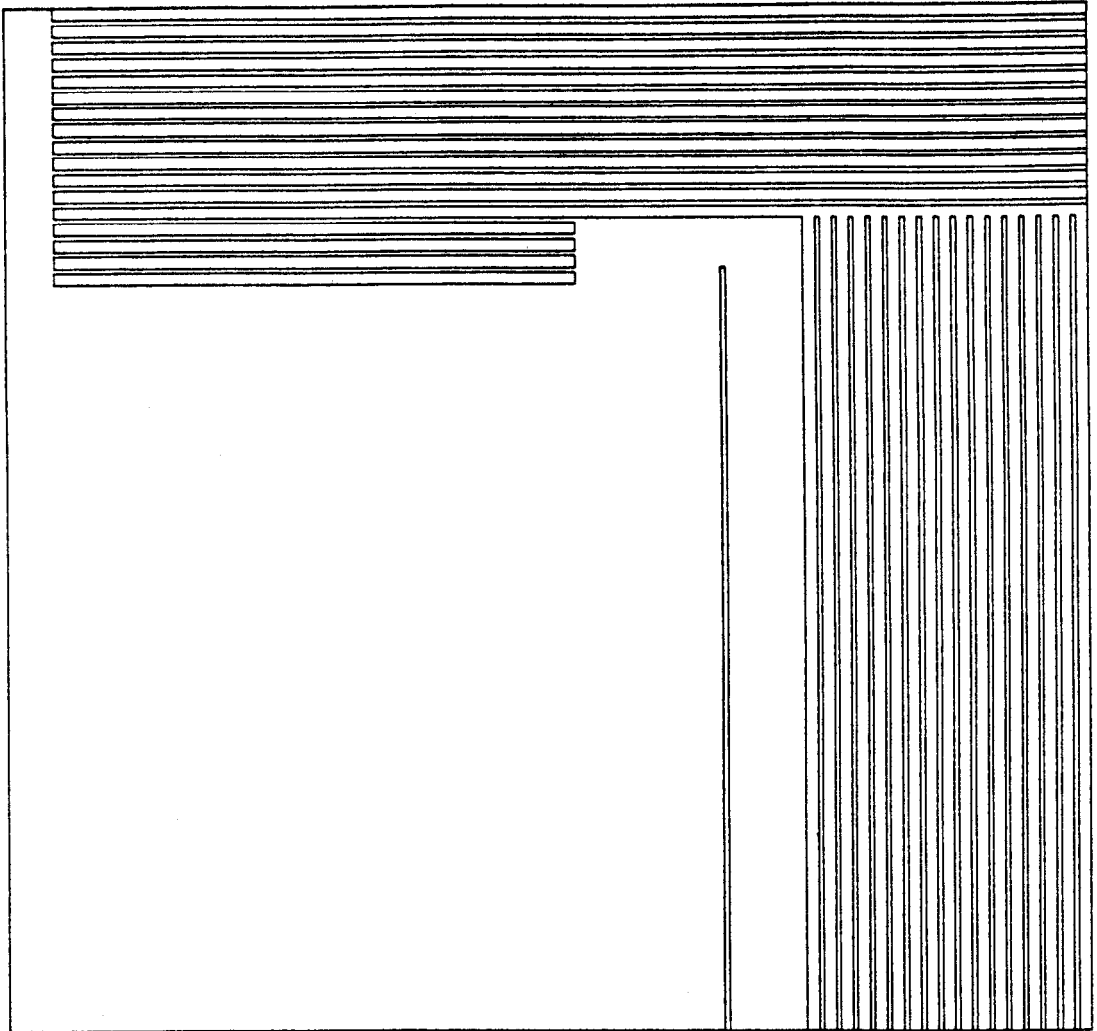
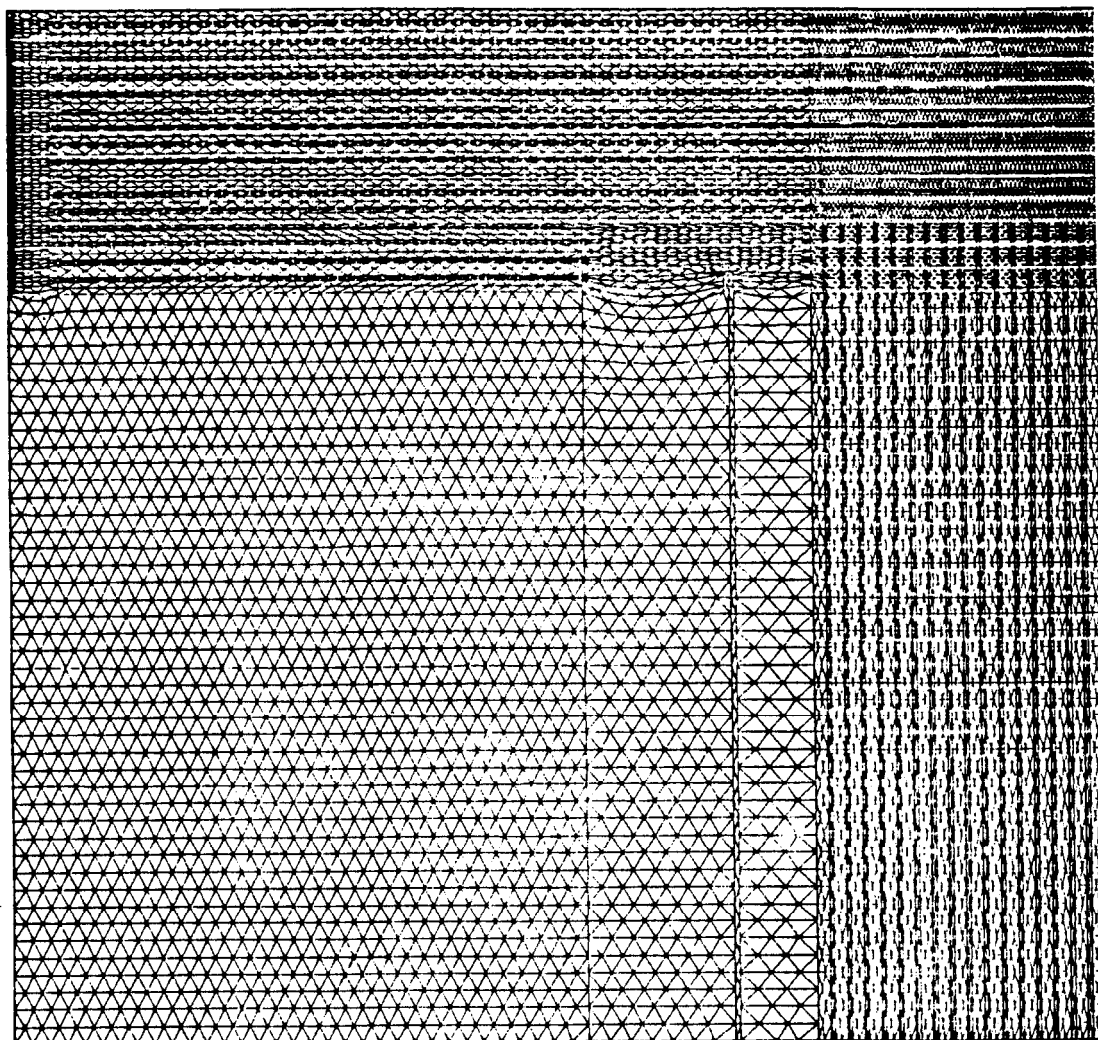Figure 4.2. Configuration for finite element analysis of the *SLD* static magnetic fields.
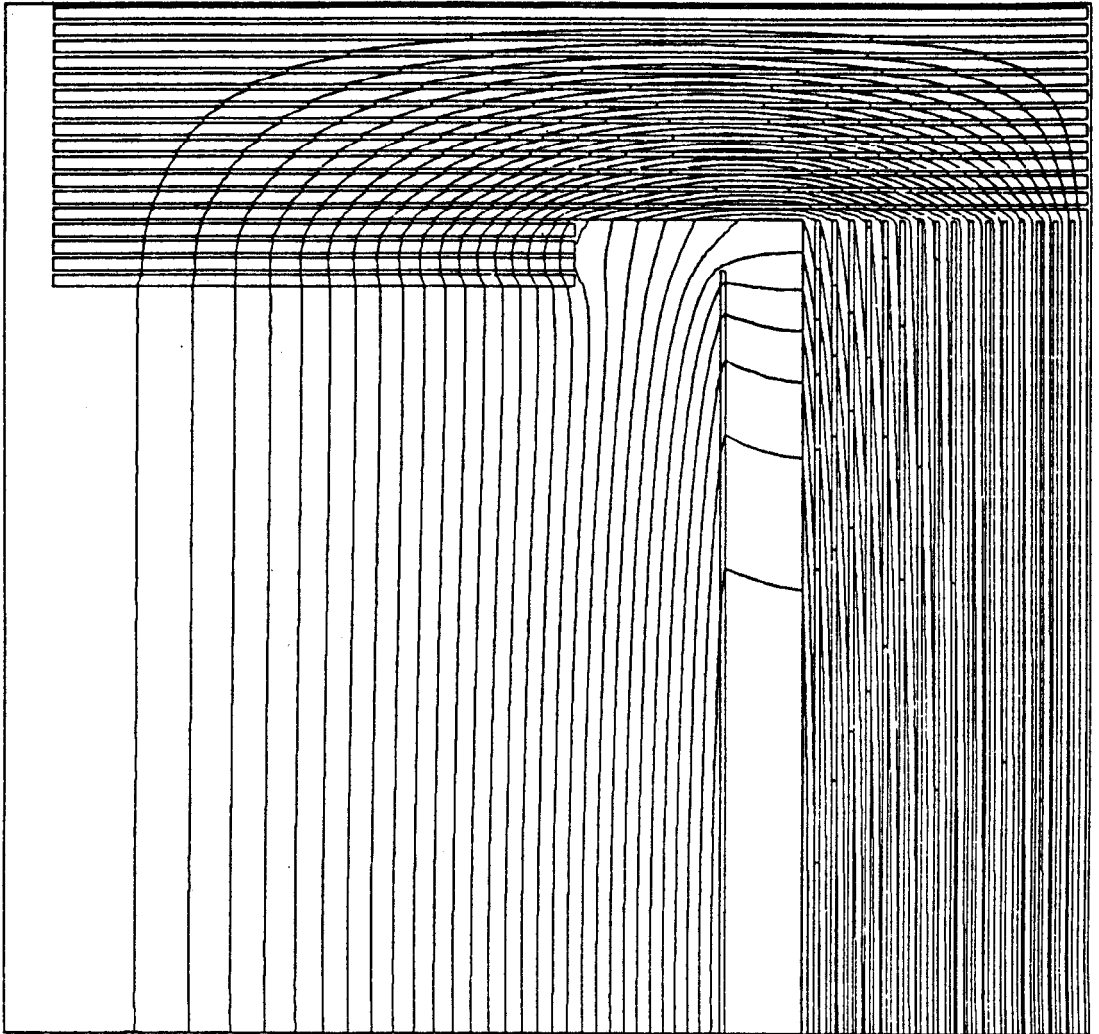
Figure 4.3. Grid used for the finite element analysis.

Figure 4.4. Field homogeneity in the magnet bore for the laminated pole case.

compared to the overall door area, the laminated model shown is thought to be a conservative representation. A flux plot using this model is given in Figure 4.4.

Extending the ends of the superconducting coil into the end doors reduces the radial field to that required by the *CRIDs*. The first four door laminations are made with a reduced diameter of 4.72 meters, allowing them to extend inside the coil. The resulting field integral defined earlier is less than 60 gauss-meters. When the inner four laminations are replaced by a solid plug, this integral is reduced to less than 30 gauss-meters, indicating that magnetic coupling should not produce a problem with field quality inside the detector.

The total dipole moment of the coil alone is 1.5×10^8 ampere-meter^2. While the iron provides an effective return for the magnetic flux, it will not shield all of the dipole moment and there will be fringe fields. The fields can be approximately determined using the results of the initial finite element field analysis. Although the results must be considered preliminary because the grid external to the magnet was very coarse for the initial studies, it appears that the iron shields 90% of the dipole moment. Far from the magnet the fringe fields will appear to be produced by an ideal three-dimensional dipole with a moment equal to about 10% of the unshielded value, or 1.5×10^7 ampere-meter^2. Figure 4.5 shows the fringe fields as a function of distance from the magnet center, along the radial direction and along the axis.

4.2.2 Static Magnetic Forces

The forces on the coil have been determined from the field analysis. A simplified analysis estimates both axial and lateral displacement forces, expressed as equivalent spring constants. The results are given in Figure 4.6 for the radial case, and Figure 4.7 for compressive forces; these are the integrated axial body forces starting at the end of the coil, and indicate the distribution of compressive loads within the coil.

If the coil is not perfectly centered within the iron, magnetic forces will tend to increase the displacement. Detailed three-dimensional computer modeling is required to determine these displacement forces, but a rough estimate gives 40,000 pounds per inch of axial displacement and 250,000 pounds per inch of
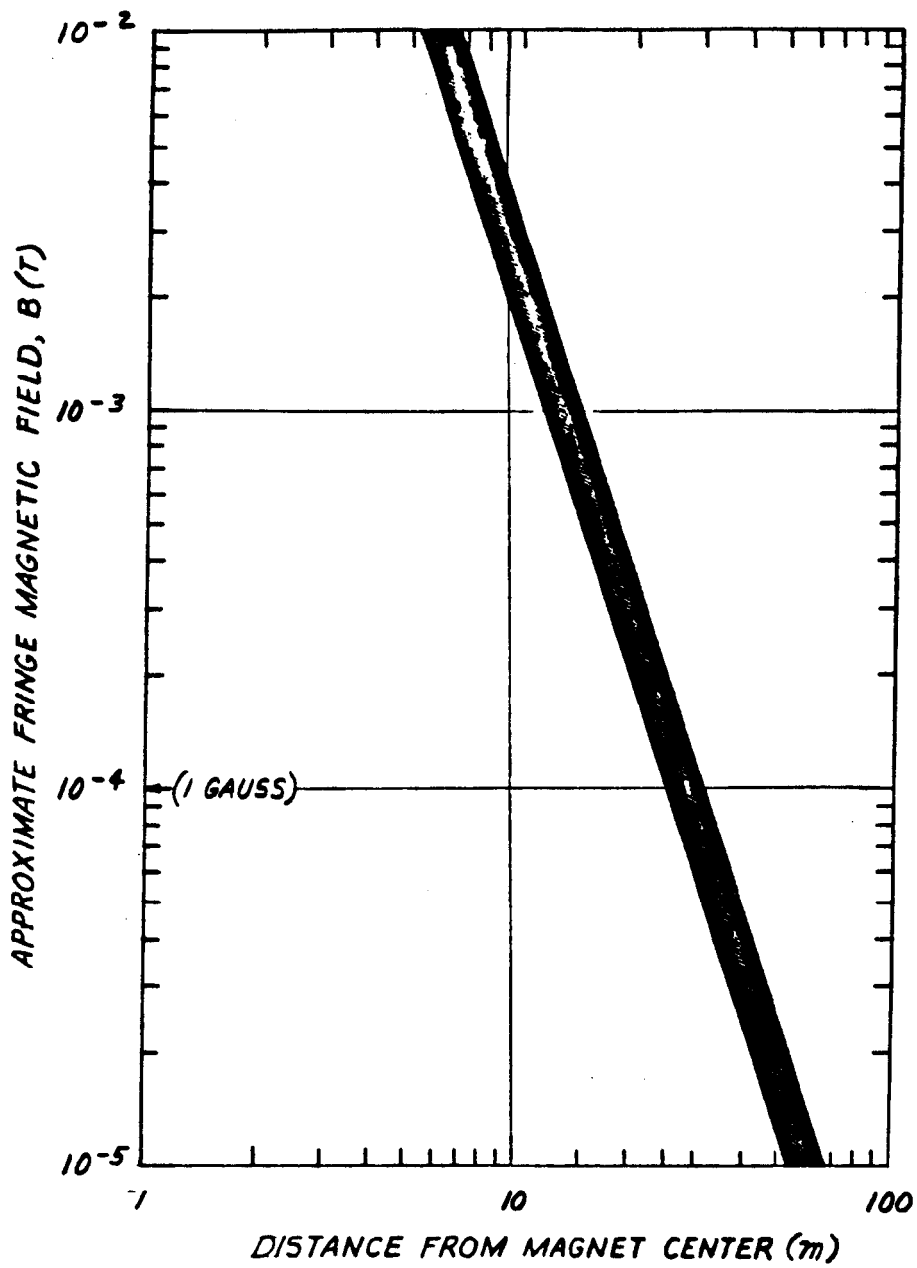
Figure 4.5. Approximate fringe magnetic fields as a function of distance from the center of the magnet.
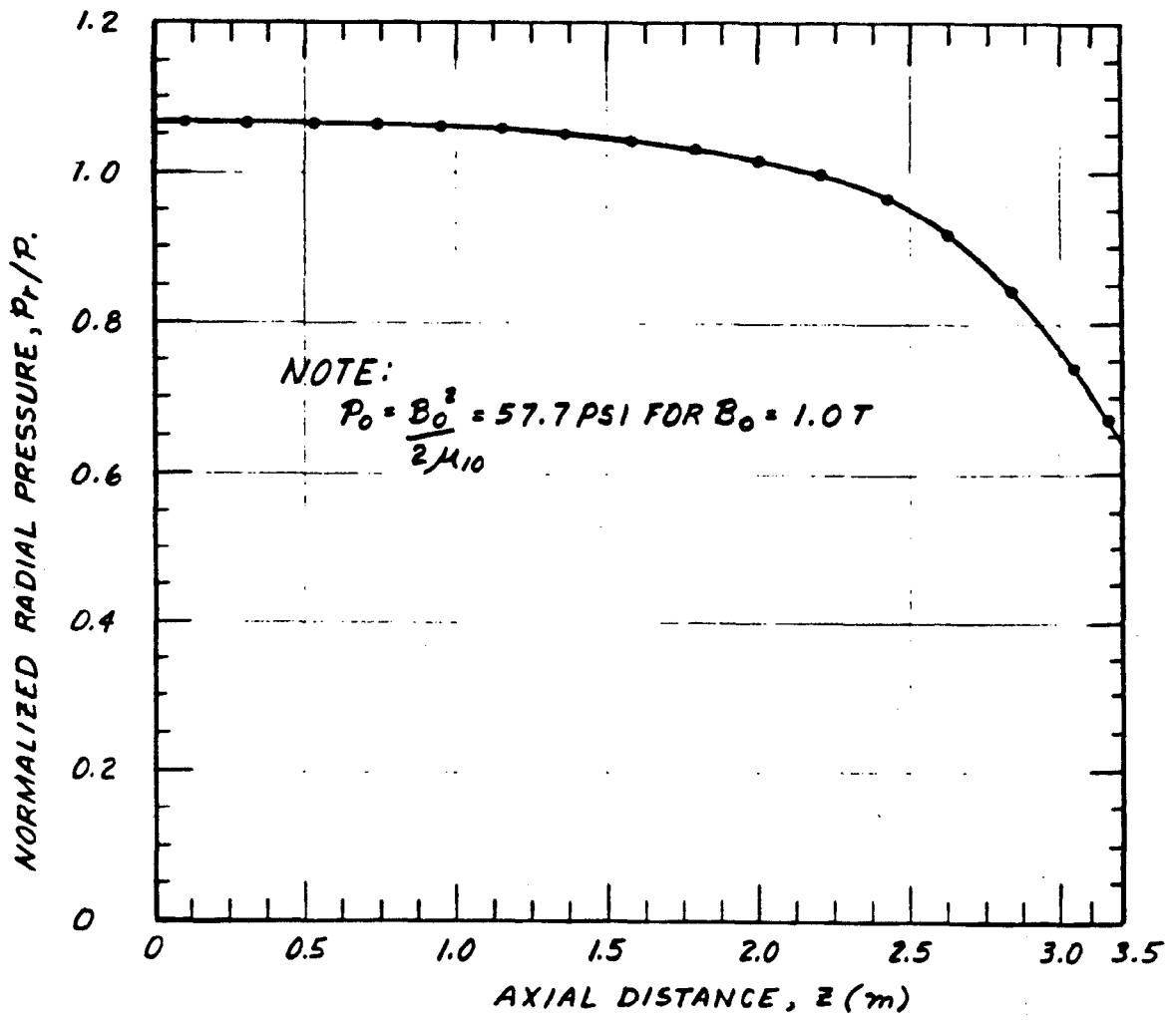
Figure 4.6. Radial force distribution on the main coil.

4 - 8
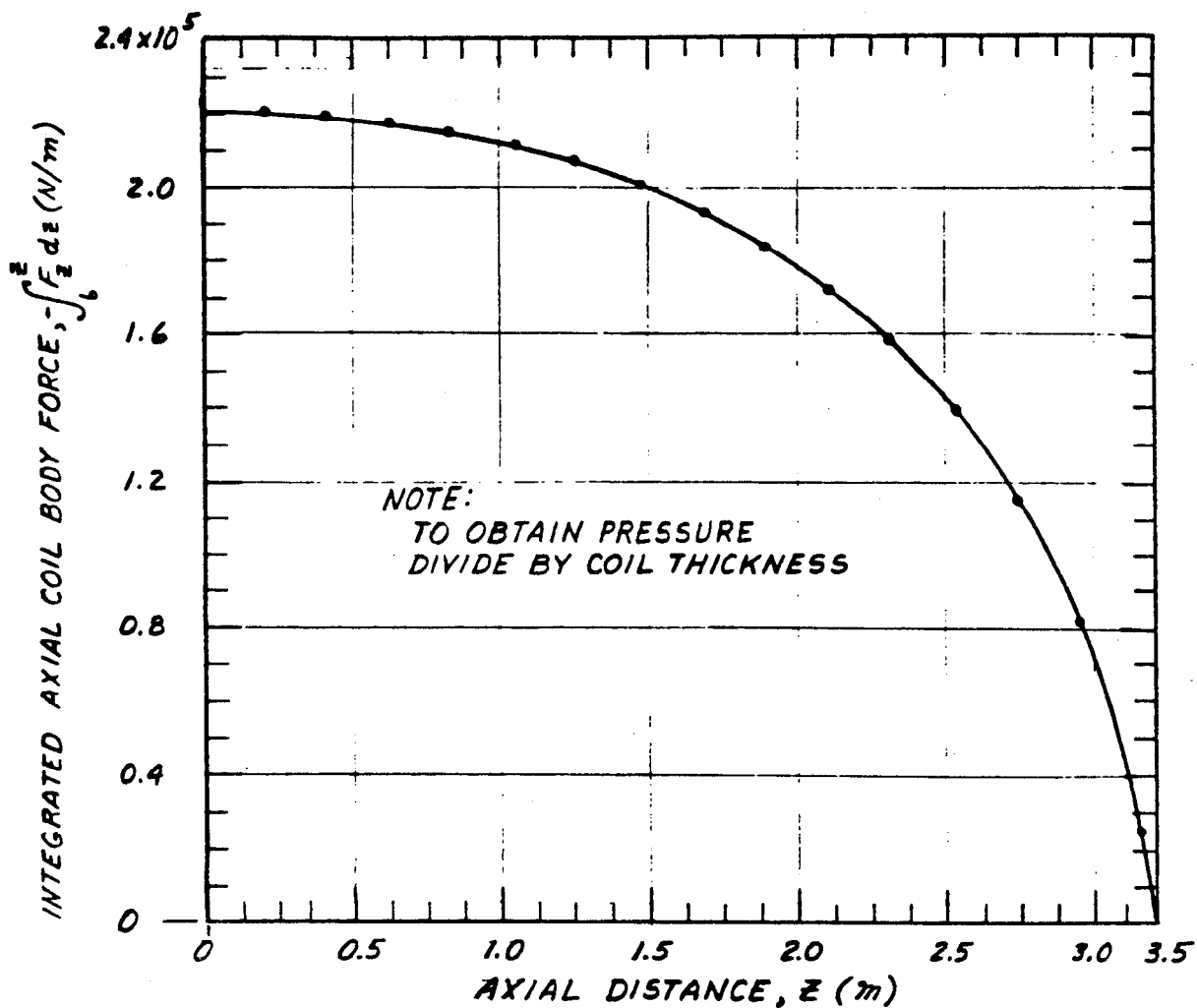
Figure 4.7. Integrated axial coil forces on the main coil.

lateral displacement.

4.3 THE SUPERCONDUCTING COIL

4.3.1 Specification of Parameters

The superconducting coil should provide an axial field (parallel to the $e^{\pm}$ beam direction) of 1.0 Tesla. The coil will be a solenoid about 5.8 meters diameter and 6.2 meters long. The vacuum vessel housing this coil will have an inside radius of 2.80 m, a maximum outside radius of 3.28 m, and a length of 6.84 m. A total of 5.3×10^6 ampere turns will be required. Thus, for example, a conductor pitch of ~ 6 mm implies about 1000 turns and a current of 5300 amps.

4.3.2 Design Considerations

One of the most important considerations in the design of the superconducting coil is the method of cooling the superconductor. Typically, three methods have been used in the past for large superconducting coils: bath cooling, indirect cooling, and internal cooling.

Bath-Cooled Conductors

In this method the superconductor is actually immersed in a bath of liquid helium. Thus, the conductor is in thermal contact with the liquid helium and the cooling is sufficient that such coils can be made cryostable, i.e., if a small section of conductor goes normal, the heat generated by i^2R losses can be removed by the liquid helium and the conductor returns to a superconducting state. Examples of successful coils built on this principle are the coils for the *LASS* spectrometer at *SLAC* and the large bubble chambers *BEBC*, the 7-foot, the 12-foot, and the 15-foot chambers.

In large collider detectors, the helium bath vessels need to have thick walls and large emergency vents in order to protect the structure from the helium gas pressure in the case of an unexpected temperature rise. For this reason, recent collider detectors which require a thin coil have not used cryostable bath-cooled coils. In the case of the *SLD* design, however the electromagnetic calorimeter and the first three interaction lengths of the hadronic calorimeter are inside the coil, so it is not of prime importance to minimize the thickness of the coil package.

A detailed comparison of the bath-cooled and indirectly-cooled approaches for *SLD* is underway.

Indirectly Cooled Conductors

In these designs, the conductor is wound on or inside of a large aluminum cylinder. The cylinder is cooled by circulating liquid helium through attached cooling loops. Thus, the superconductor is not in direct thermal contact with the liquid helium and the cooling is less effective than in the case of the bath-cooled designs. However, coils less than one radiation-length thick can be built this way. The design is less complicated than those for bath-cooled coils.

The main risk in the indirectly cooled design is the relatively low energy margin, i.e., fairly small amounts of energy deposited in a limited region of the coil are enough to cause a quench. If there are imperfections in the mechanical rigidity of the coil, frictional heating generated by small coil motions could be critical. It is a quantitative question then just how much frictional heating, distributed over how large a volume of coil, is required to quench the coil. Some preliminary calculations, and some actual measurements carried out in Japan,[1] indicate that as much as ten joules, spread over a region of the order of one meter long and several turns wide, can be tolerated. This places severe, but probably achievable, requirements on the overall mechanical integrity of the coil.

No indirectly cooled coils as large as the one contemplated for the *SLD* have been built before. However, coils about half this size have been built for the *CELLO* and the *CLEO* detectors. Both of these coils have operated successfully, but somewhat below their design fields. Their problems do not seem to be related to quenches caused by coil motion. Another indirectly cooled coil has been built for the *CDF* detector, and is scheduled to be tested in the near future. The results of these tests will be of great interest. The coils for the *ALEPH* and *DELPHI* detectors in Europe and the *VENUS* and *TOPAZ* detectors in Japan are also based on indirect cooling, and are important in the *SLD* coil design.

Internally Cooled Conductors

In these designs, liquid helium is circulated through apertures inside the conductor, much as water is circulated through holes in conventional warm copper

conductors. The cooling is very efficient in this case since the superconductor is in good thermal contact with the liquid helium; thus, internally cooled conductors should be more stable against quenches than indirectly cooled conductors.

It may not even be necessary to circulate the liquid helium inside the conductor. A stationary volume of liquid helium trapped inside the conductor may be used to increase the enthalpy of the conductor to provide a large energy margin, and cooling might be provided indirectly.

A design study[2] specifically for the *SLD* coil has been carried out by the *MIT* magnet lab based on internal cooling using the *ICCS* conductor (Internally Cooled Cabled Superconductor). The *ICCS* cable consists of NbTi and copper stabilizing wire with a Cu:NbTi ratio of 26:1. This cable is enclosed in a stainless steel sheath of 1.65 mm wall thickness to make a conductor of 1 inch $\times$ 1 inch external cross section. About 32% of the volume inside the stainless steel sheath is void, to be filled by the liquid helium coolant. The coil is a single layer of 250 turns of this conductor wound inside a 1/2-inch-thick aluminum cylinder. Cooling loops are attached to the outside of the aluminum cylinder for additional cooling to be used especially during cooldown. A current of 21,000 amps would be needed to provide the 1.0 Tesla field. This design seemed very attractive from the point of view of efficient cooling by virtue of the direct contact between the liquid helium and the superconductor. However, after discussion with a number of other magnet experts, several questions have been raised about this design.

4.3.3 Timetable Major Coil Design Decisions

The *MIT* magnet lab design study for an internally cooled coil for the *SLD* was completed in April of 1984. A design comparison of a bath-cooled and an indirectly-cooled coil for the *SLD* will be completed by September of 1984. An *RFP* (Requests for Proposal) for the design and construction of the *SLD* coil will be released to industry in September 1984 permitting selection of the appropriate design and construction proposal by November of 1984.

4.4 MAGNET YOKE

4.4.1 General Description

The magnet yoke, shown earlier in Figure 4.1 consists of a laminated barrel, 2 laminated end doors, and 2 independent support arches. The barrel is a modified octagon made up of 24 trapezoidal sections. This geometry avoids the radial cracks which would degrade the performance of the detector. Each of the octagonal sections are split into three parts in order to meet the 100-ton handling capacity of the crane in the central experimental hall. Each of these sections is independently supported from the support arches. The complete assembly of barrel and support arches weighs 1700 metric tons.

The laminated end doors are designed in vertical and horizontal box beam sections to take the magnetic loads. These box beams are welded together to form the complete doors. When completely assembled the door weighs 680 metric tons. The design of the door is such that it derives its position relative to the barrel from accurate registers located on the lower half of the support arches. Rapid access to the interior of the detector is obtained by motorized ball-screws mounted on the barrel and connected to the end doors. Pressurizing the end door jacks takes the end door weight off the support arch registers and puts it on the end door roller assembly. Activating the ball screws then drives the door away from the barrel.

4.4.2 General Construction

The flux return path is composed of two endcaps and a barrel section of roughly octagonal shape. The total assembly is supported by two complete and independent arches which also provide the structural support for the solenoid and all the internally located detectors.

A finite element stress analysis program called SAP was used in the arch design. A sample grid for this analysis is given in Figure 4.8. The resulting stresses and corresponding deflections are given in Figures 4.9 and 4.10.

The yoke, barrel, doors, and arches will be pre-assembled at the point of manufacture, taken apart, and re-assembled in the central experimental hall in

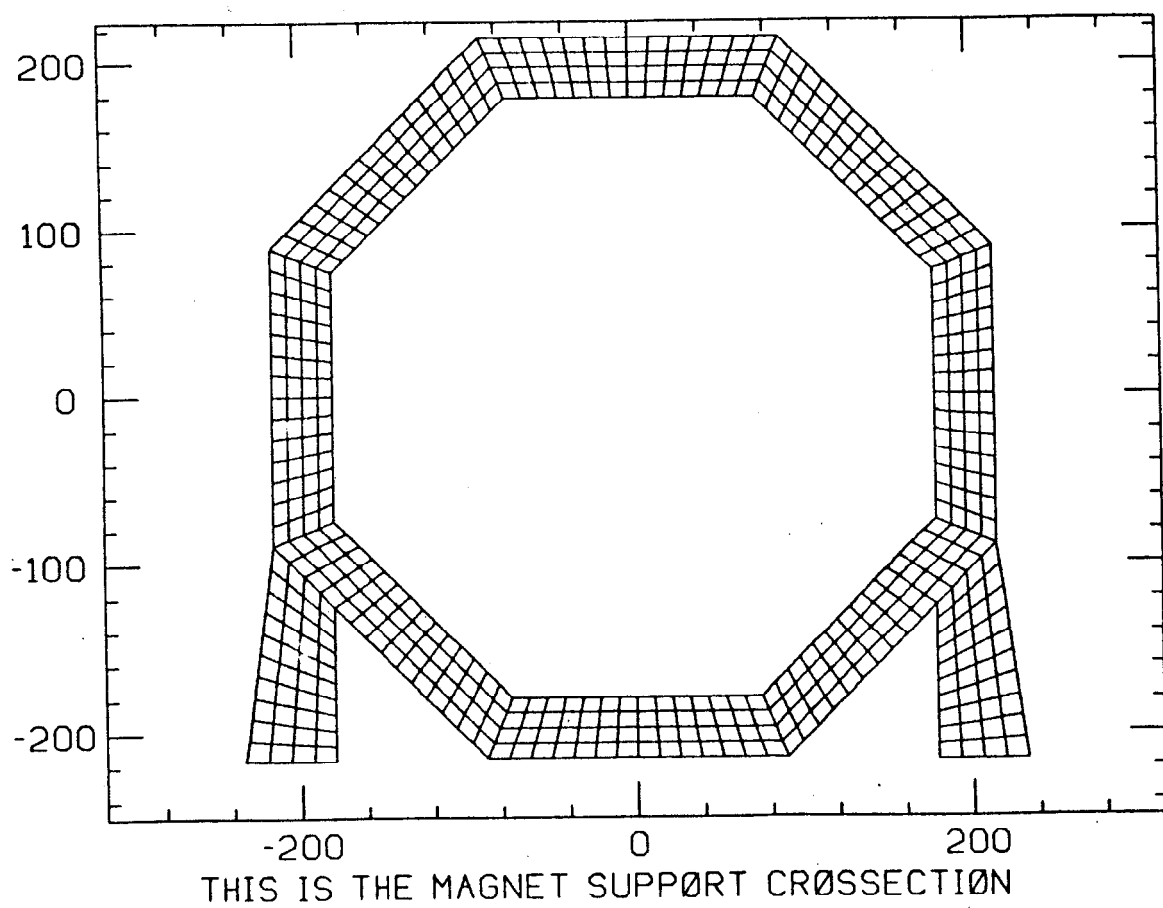THIS IS THE MAGNET SUPPØRT CRØSSECTIØN

Figure 4.8. Sample grid used in finite element stress analysis of *SLD* arches.
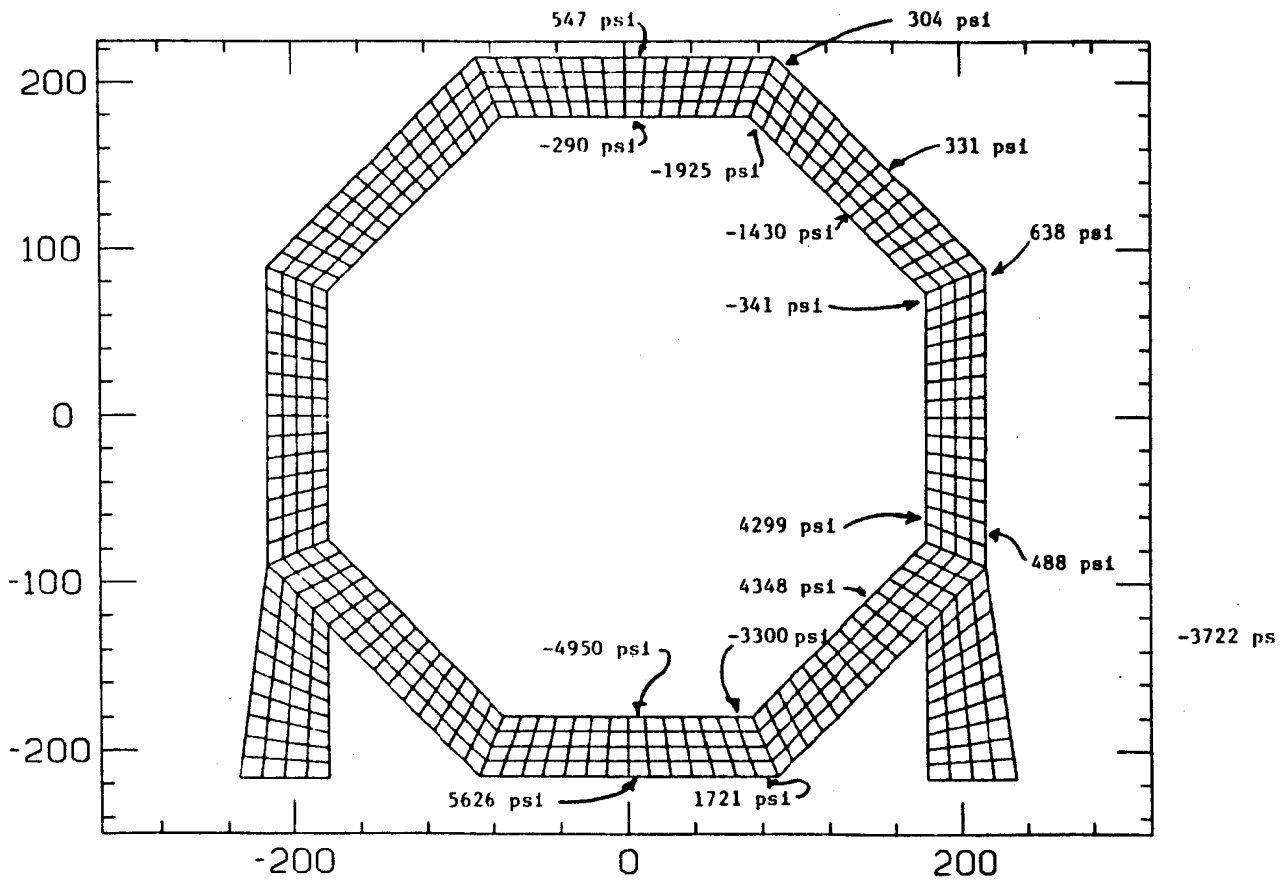
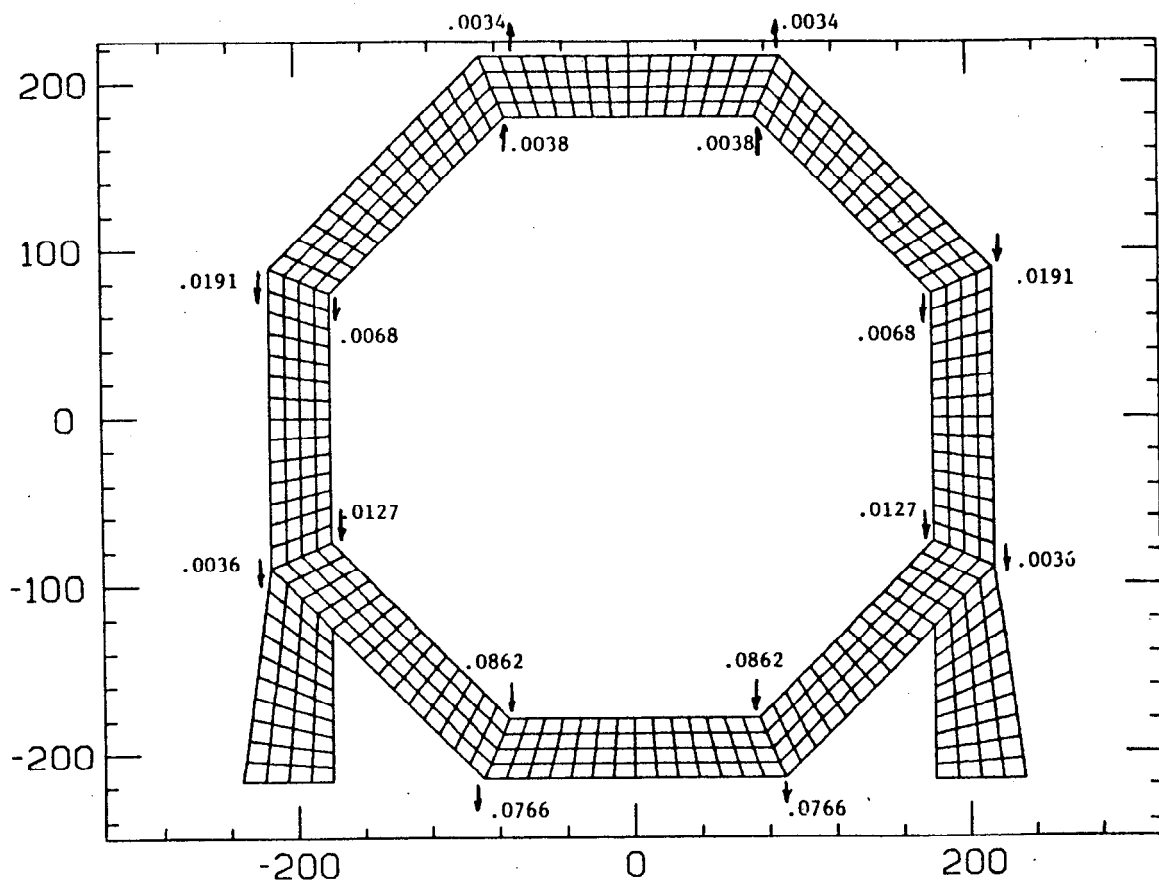Figure 4.9. Typical stresses in *SLD* arches.

Figure 4.10. Typical deflections in *SLD* arches.

order to minimize the work in the pits.

A detail of a typical corner joint of the octagonal barrel section is given in Figure 4.11. This arrangement leaves no radial cracks to degrade the physics performance of the detector and provides self-shielding.

Each of the eight parts will be built up from three subsections, each making up approximately one third of the thickness. This design allows the use of rectangular plates to the greatest extent and also provides large prismatic apertures with permanent access from both ends to the calorimeter elements in the gaps.

The endcaps are assembled from sections weighing less than 70 tons each. These sections also have rectangular cross sections and are designed to support the total force produced by the magnetic fields on each of them. This reduces the number of mechanical fasteners which must be used between individual sections in assembling the endcaps. These sections will be fabricated and machined externally to eliminate cracks between counters and to provide the required fit against the barrel sections.

The endcaps will be assembled vertically in the pit using a special fixture and then moved on individual rollers-supports for final assembly to the barrel section.

In the assembled position the endcaps rest inside the arches and the endcap weight is then transferred from the endcap supports to the arches. When the magnet is assembled, the two support arches carry all the weight of the magnet iron, solenoid, detectors, shielding and superstructure. All this load is in turn transferred to four sets of roller bearings through hydraulic jacks in the feet of the arches. Standard roller bearings provide translation; special tapered rollers will be substituted to allow rotation of the magnet. The arches carry directly the weight of the solenoid and the liquid argon calorimeter (LAC) through vertical support members at each end of the solenoid. These vertical supports have corresponding vertical cutouts in the endcaps. Lateral loads caused by earthquake loading cannot be absorbed by the vertical members and are absorbed sideways by the vertical members in their slots.

The detector is designed to be self-shielding, so that access will not require
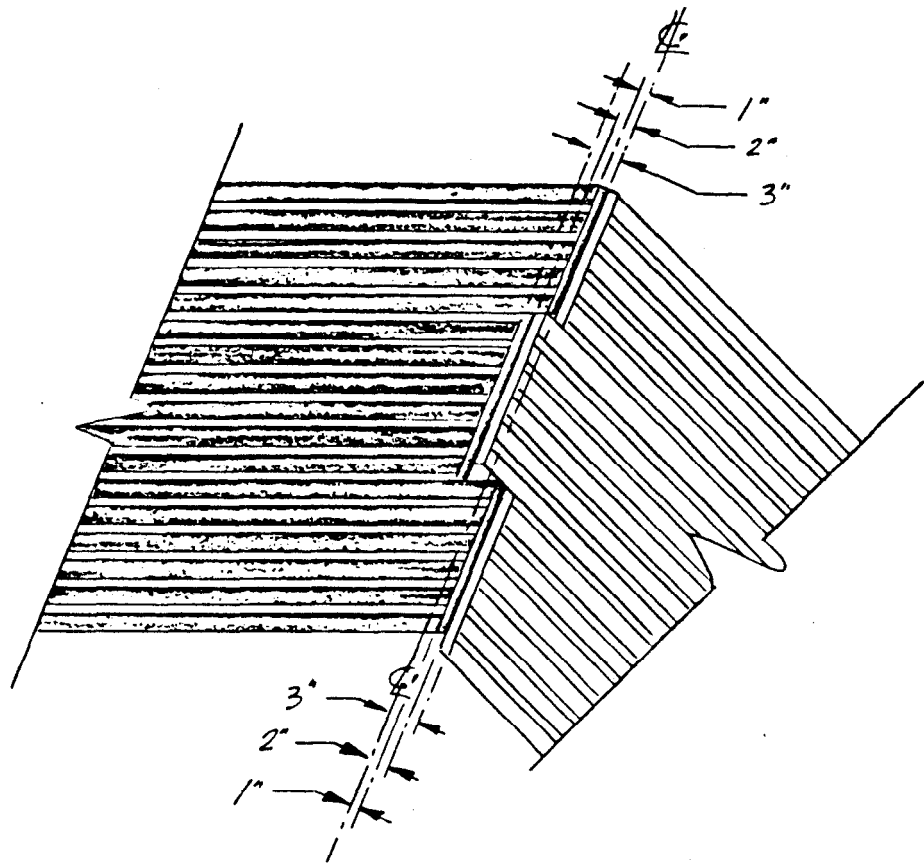
Figure 4.11. Detail of typical corner joint in barrel section.
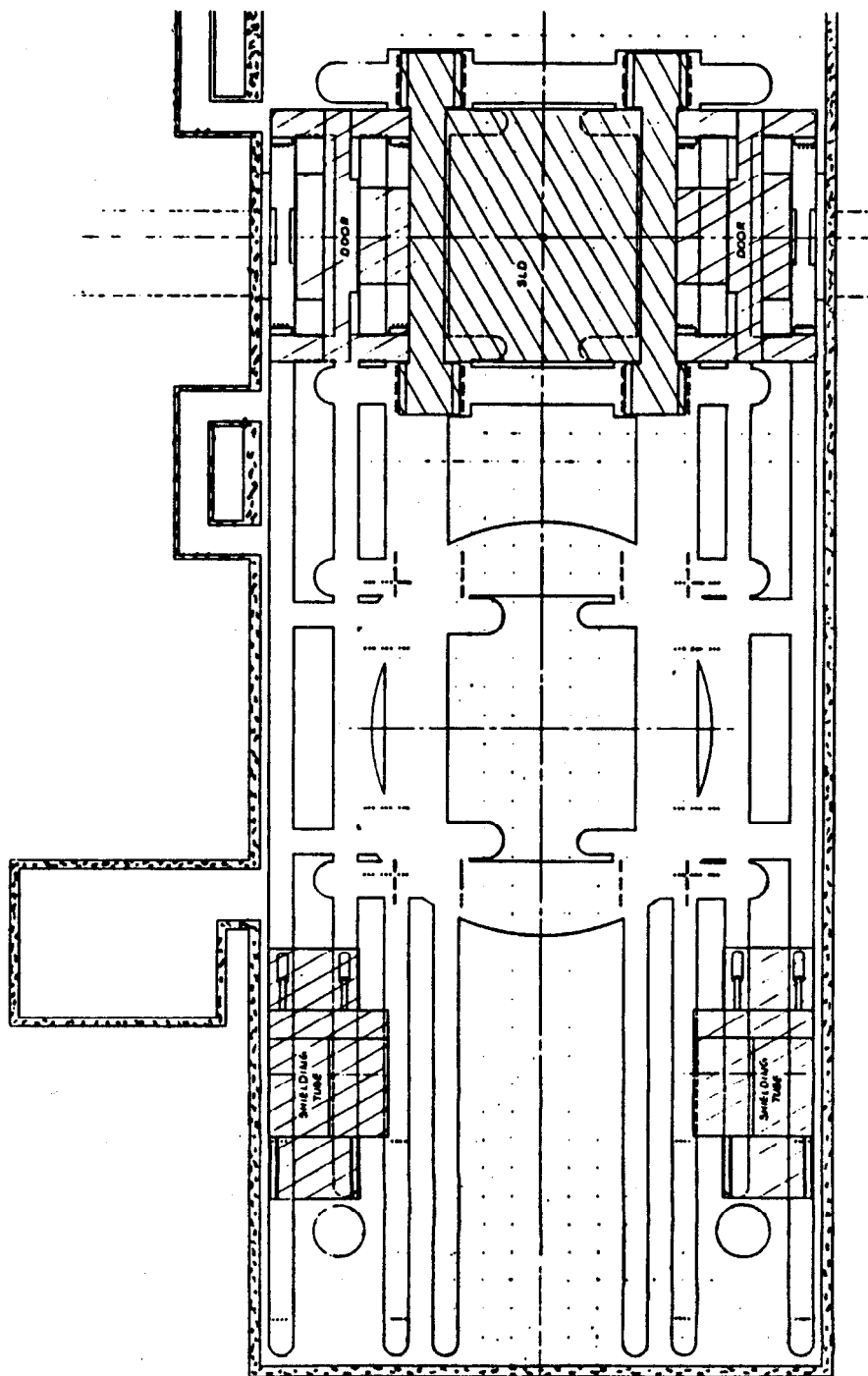
Figure 4.12. *SLD* opened for minor servicing on beamline.

the disassembly of large shielding blocks. Although this reduces the time lost for repairs and maintenance, it complicates access to the interior of the detector. A split concrete tube between the detector and the experimental pit walls shields the collider final focus components and allows detector access in the operating position. When the two halves of the tube are separated and moved off beamline, the doors can be moved along the final focus pipe 3 or 4 meters allowing access to the interior of the detector as shown in Figure 4.12. To minimize downtime, the door opening will be guided and motorized so a small crew can open the detector without calling in riggers and surveyors.

In all locations where the components will remain for more than a few days, provision for 'tie-down' must be made to prevent overturning or translation of components during an earthquake.

4.5 References

1. H. Hirabayashi et al., Japanese Journal of Applied Physics, Vol. 21, 1149 (1982).

2. P. Marsten et al., "*SLD* Superconducting Magnet Conceptual Design Report," prepared for the *SLD* collaboration by the *MHD* and High-Energy Physics Magnet Design Group of the Plasma Fusion Center at *MIT*.

5. TRACKING

The goal of the *SLD* tracking system is to reconstruct charged-particle trajectories. The understanding of any process, as well as the usefulness of the Čerenkov ring imaging devices and the calorimeters, hinges upon the accuracy and efficiency with which tracks are resolved. In order to measure trajectories over a wide range of momentum and 95% of the solid angle, the *SLD* tracking detectors include: i) a charge-coupled device vertex detector immediately adjacent to the the beam pipe with a space resolution of $\sigma = 5~\mu$m; ii) a central drift chamber occupying radii between 20 and 100 cm with 80 layers of sense wires and $\sigma = 100~\mu$m; and finally, iii) endcap drift chambers that complete the forward and backward cones tracking acceptance to angles of 15° to the beam axis. This chapter gives a detailed discussion of these elements.

5.1 VERTEX DETECTOR

With suitable masking against synchrotron radiation, the *SLC* beam pipe will allow detectors to be placed as close as 10 mm from the vertex. As such, it offers opportunities unique among colliding beam machines for the detection of short-lived particles. In order to resolve the individual tracks within a jet so close to the vertex, a detector that provides 2-dimensional readout is essential. Solid-state detectors have superior precision, and mosaics of silicon charge-coupled devices (*CCDs*) will provide a measurement of 2 points on each track for a precise reconstruction of vertices.

The general arrangement is shown in Figure 5.1. *BP* is the beam pipe of radius 8 mm. *M3* is one option for the innermost synchrotron radiation masks. Surrounding the interaction point (*IP*) are two concentric arrays of *CCD* detectors (*B1* and *B2*, of length 60 mm on radii of 10 and 20 mm respectively). Particles with angles greater than 34° to the beam axis are tracked in each of these barrel detectors, allowing an extrapolation to the vertex with impact parameter precision of typically 10 μm in both z and $r\phi$. Between 18° and 34° the particles are seen in *B1* and one of the endcap *CCD* detectors *EL* or *ER*, allowing a measurement of the impact parameter with similar precision. Below 18° there is no tracking information provided by the *CCDs*.
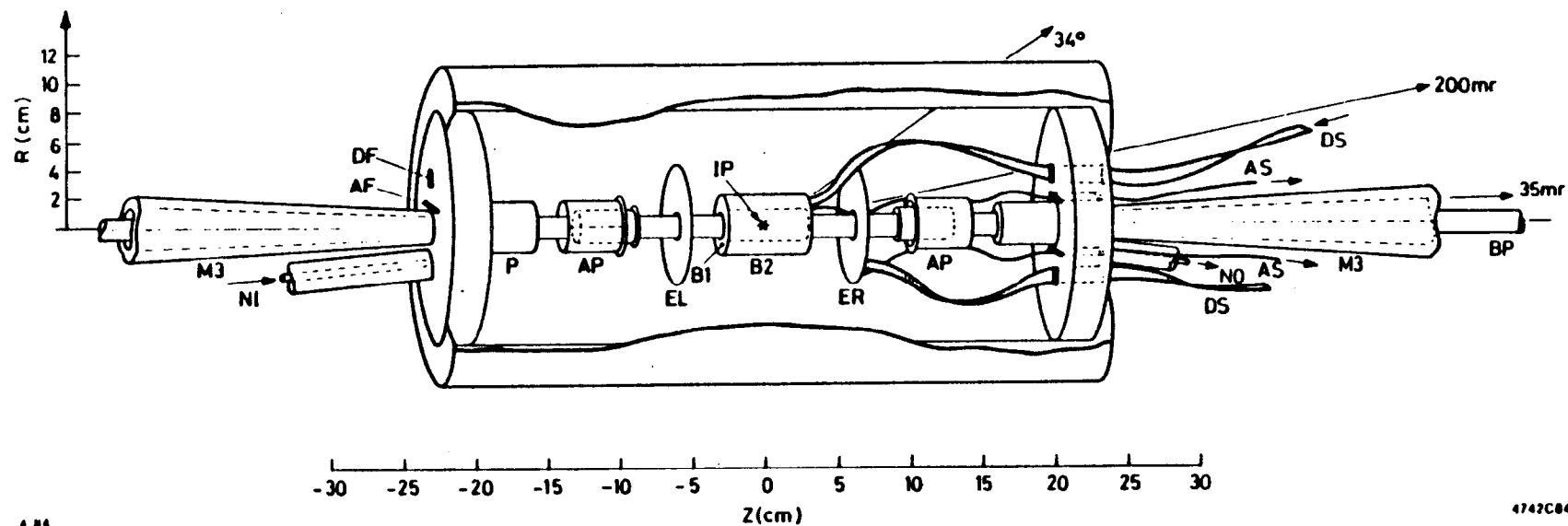
Figure 5.1. General arrangement of *SLD* vertex detector.

5.1.1 Description

The *CCD* detectors need to run at a temperature of less than 200 ° K. This is achieved in a low-mass atmospheric pressure enclosure of cellular material, blown with cold nitrogen gas via tubes *NI* and *NO*. Plugs P reduce the heat leaks from the beam pipes, and the external volume (i.e. the inner aperture of the central drift chamber) is blown with dry nitrogen at room temperature in order to avoid problems of external condensation around the vertex detector.

Down to a polar angle of 200 mrad, particles traversing the vertex detector see only about 0.015 radiation length of material. There are of necessity somewhat more massive items (preamplifiers, feed-through connectors) which need to be mounted locally, but these are confined to angles below 200 mrad. *AP* are concentric rings of hybrid preamplifiers which receive the signals from both the barrel and endcap *CCDs*. The preamps include line drivers which transmit the signals down miniature coax cables (*AS*) to the external electronics. The *CCD* drive pulses are generated externally and fed to the detector down flat profile bunches of transmission lines *DS*.

The *SLD* will use the P8600 *CCDs* manufactured by the *GEC* Company (*UK*), which have good efficiency[1] ($> 98\%$) for minimum-ionizing particles, high precision ($\sigma_x \approx \sigma_y \approx 5$ μm) and good 2-track resolution (40 μm spatial separation between tracks at the detector). Each *CCD* covers a sensitive area of approximately 9 $\times$ 13 mm^2 (385 $\times$ 578 pixels, each pixel 22 μm $\times$ 22 μm); the physical chip area is about 20% larger. In order to cover the area of *B1*, *B2*, *EL* and *ER*, 220 *CCDs* will be used. Mosaics on this scale have not previously been attempted for particle detectors, but are beginning to appear in the imaging field for large area focal-plane detectors. *GEC* will be manufacturing high quality chips in the required numbers for use in astronomy and high-energy physics by the end of 1985. In total, the vertex detector comprises 50 $\times$ 10^6 pixels, each one of which can in principle carry its own particular pulse height. Although the capacity exists to swamp the data acquisition system, experience has shown that good quality *CCDs* are intrinsically extremely low-noise detectors. Nevertheless, special electronics must be developed to read out the full detector system on a

Table 5.1.
Vertex Detector: Table of Parameters

Individual CCDs

Pixel size	22 μm $\times$ 22 μm
Active area	385 $\times$ 578 pixels (8.47 $\times$ 12.72 mm^2)
Total number of pixels	223 $\times 10^3$
Depletion depth	8 μm [effective thickness of silicon for charge collection = 16 μm]
Minimum Ionizing signal	$\sim$ 1300 electrons (Landau peak)
Efficiency for Min-I particles	$>$98%
Mean cluster size	Very threshold-dependent, but 80% of charge is in two strongest clusters.
Precision in x and y	4–6 μm (from cluster centroids)
Readout time	50 ms
Clearing time (after unwanted beam crossing)	1.5 ms

Individual Ladders

Number of CCDs per ladder	5
Active area	8.47 $\times$ 60.0 mm (CCD active areas are overlapping)
Materials for normal incidence	6.1 $\times 10^{-3}$ radiation length

Complete Detector

Barrel B1:	Radius	10 mm
	Length	60 mm
	Number of Ladders	8
	Number of CCDs	40
Barrel B2:	Radius	20 mm
	Length	60 mm
	Number of Ladders	16
	Number of CCDs	80
Endcaps EL and ER:		Positioned at z = $\pm$ 60 mm
	Inner Radius	12 mm
	Outer Radius	40 mm
	Number of CCDs	100 (50 per Endcap)
Coverage:	Impact Parameters	Down to $\theta = 34°$ with B1 and B2
		Down to $\theta = 18°$ with B1 and EL/ER
	Tracking	$\theta = 11°$ with EL/ER only
Readout and clearing times		As for individual CCDs (run entirely in parallel)
	Material	Typically 2.1 $\times 10^{-2}$ radiation length

reasonable timescale. The *CCD* vertex detector parameters are given in Table 5.1.

5.1.2 Mechanical Layout

If the *CCD*s were arranged in a single-sided mosaic, there would be relatively poor coverage due to the dead area around the periphery of each chip and due to the further space required for bond pads on the substrate around each chip. These dead areas can be eliminated by bonding the chips on alternate sides of a ceramic or quartz strip to form a ladder in such a way that there is a small overlap between the sensitive areas of upper and lower *CCD*s. The strips carry thick-film traces on both surfaces which present the appropriate set of bonding pads for each *CCD* in the ladder (Figure 5.2).

The bias levels and drive pulses are all fed in at one end of the ladder on a lightweight strip connector and are then distributed to the *CCD*s in parallel along the ladder.

The physical connections from the pads to the *CCD*s are standard wire bonds. The uniformity of specifications among individual *CCD*s allows the parallel biasing with insignificant loss of efficiency, charge-transfer efficiency, etc. The 5 analog outputs from the *CCD*s on the ladder are brought back to the end of the ceramic strip using a multi-layer thick-film trace technique and fed via thin coax cables to the local preamplifiers. Neighboring *CCD* ladders overlap (Figure 5.3) to preserve azimuthal coverage. Note that this arrangement would allow modification in the radius of *B1* or *B2* if experience led to some other preferred geometry. The mechanical support for the barrels will be a pair of thin quartz 'bicycle-wheels' at either end of the assembly. The endcap detectors (Figure 5.4) are constructed in an arrangement of overlapping ladders with 3 or 4 *CCD*s.

The leads (strip-lines and coax cables) are permanently connected at the ladder end, but are push-fit at the preamp or end wall of the cryostat. Disassembling the detector to change a ladder will be a straightforward process once the vertex detector is removed from the spectrometer. Individual *CCD*s would not be exchanged; complete ladders constitute the natural unit of spares. In the event of major *CCD* failure, such as an inter-gate short, at worst a single ladder would
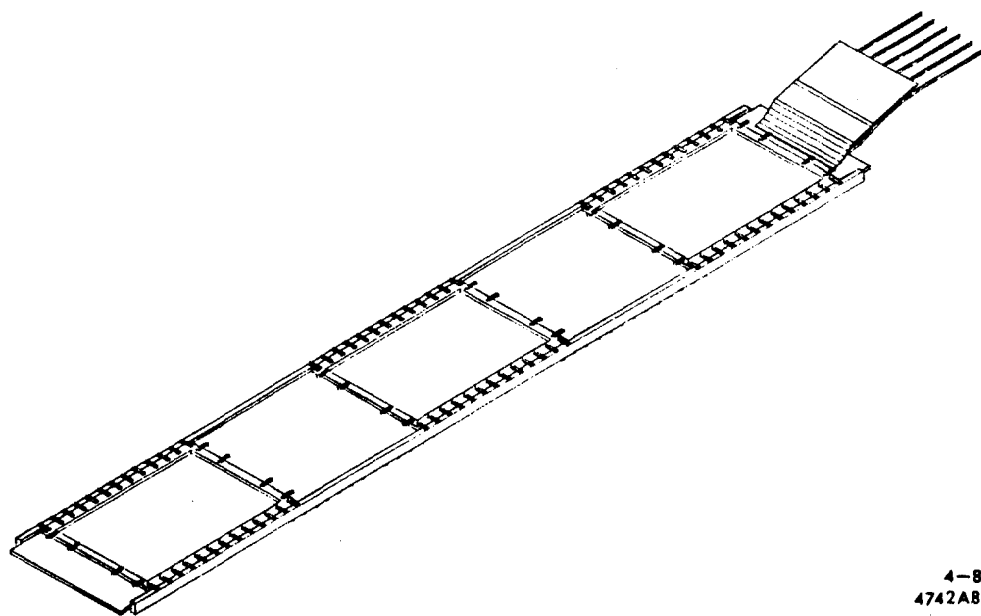
4-84
4742A82

Figure 5.2. Construction of one 'ladder' of *CCDs*.

68.4 MM

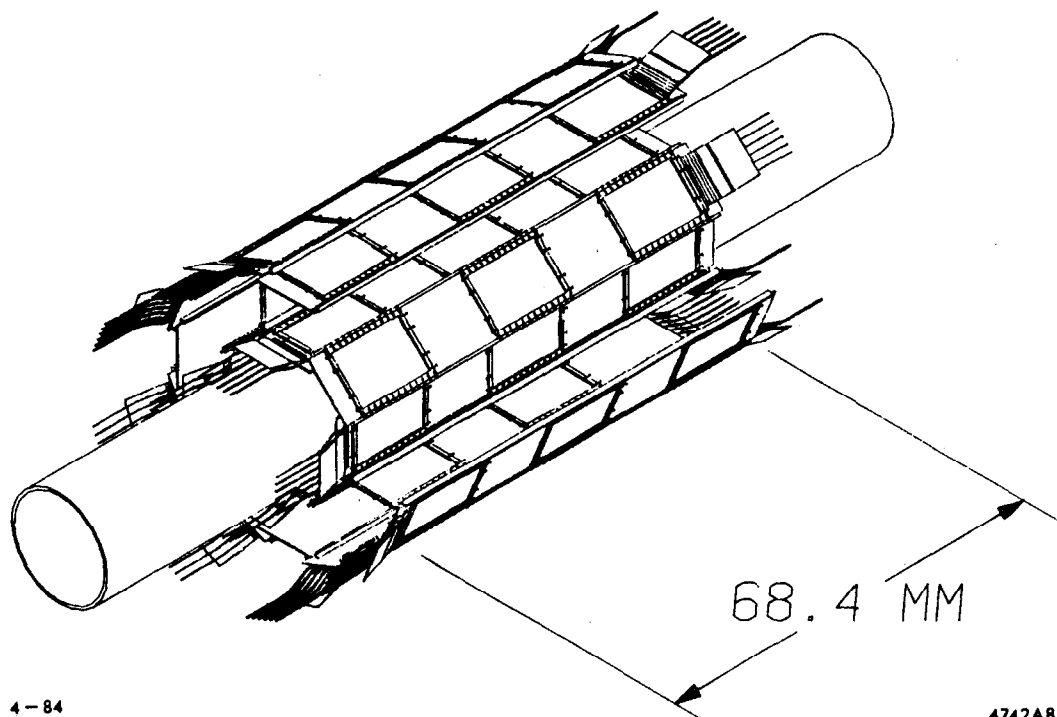Figure 5.3. Arrangement of ladders to make up the barrel detectors *B1* and *B2*.

FRONT
CCD's

BACK
CCD's

EXTERNAL
CONNECTIONS

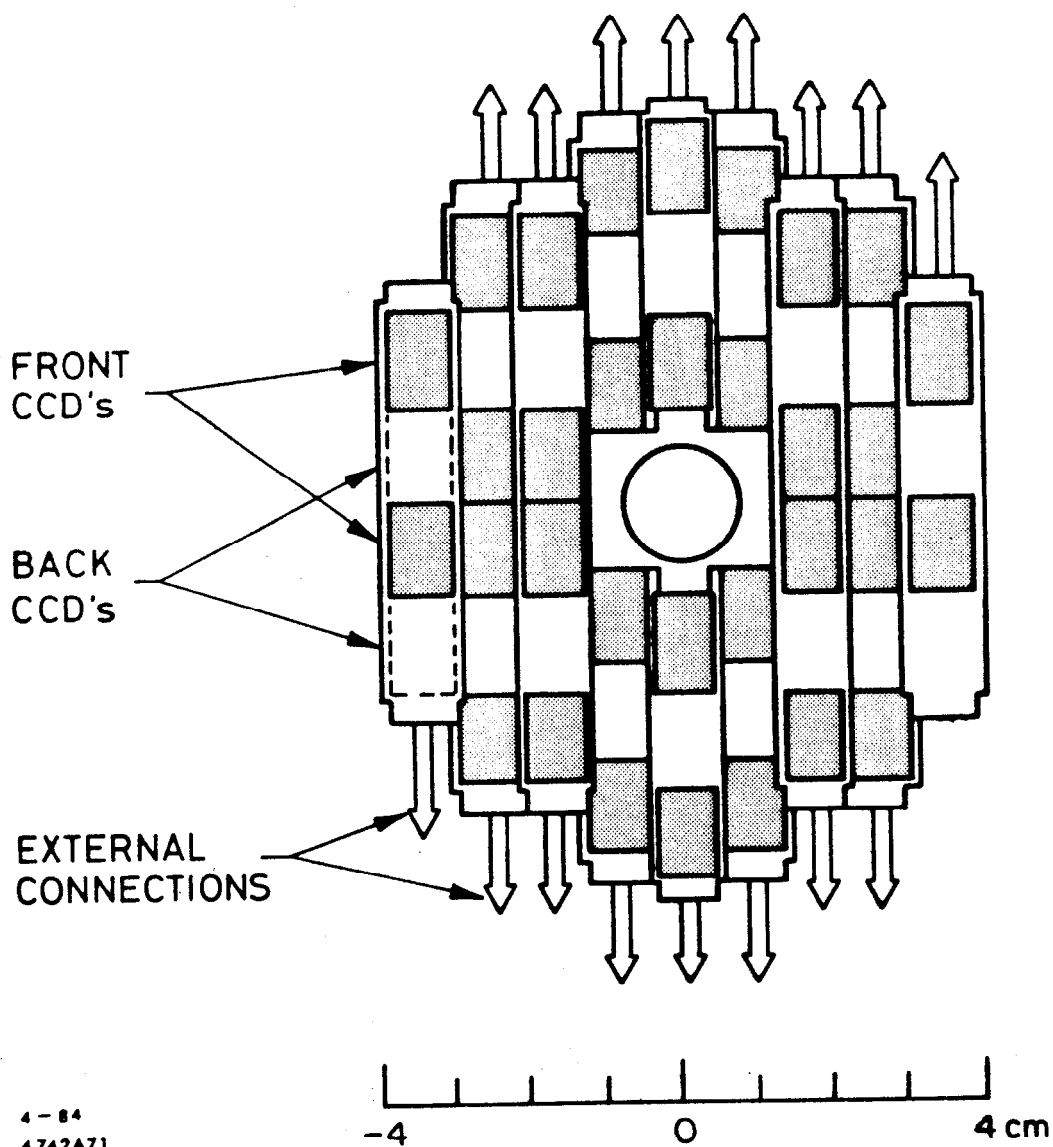4 — 84
4742A71

−4   0   4 cm

Figure 5.4.   Arrangement of ladders to make up the endcap detectors *EL* and *ER*.

be disabled and useful data taking could continue in the remaining ladders.

5.1.3 Electronics

Within 4 ms after a beam crossing, the trigger logic will have decided whether the event is to be fully read out. If not, the vertex detector is put into 'clear' mode. This means that the parallel and serial registers of the *CCD*s are triggered together approximately 578 times without any reading of the analog outputs. The effect is to dump the stored charges in all pixels through the reset transistor at the *CCD* output nodes. The devices are thus cleared for the next beam crossing. At the *SLC* the time between beam crossings is 5.5 ms, so the clearing time can be as long as 1.5 ms. This allows the drivers to be conveniently mounted outside the detector and the signals fed in on long transmission lines for each ladder. If a triggering event is detected, further crossings of the *SLC* are inhibited while the vertex detector is read out. This requires approximately 50 ms. The read out of each row now requires one shift of the serial register followed by a sampling of the analog level, followed by 385 repetitions of this process. A step in the analog output between two adjacent pixels represents charge stored in the second pixel. There are three requirements:

   (a)   all *CCD*s are read in parallel;

   (b)   the serial register is cycled as quickly as possible (100 ns);

   (c)   the analog signal is sampled as briefly as possible ($\approx$ 100 ns) consistent with the required noise level of $\ll$ 1 minimum ionizing particle.

Requirement (b) imposes obvious limits on the risetime of the serial register drive pulses. The required risetimes are much faster than for the parallel register, but the situation is eased by the much smaller capacitances of the serial register gates, so that again external drivers and low impedance transmission lines can be used. The signal processing is indicated schematically in Figure 5.5. The electronics beyond the preamplifiers is mounted in 6 Fastbus crates on the outside of the detector. The signals first pass through a linear gate which is closed when the *CCD*s are being clocked in order to protect the sensitive downstream electronics from relatively massive clock feed-through pulses. Without this, there is an inevitable recovery time of some hundreds of nanoseconds. To average and
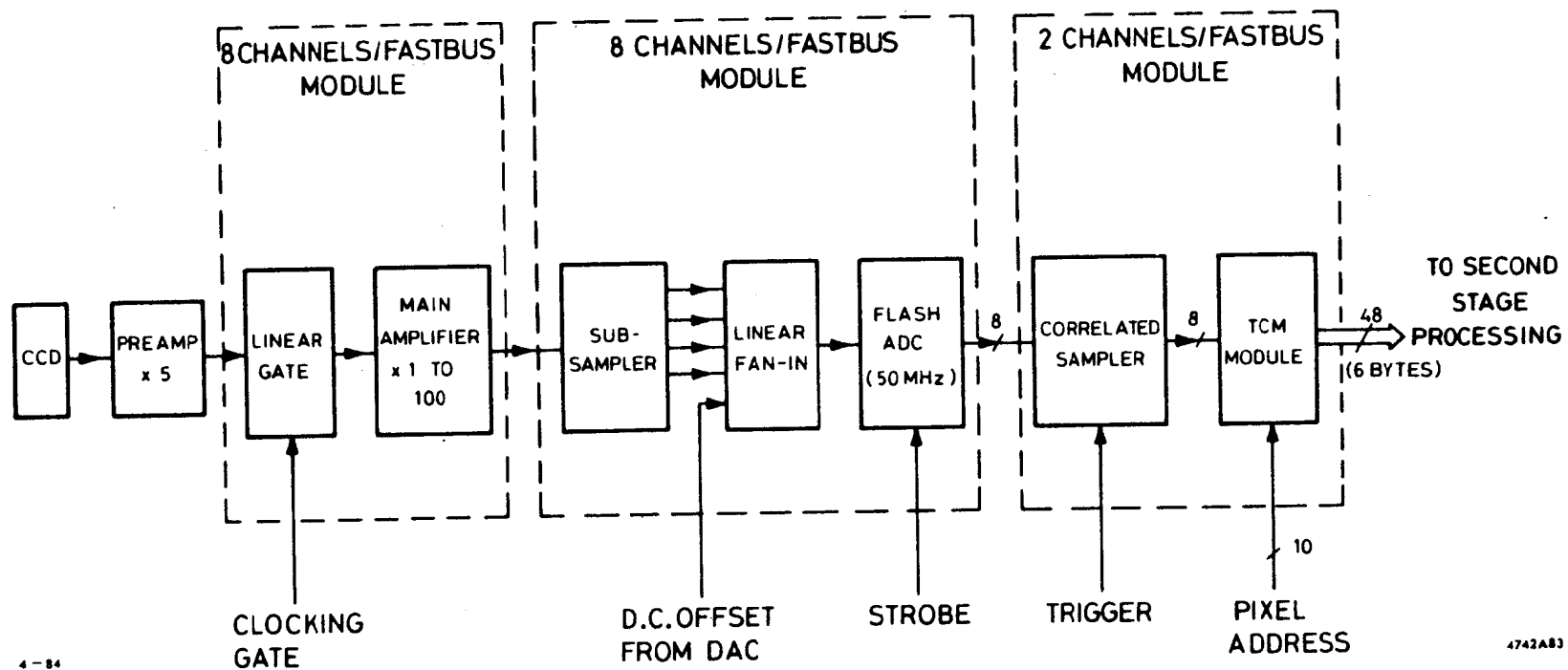
Figure 5.5. Block layout of *CCD* readout electronics.

process the signals, the main amplifier and sub-sampler split the signal into four with 5 ns relative delays between each. These signals are combined in the linear fan-in, together with a dc level which provides the control on the sample levels to be taken by the *ADC*. The flash *ADC* takes 4 samples at 20-ns intervals (effectively 16 samples at 5-ns intervals due to the effect of the sub-sampler). The correlated sampler sums the 4 samples corresponding to each pixel in turn and subtracts the result from the previous sum. It then feeds out the difference to the Thresholding, Clustering and Memory logic module (*TCM* module). This will be a pipelined processor working on several rows of data in a fast memory while the next few rows are being read into a second fast memory. This flexible module allows clusters to be defined, the cluster pulse height to be determined, and thresholds (lower and upper) to be imposed on the cluster or on individual pixels. When the pixels which are contained within accepted clusters are recognized, the pixel address (*CCD* number, parallel register number and serial register number) is associated with the pixel pulse height (6 bytes in total) and sent to the data acquisition memory.

5.1.4 Backgrounds

Two general sources of background have been considered, neutron and ionizing radiation. Neutron background from the beam dumps, and other nuclear backgrounds, constitute a steady source of nuclear interactions in the *CCD*s. Estimates show that these are entirely negligible, particularly since the P8600 *CCD*s are not highly sensitive to nuclear interactions, as are some other varieties of *CCD* design.

Ionizing radiation comes mainly from synchrotron radiation in the beams in the final bending magnets and quadrupoles. Direct synchrotron radiation is screened by a series of masks, but secondary scattering and x-ray fluorescence inevitably emerge at some level from the beam pipe. Nevertheless, the situation is much more favorable than at *LEP* where beams of large cross-section have to be tightly focused close to the interaction point, and where the equipment is subject to synchrotron radiation from a crossing rate 200 times higher than at the *SLC*.

The fluxes of synchrotron radiation are discussed in Chapter 8. The effect of this radiation on the detector involves two factors. First, the absorption coefficient of silicon over the relevant energy range of 10 keV to 1 MeV varies from 10 mm^{-1} to 10^{-2} mm^{-1}. At the upper end of the spectrum, the silicon is so transparent that very little of the radiation is absorbed by the entire material of the vertex detector. Second, x-rays below 100 keV normally give short range electrons by Compton scattering, which tend to give either no signal (conversion in the undepleted region of the detector) or to give signals many times that of a minimum ionizing particle if the electron is released in the depletion region. Such a background will be eliminated in the data acquisition system which will be set to exclude clusters of pulse height greater than a few times minimum-ionizing.

The result of these factors is that even the inner barrel detector sees a background of only about 10^4 Rads per year. While the radiation tolerance of the CCDs is still being evaluated, it is known that mega-hard, 3-phase CCDs can be fabricated, and there is no reason to doubt that CCDs can tolerate the radiation levels at the SLC. The background clusters which fake signals from minimum ionizing particles are calculated to occur at a level of only a few per square centimeter. Projecting tracks inward from the central drift chamber gives an area of confusion of from 0.03-0.07 cm^2 at each plane and angular resolutions of $\Delta\theta =$ 6 mrad and $\Delta\phi$ from 1 to 6 mrad all at the 2.5-σ level. Random hits in two planes can link up with drift chamber tracks only if they fall within these areas and angles. The probablility for random hits satisfying these constraints is small. The CCDs should be capable of handling a background level of many hits per square centimeter, well above the calculated values.

The synchrotron radiation background may not work out entirely as calculated. Indeed, experience in other colliders shows that the calculations are frequently too optimistic. Thus it may be necessary to enlarge the inner radius of the detectors. With this in mind, it is intended to continue the CCD production beyond the 220 CCDs initially needed. There may be an advantage to adding a third barrel or a second set of endcaps, and the cost of CCDs is sufficiently modest that one will prepare for expansion by building the required detectors.

5.1.5 Performance

The general performance of the *CCD* detectors when traversed by minimum-ionizing particles is as follows. Signals are seen in compact clusters of neighboring pixels, with typically 80% of the pulse height being contained in the two most populated pixels. Typical data are shown in a gray-scale representation of the pulse heights in Figure 5.6, which shows 17 tracks passing through an area of 1 square millimeter, including two which are separated by only about 50 μm in space. The two-track resolution is indicated in Figure 5.7. which also gives a good indication of the very uniform background on which these small signals are superposed; dark current variations between pixels, and electronic noise, are at a very low level. Occasionally a minimum-ionizing particle produces a cluster of large pulse height due to high-energy δ electrons or, very rarely, nuclear interactions in the silicon. In such cases, the cluster is always abnormally large, frequently showing a clear track-like quality, Figure 5.8. The corresponding cluster centroid would obviously produce a false track co-ordinate, but such clusters are excluded from the event reconstruction on the basis of pulse height and cluster shape. The δ electrons are thus a much smaller source of confusion than in drift chambers or microstrip detectors where the knowledge of the spatial distribution of the detected charge is rather limited. Fig 5.6 demonstrates clearly the advantage of a 2-dimensional detector in an environment of high track density (such as a jet from Z° decay). If the data of the figure are seen only in the x or y projection, there would be a serious level of track merging and the consequent problem of de-clustering with an inevitable loss of information and spatial precision.

5.2 THE CENTRAL DRIFT CHAMBER

5.2.1 Description

The central drift chamber (*CDC*) occupies the volume defined by an inner radius of 20 cm, an outer radius of 100 cm, and a length of 200 cm centered about the interaction point. The *CDC* is cylindrical in shape with an outer wall, flat end plates enclosing the volume, and an inner pipe or hole for the beams and vertex detector, as shown in Figure 5.9. Internally, the drift chamber con-
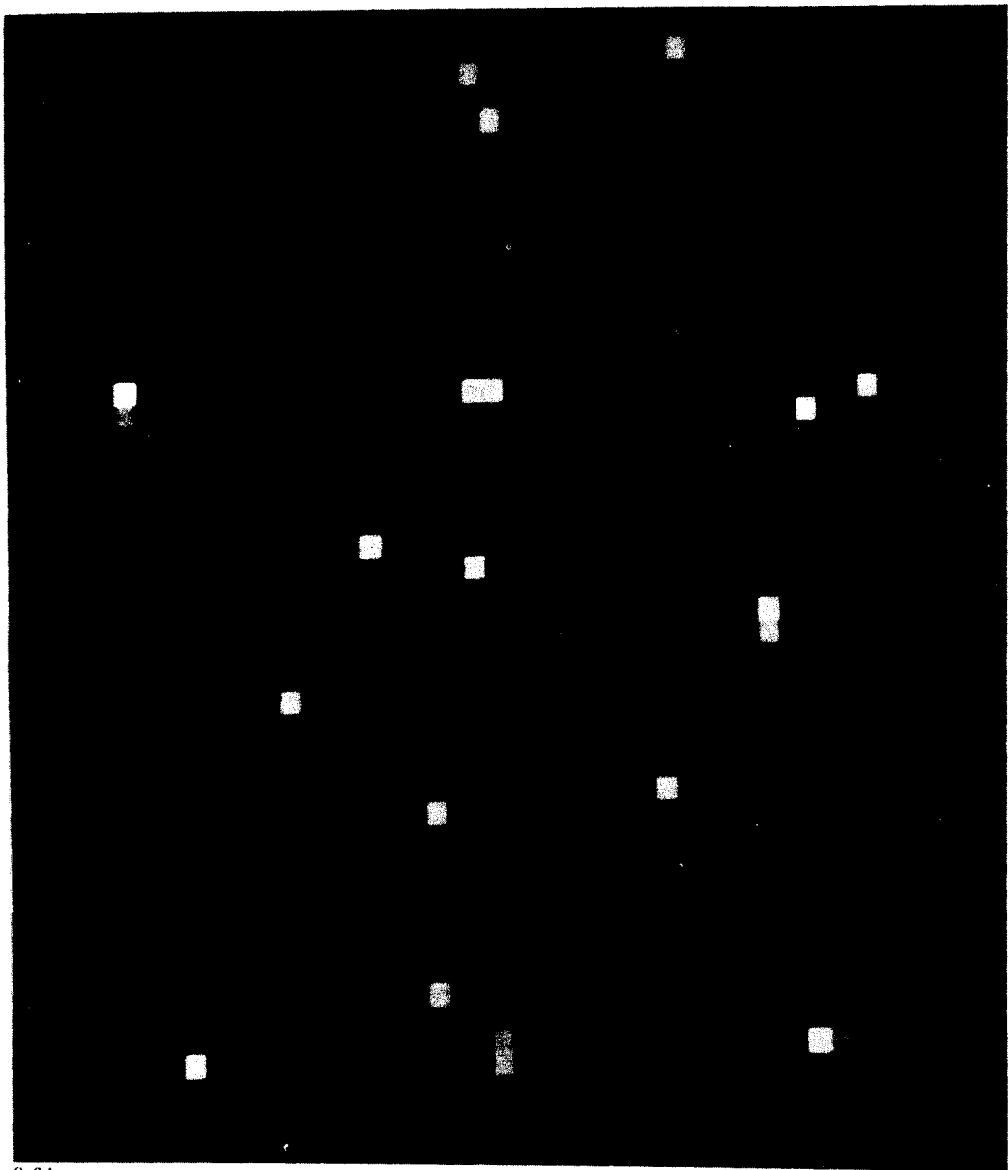
Figure 5.6. Gray scale representation of pulse heights in 1 square millimeter of pixels.
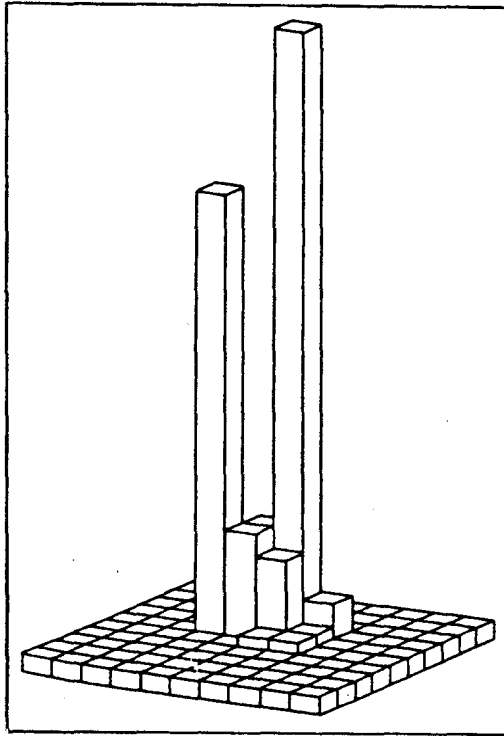
4—84   4742A67

Figure 5.7. Two track resolution of CCDs in an isometric reconstruction of two particles separated by 40 μm. The height of each element represents the pulse height measured in the corresponding pixel.

4—84   4742A66

Figure 5.8.   A heavily ionizing recoil track of length approximately 2 mm (probably the result of Coulomb scattering).
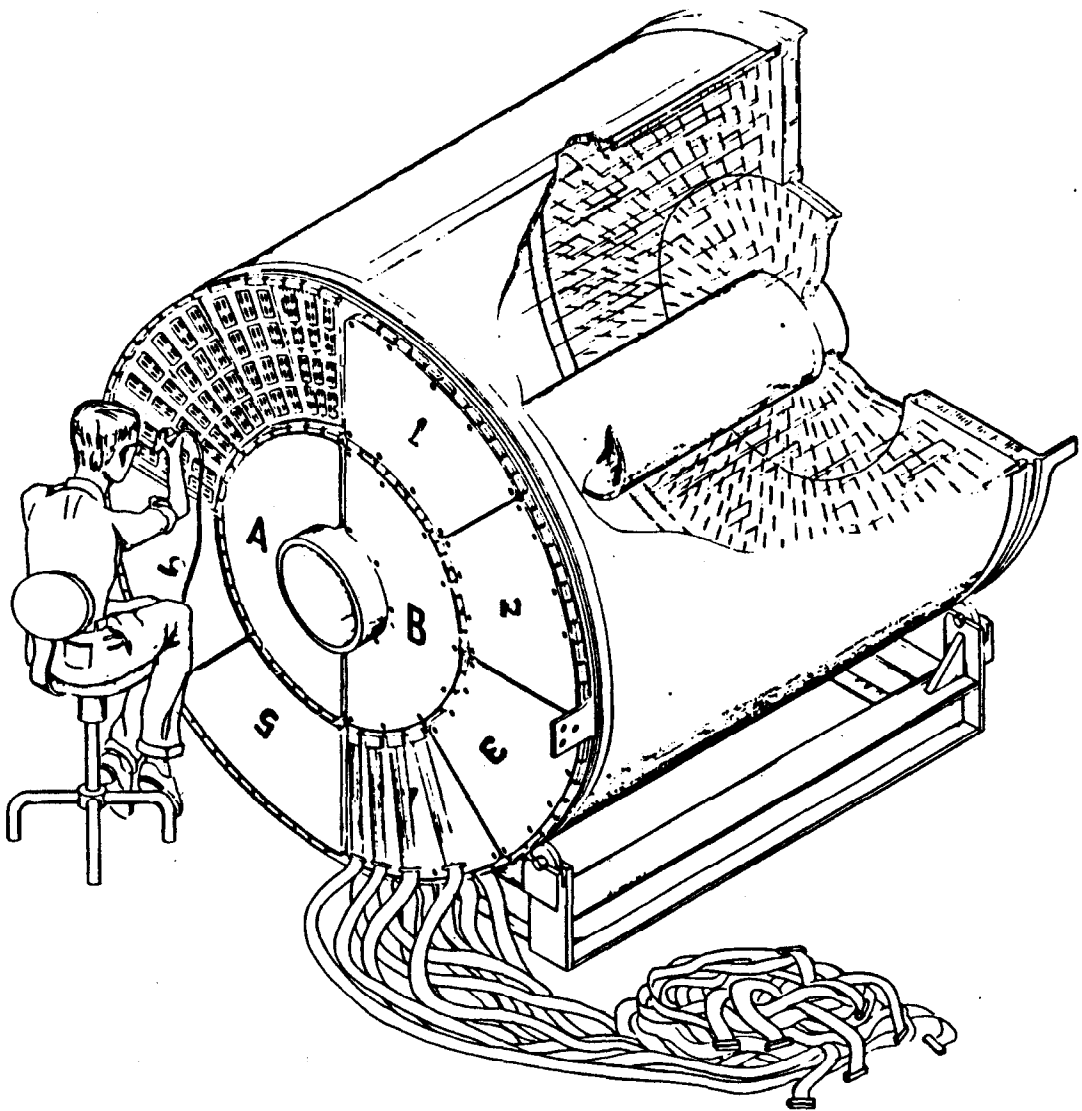
Figure 5.9. An illustration of the central drift chamber.

Table 5.2.
Parameters of the Central Drift Chamber

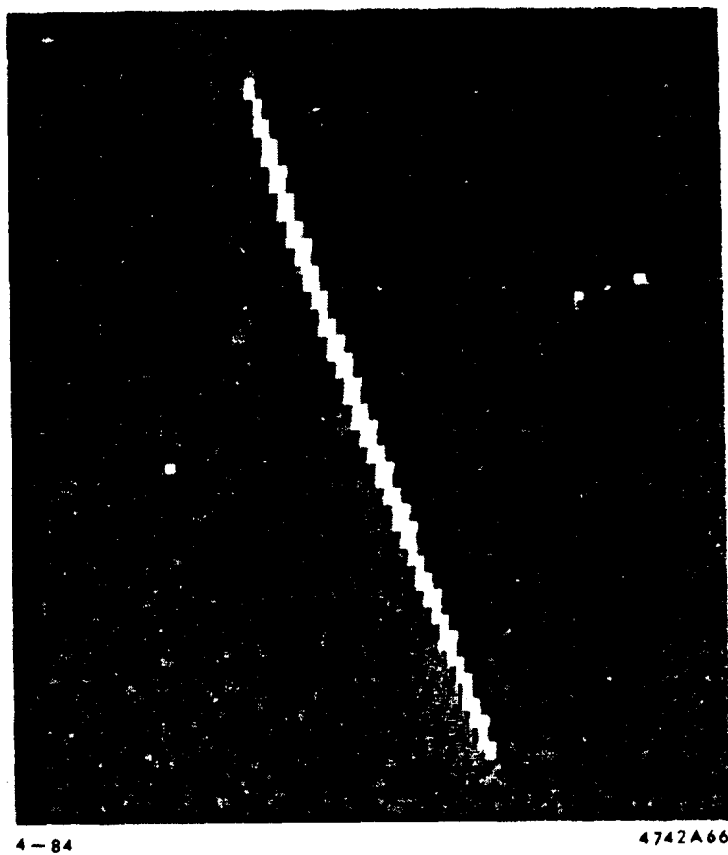|	
Inner radius	200 mm
Outer radius	1000 mm
Length	2000 mm
Innermost wire radius	238 mm
Outermost wire radius	961 mm
Number of superlayers	10
Number of sense wires per cell	8
Number of sense wire layers	80
Number of axial layers	32
Number of stereo layers	48
Number of vector cells	640
Stereo angle	50 mrad
Number of wires:	
Sense	5120
Guard	15360
Field	17280
Bulkhead load	16 tons
Cell dimensions:	
Height	49.8 mm
Full width	59 mm
Nearest wire spacing (guard-sense)	4.3 mm
Sense wire diameter (stainless steel)	30 μm
Field wire diameter (Cu-Be)	170 μm
Average drift field	1.3 kV/cm
Average field at field wires	12 kV/cm
Maximum field voltage	−7 kV
Gas	CO_2-isobutane (92%-8%)
Average drift velocity	10 μm/ns
Lorentz angle in 1 Tesla	5 degrees
Amount of material:	
Inner wall	0.009 X_0
Wires	0.020 X_0
Gas	0.006 X_0
Outer walls	0.018 X_0
End plates and electronics	0.20 X_0
Charge division (all sense wires)	±1.0% of length
Track pair resolution	2 mm
Performance parameters (CDC alone)	
Momentum $\sigma(p)/p$:	
at low momenta	0.55%
at high momenta	0.20p% (p in GeV/c)
Polar angle $\sigma(\theta)$:	
at low momenta	2 mrad
at high momenta	1.6 mrad
Azimuthal angle $\sigma(\phi)$:	
at low momenta	1.1 mrad
at high momenta	0.34 mrad
Impact parameter error ($r\phi$ plane):	
at low momenta	200 μm
at high momenta	100 μm
Longitudinal Coord. $\sigma(z_0)$:	
at low momenta	1.0 mm
at high momenta	1.0 mm

sists of a large set of wires running approximately parallel to the axis, and held under tension by two bulkheads and the inner and outer walls. The chamber wires are arranged in ten superlayers, each with cells having eight sense wires. The orientation alternates between axial and stereo in the arrangement *AUVAU-VAUVA*. The wires establish electrostatic fields which direct the electrons from ionizing tracks to drift onto sense wires where they undergo amplification by gas avalanche mechanisms. Preamplifiers sense the resulting signals and provide additional gain for signals, which are transmitted on twisted-pair cables to external electronics. The mechanical design is described in Section 5.2.2 and the details of the electrostatic fields and the electron drift are described in Section 5.2.3. Both ends of each sense wire are instrumented with electronics, and comparison of relative signals at the two ends gives information on the z-position of a sense wire pulse through charge division. The importance of charge division in pattern recognition is discussed in Section 5.2.4. To optimize the measurement of the polar angle θ, stereo angles ($\pm$ 50 mrad) are introduced on some of the layers. The choice of stereo angle and the best mixture of stereo and non-stereo sense wires is also discussed in Sections 5.2.4 and 5.5. The parameters of the central drift chamber are listed in Table 5.2.

5.2.2 Mechanical Design

Figure 5.9 shows the overall structure of the *CDC*. The structure consists of two flat end plates supported by inner and outer cylindrical walls. The internal wires are strung to a tension of approximately 400 gm for field and guard wires and 50 gm for sense wires, for a total force on the each end plate of 16 tons, inwardly directed. The support walls consist of thin-walled honeycomb and are sufficiently strong to support the total force. The honeycomb walls consist of two 5 mil (0.13 mm) thick aluminum sheets with a nylon fiber honeycomb material (*NOMEX*) sandwiched in between. The outer walls and the inner tube are fabricated on mandrels of the correct size by a layup of the materials with bonding agents between the aluminum and honeycomb. The materials are set into the shape of the forms under pressure and heat. The endplates are fabricated in a similar fashion, but for these structural pieces, the materials are 1/4 inch (6.4
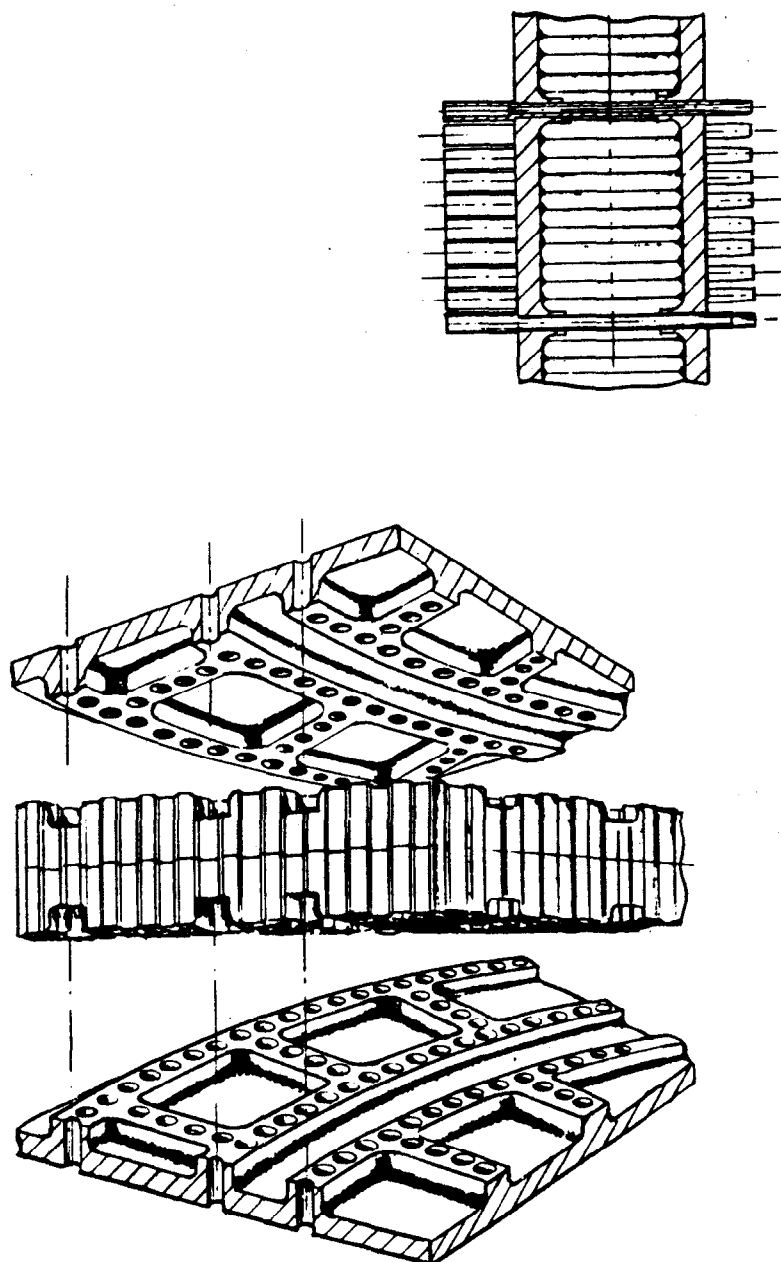
Figure 5.10. Details of the endplate honeycomb panels.

mm) thick aluminum and aluminum honeycomb core. The end pieces are 2-inch (51 mm) thick, chosen to provide sufficient stiffness. Figure 5.10 shows some detail of the endplate design. The aluminum is ribbed to provide additional stiffness where wire feedthrough holes penetrate the sheets. The honeycomb must be milled out in the reverse pattern for close fit. Layup and bonding of the endplates will be done in a hot press.

Feedthrough holes will be drilled on a numerically controlled (*NC*) machine. The accuracy of wire location in this scheme using molded feedthroughs and wire guide inserts to center the wires is shown in Figure 5.11. These were measured in an *SLD* prototype chamber. The projected rms scatter of 26 μm is better than needed for the *CDC* specifications. Figure 5.12. shows the basic structure before final assembly.

The *CDC* consists of an inner spool piece and an outer structure. Each portion of the *CDC* is separately able to support the forces of wires. The advantages of a two-piece *CDC* are several. First, access to the interior of the chamber is best in this scheme. Second, fabrication of the two separate pieces can occur in parallel, shortening the construction time. Third, the structural members are built before stringing, providing stiff and strong pieces during stringing of wires. Accurate end-to-end alignment is better in this scheme because of the torsional stiffness of the pieces. Perhaps the most important advantage of the 2-piece chamber construction for the *SLD* is the ability to make a structure with walls of minimum radiation thickness without the complexity and material involved in sealed removable side panels. A minor disadvantage lies in the alignment of the inner piece relative to the outer piece. This alignment can be done well mechanically, but ultimately will be tuned accurately in software, using tracks. A system (in the *DELCO* experiment) similar to this proposed design achieved 10 μm errors in transverse positional accuracy and 0.3 mrad in angle.

The chamber construction will proceed as follows: the endplates are prestressed, using rods and springs, before stringing the wires one by one through their plastic feedthroughs. Stainless steel wire guides will be threaded by hand, the wires pulled to nominal tension, and the wire guides crimped. Springs located
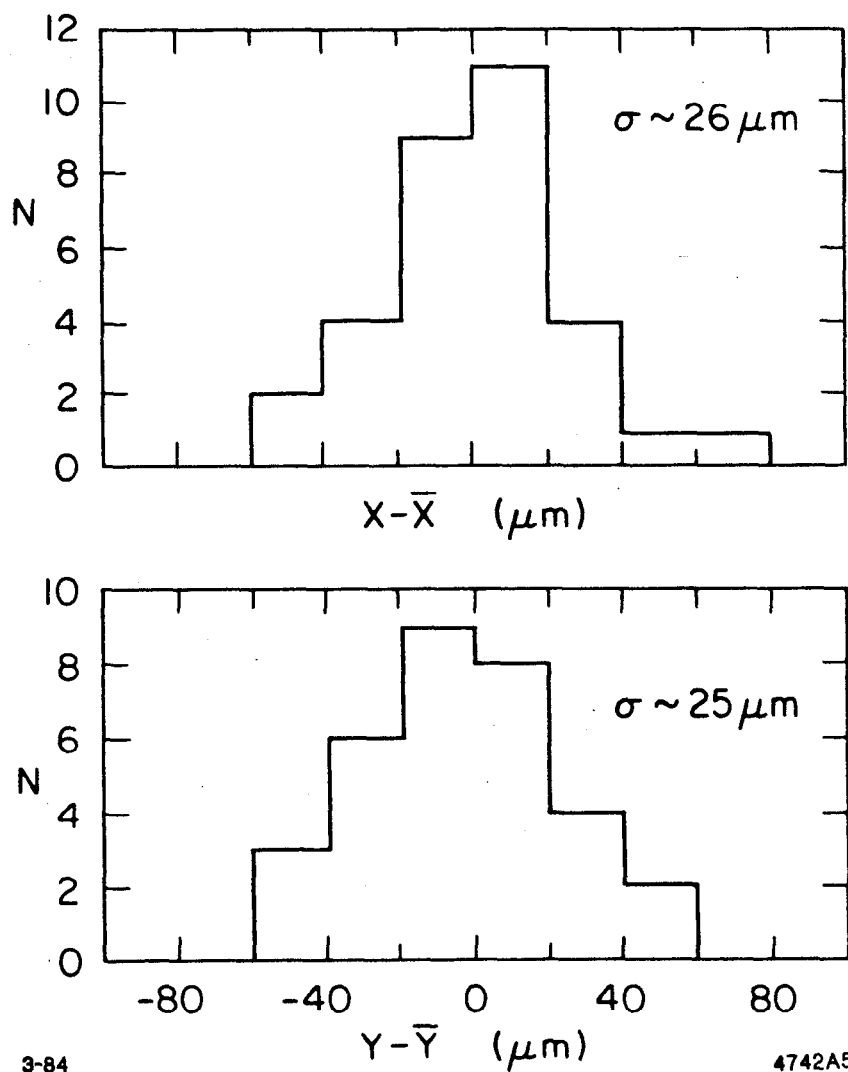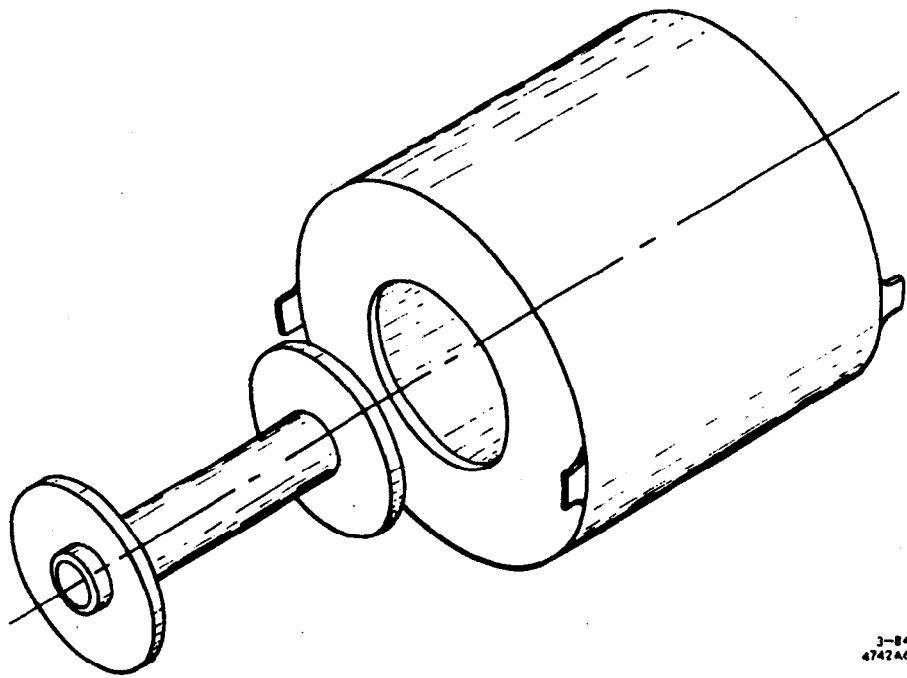
Figure 5.11. Scatter of 32 sense wires about the nominal values in a *SLD* proto-type chamber. The rms deviations are well within tolerances needed to preserve overall track resolution.

3-84
474246

Figure 5.12. Inner and outer structures of the central drift chamber. Access to inner volume for assembly and, if needed, repair is provided in this scheme.

at one end of each wire hold the tension during construction, even though the endplates may flex minute amounts as the stringing proceeds. The pre-stressing rods are removed one at a time as wire stringing progresses. After stringing is complete, the ends of the feedthroughs are sealed with epoxy to prevent gas leaks.

High voltage distribution is applied next using multi-layered printed circuits. The total number of voltages required is approximately 200. The maximum voltage is approximately -7 kV. The next layer above the voltage distribution is for preamplifier circuits. The 640 eight-channel hybrid preamplifiers are distributed about the ends. Output signals are sent to the outer rim of the structures. Twisted pair cables pick up these signals and carry them to the outside of the detector. The details are illustrated in Figure 5.13.

5.2.3 The Cell Design

The electrostatics of the cell have been studied in some detail in computer simulation. Presently a prototype study is in progress. The basic cell is shown in Figure 5.14. It consists of 8 sense wires, 24 guard wires, and 27 field wires. The sense wires are separated by 5 mm; the guard wires are separated by 5 mm and staggered left and right of the sense wires by 3.5 mm. The field wires are separated by 5 mm and form a cage by closing the ends of the cell.

The choice of this cell design is primarily dictated by the requirement that a single track be measured by each sense wire to better than 100 μm. This point resolution permits an overall detector momentum resolution of $\Delta p/p =$ .001 p (p in GeV/c) in the high momentum limit. Each cell is 49.8 mm along the radius and approximately 59 mm wide at the midpoint. A plane of eight sense wires is surrounded by guard wires and field wires. Twenty two guard wires are arranged in two rows parallel to the sense wires. There are two additional guard wires (actually dummy sense wires) at the top and bottom of the cell to help shape the electrostatic fields of the cell. Field wires surrounding the cell complete the electrostatic field shaping. The smallest distance between wires is 4.3 mm between guard wires and adjacent sense wires. Voltages on the guard wires are expected to be approximately -2.80 kV, while field wires may run up
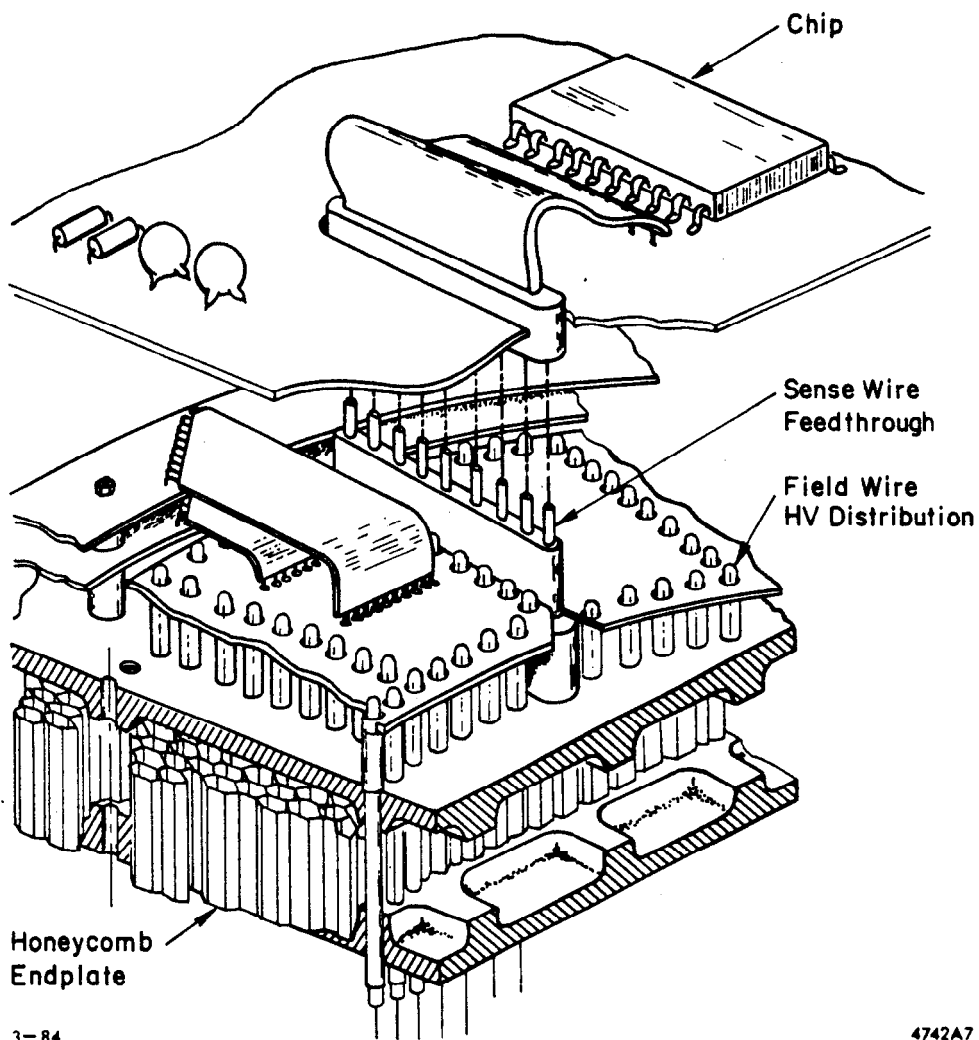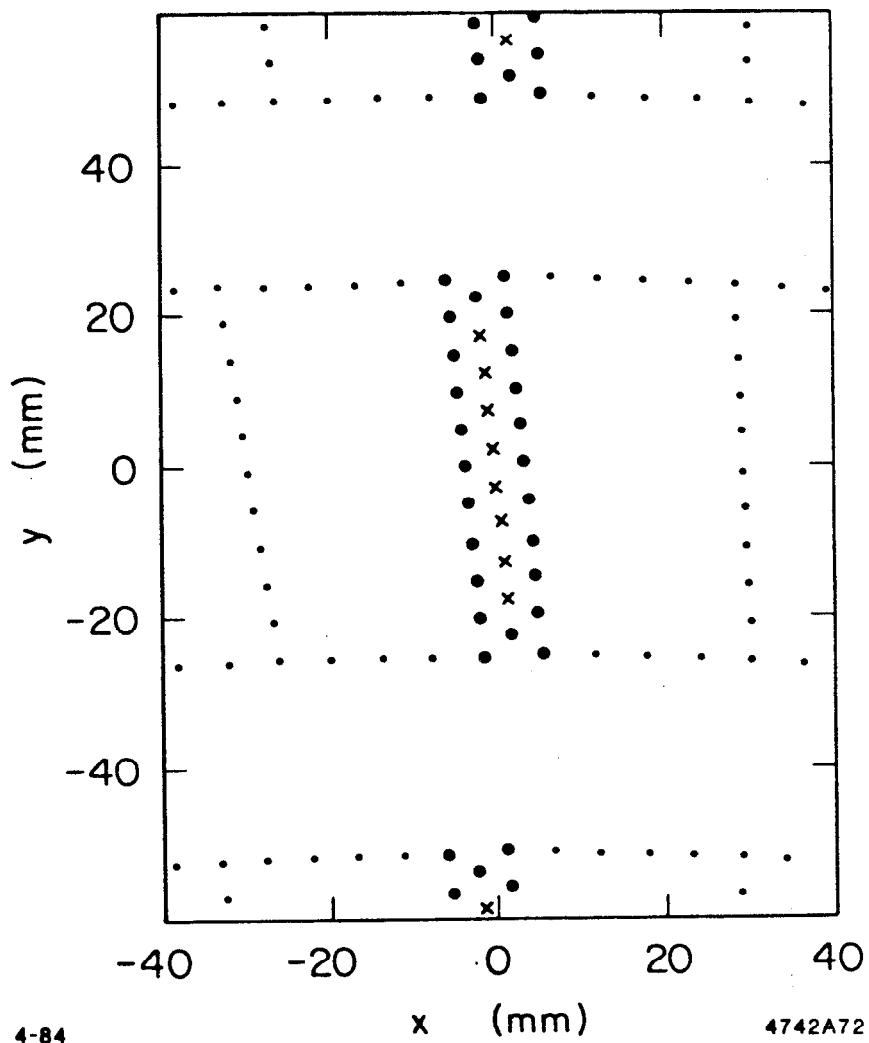
Figure 5.13. Detail of the high voltage distribution.

Chip

Sense Wire
Feedthrough

Field Wire
HV Distribution

Honeycomb
Endplate

3—84

4742A7

5 - 25

Figure 5.14. The basic cell design. Sense wires are shown as ✕, guard and field wires as ●.

to −7 kV.

The sense wire, guard wire, and outside field wire planes are tilted 5° away from radially pointing vectors, to take advantage of the Lorentz angle effects for drifting electrons in a 1 Tesla magnetic field. The advantages of a tilted cell geometry are described later. Potential contours for this cell are shown in Figure 5.15. Using computer simulation, the details of the drift chamber have been studied. The choice of the guard wire configuration focuses the drift paths of electrons coming from ionizing particle trajectories. Figure 5.16 shows a detail of one sense wire region. Charge collection on each sense wire is more nearly isochronous in this scheme than in others such as a single guard wire between sense wires. Figure 5.17 shows drift paths in the entire cell. The paths are approximately perpendicular to the radius vector, even though the cell has a tilt.

Figure 5.18 shows the longitudinal diffusion coefficients measured for several common gas mixtures. This parameter is the position uncertainty in the direction of the drift that an ideally localized distribution of electrons acquires after a drift of one centimeter. It depends on the values of E and P in the drift region and, of course, on the gas mixture. The three curves show (1) A-CO_2 - CH_4 (89%-9%-1%), (2) A - CO_2 - C_2H_6 (50%-25%-25%), and (3) CO_2 - isobutane (92%-8%). The best gas from the standpoint of diffusion is CO_2 -isobutane. This gas is currently being tested in an *SLD* prototype chamber. Using the measured gas parameters for CO_2 -isobutane, the performance of the cell has been predicted by computer simulation. Figure 5.19 shows the position resolution, for a single sense wire, versus the distance of the track from that wire. The lower curve is the contribution from gas diffusion, ionization fluctuations, and cell electrostatics. The upper curve shows an additional mechanical alignment uncertainty of 50 μm added in quadrature. One data point shows results of a CO_2 -isobutane prototype tested at *CERN*.[2] The *SLD* design is expected to achieve the 100 μm resolution specification.

The velocity of drift in CO_2 -isobutane is compared to the other two gases in Figure 5.20. It is approximately 5 times slower than that of standard argon mixtures. At the planned voltages, the velocity is approximately 10 μm/ns.
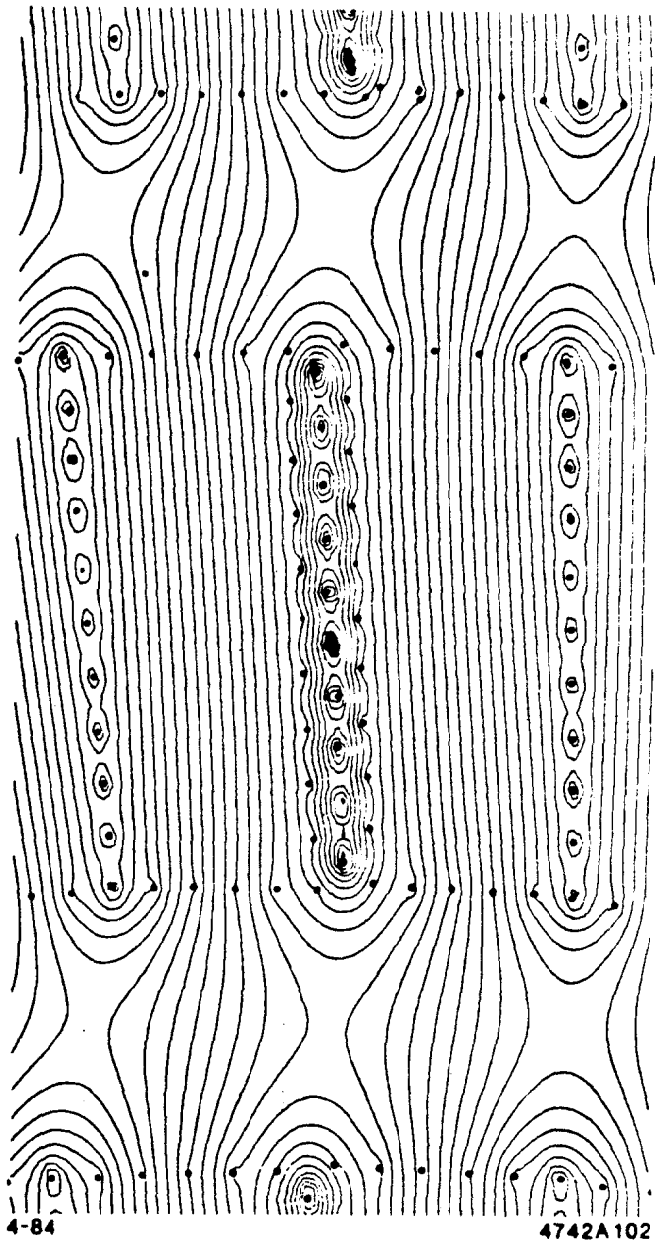
Figure 5.15. Equipotential contours in a cell.
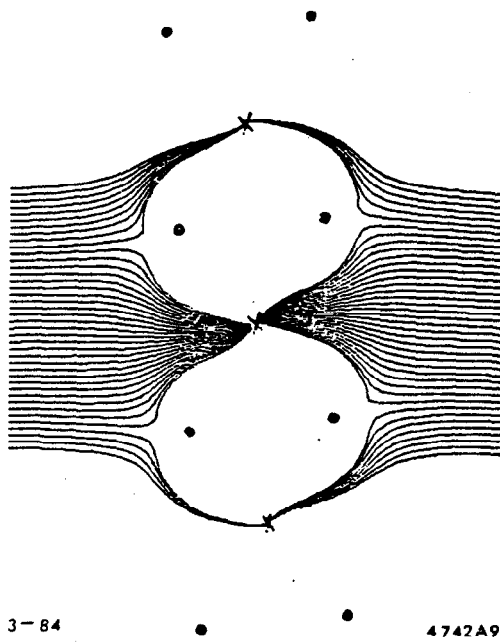
3 — 84   4742A9

Figure 5.16.   Electron drift paths near the sense wire for a track 10 mm from the sense wire.
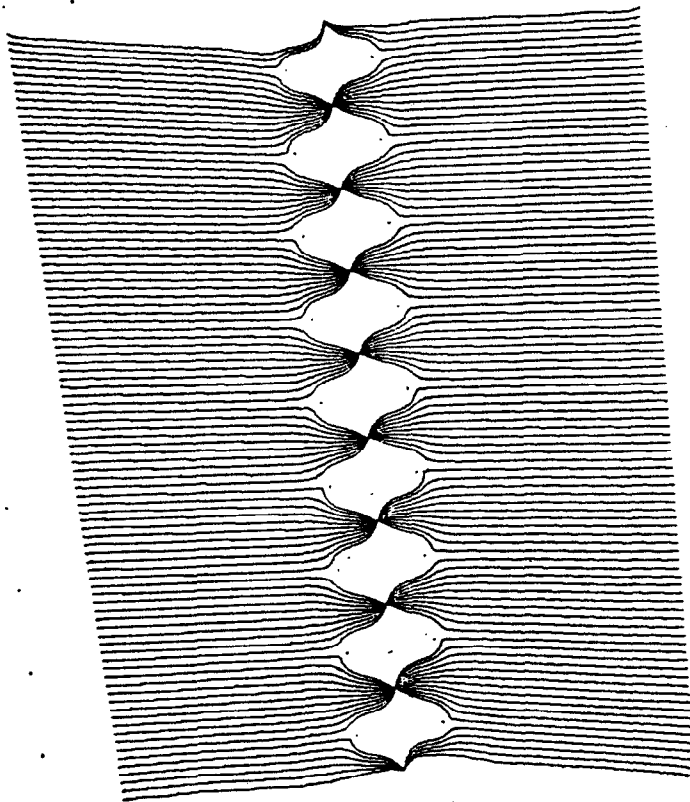
3 — 84

4742A10

Figure 5.17. Electron drift paths in the entire cell for a track 25 mm from the sense wires.

5 - 30
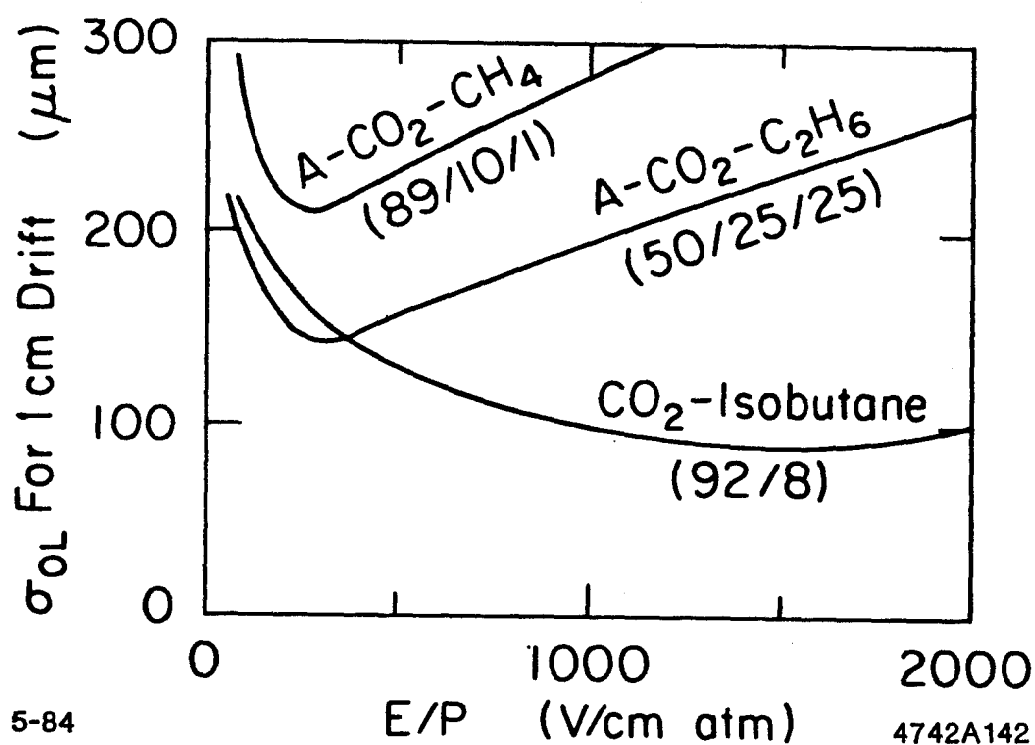
Figure 5.18. Longitudinal diffusion coefficients for three gases studied, versus drift field E.
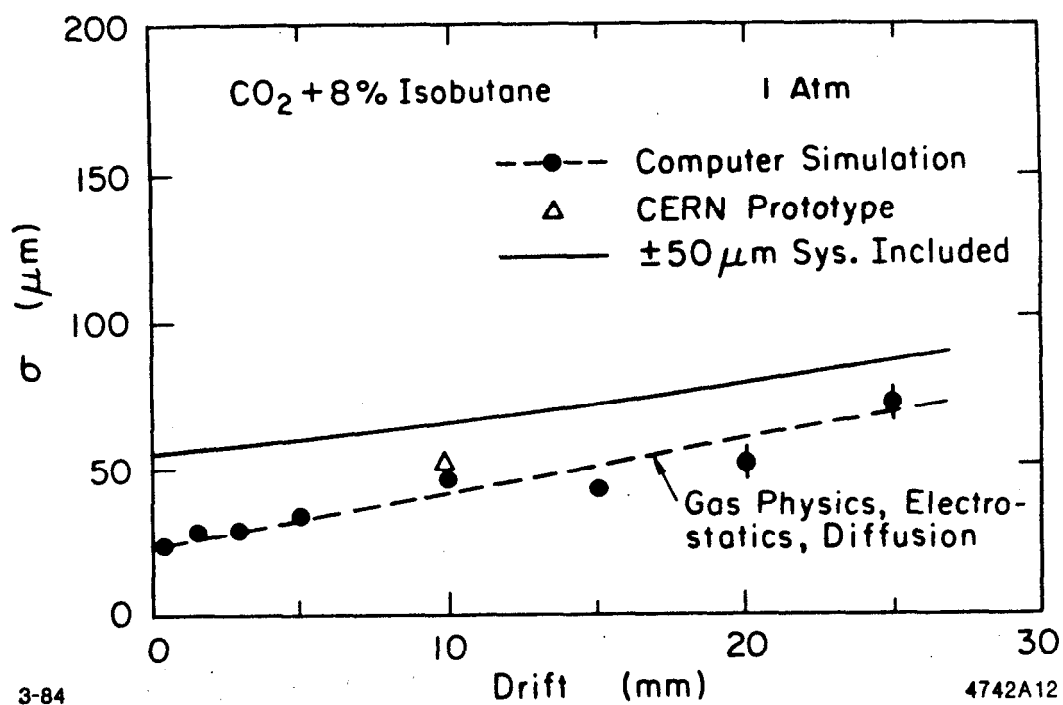
Figure 5.19. Track resolution versus drift distance predicted by computer simulation. One data point comes from a *CERN* prototype (*CERN-EP/83-81*). The dashed line smoothes the computer results. The solid line includes 50 μm systematic errors added in quadrature.
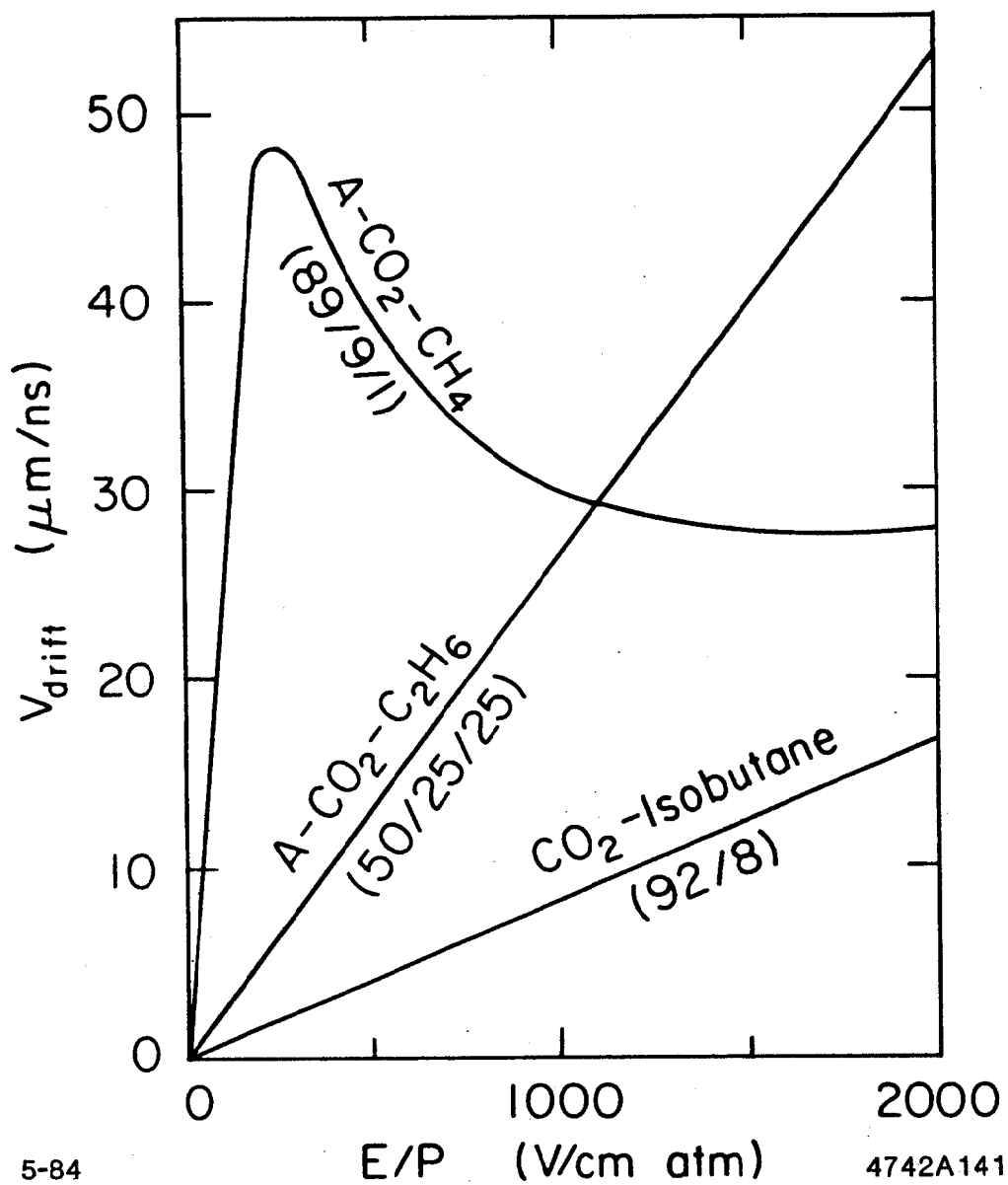
Figure 5.20. Drift velocities versus E for three gases at 1 atm.

This velocity is proportional to the field strength in the drift region. Changes in voltage or gas pressure can change the velocity, seriously degrading position resolution. Regulation of voltages and pressures to $\pm 0.1\%$ is planned. These residual changes correspond to an average $\pm$ 15 μm uncertainty in position. Temperature regulation to $\pm 1°C$ will maintain overall alignment of the wires in the CDC. Monitoring of the drift velocity will be incorporated into the system.

The choice of a tilted cell design is preferred by tracking efficiency considerations. Figure 5.21 shows the principle of the problem encountered in non-tilted cells in magnetic fields. The negatively-charged track in that figure passes through five or six collection regions of the cell, while the positively-charged track passes through only two or three. Inaccesible regions in non-tilted cells lead to a ϕ-dependent tracking efficiency. In CO_2-isobutane, the (small) 5° Lorentz angle minimizes this problem, but tilting the cell is still preferable over a non-tilted cell design. One benefit of using an unsaturated gas is that the Lorentz angle is approximately independent of electric field.

Tracks which pass through the collection regions at angles that are not normal to electron drift lines will suffer degradation of resolution due to ionization fluctuations having components along drift lines. Figure 5.22 shows an estimate of this degradation by the formula

$$\sigma_m^2 = \sigma_0^2 + \left(\frac{1}{2\bar{n}} \sin \theta_N \right)^2$$

where σ_0 is the measurement resolution, θ_N is the angle of incidence on the collection region, and $\bar{n}$ is the specific ionization.

The two track resolving power in CO_2-isobutane seems to be somewhat better than for argon mixtures, approximately 2 mm versus 3 mm respectively. A track passing through a cell leaves a 2-mm dead band on both sides of the sense wire. Figure 5.23 illustrates the dead regions where additional tracks will be lost. The dead band on the side of the cell away from the track is a reflection of the real dead band. In a tilted cell design these reflected dead bands do not point toward the origin, but are tilted themselves by twice the cell tilt angle. The

5 - 34

Super
Loyer

4742A17
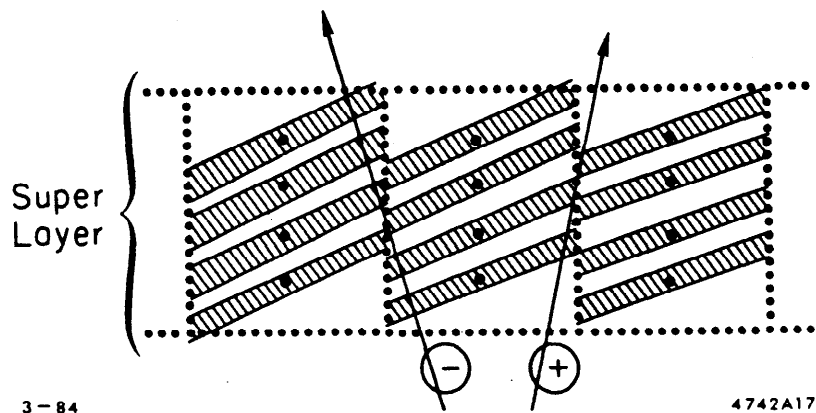
Figure 5.21. An idealized sketch of a non-tilted cell. The dead triangular regions
cause tracking inefficiencies that depend on angle.

200

Resolution vs Penetration Angle   A-CO_2-CH_4

σ_m (μm)

100

CO_2-Isobutane

Lorentz Angle For:
CO_2-Isob   A-CO_2-CH_4

0

0   10   20   30   40

θ_N (degrees)

3 - 84   4742A16

Figure 5.22. An estimation of resolution degradation due to tracks with angles not normal to collection regions in the cells.

5 - 36

Figure 5.23. Dead bands in a non-tilted cell can aggravate the cell inefficiencies.
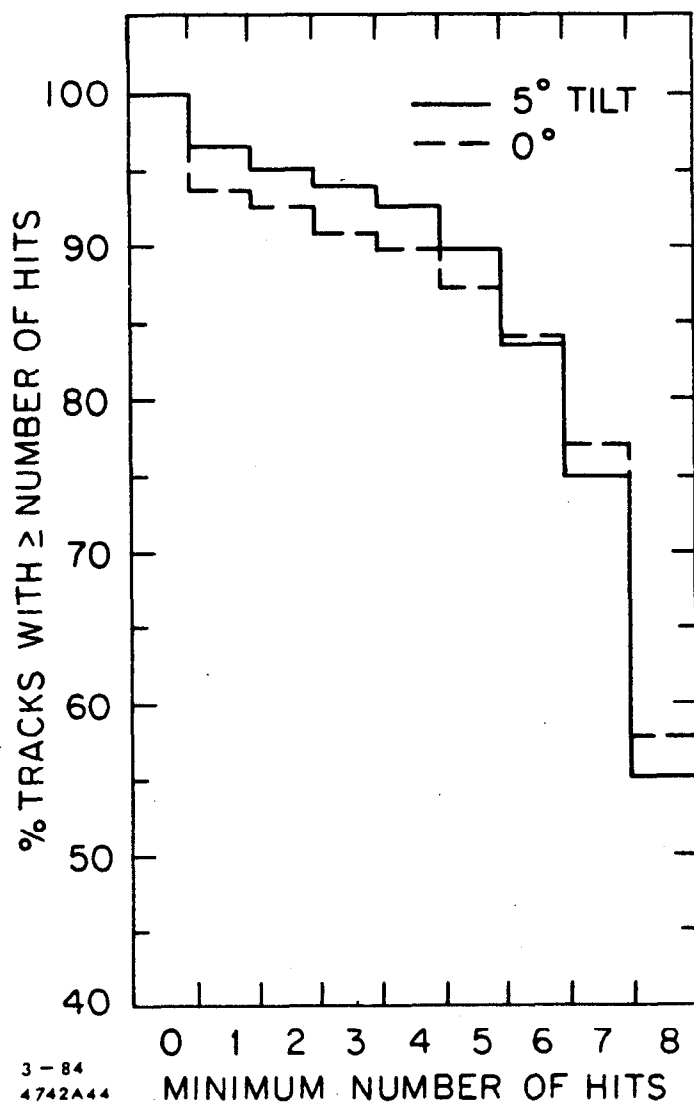
Figure 5.24. Comparison of the available number of hits per track in 0° and 5° tilted cells in the innermost superlayer, using Lund Monte Carlo events.

probability for this reflected dead band to kill an entire track segment in the cell is small, so hit inefficiencies are expected to be smaller t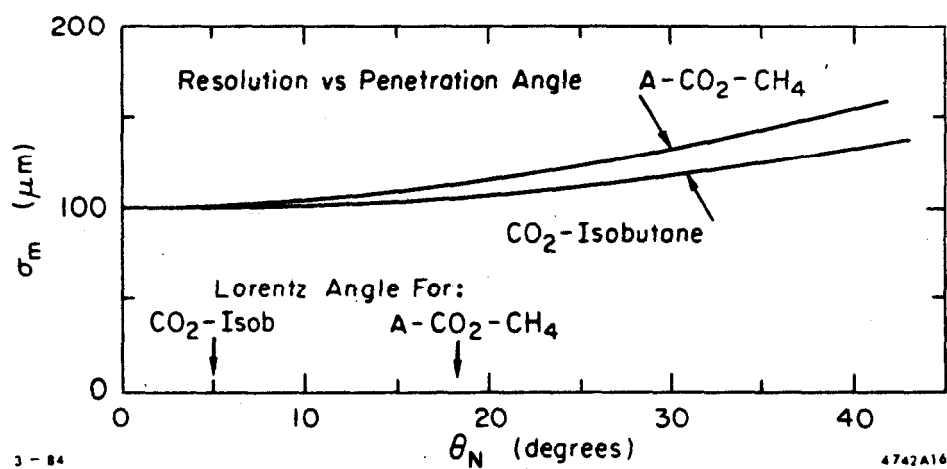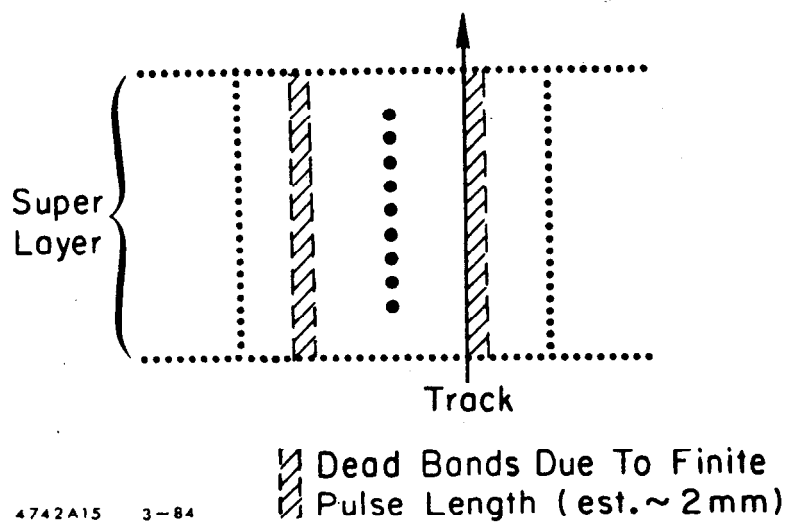han those of a similar non-tilted cell. Figure 5.24 shows hit efficiencies in the innermost superlayer of the *SLD* design for 0° and for 5° tilt. Track segments are characterized by the number of hits which survive (0 through 8) by not lying in a dead band. This calculation used the Lund Monte Carlo generator for Z° decays, which should approximately represent the jet-like nature of event topologies to be expected. Figure 5.24 shows a decreasing efficiency as the number of hits required increases from 0 to 8. Minimum standalone tracks segments that could be useful would require 3 or more hits. The tilted cell design shows greater efficiency for 3, 4, or 5 hits required, and lower efficiency when 7 or 8 hits are required. This lower efficiency for 7 or 8 hits can be easily understood since the reflected dead band tilts at twice the cell angle and thus is more likely to kill some parts of additional tracks. This is not a serious problem. Tracking algorithms are expected to push down to 3 hits in track segment definitions, where the tilted design is better. The conclusion of this calculation is that tilted cell designs perform better.

A disadvantage of the tilted cell design is that performance is degraded if the magnetic field is reversed, so a strong bias against that possibility is inherent to the detector.

Using the tilted cell design, a section of the drift chamber is as shown in Figure 5.25. Ten superlayers are arranged in four axial and six stereo layers. Charge division on all sense wires provides z-position values. The charge division information allows stereo layers to participate in the track finding algorithms by projecting these points back to the $z = 0$ plane. This is discussed in detail in Section 5.5.3. Table 5.3 lists the configuration of the superlayers.

5.2.4 Charge Division and Stereo

At the Z° the mean charged particle multiplicity is expected to be approximately 21, which will make these events the most difficult to reconstruct of any $e^{+}e^{-}$ storage ring experiment to date. The *CDC* has four axial superlayers comprising 32 sense wires. These are the innermost, outermost and two central superlayers — an arrangement that optimizes the momentum resolution of the
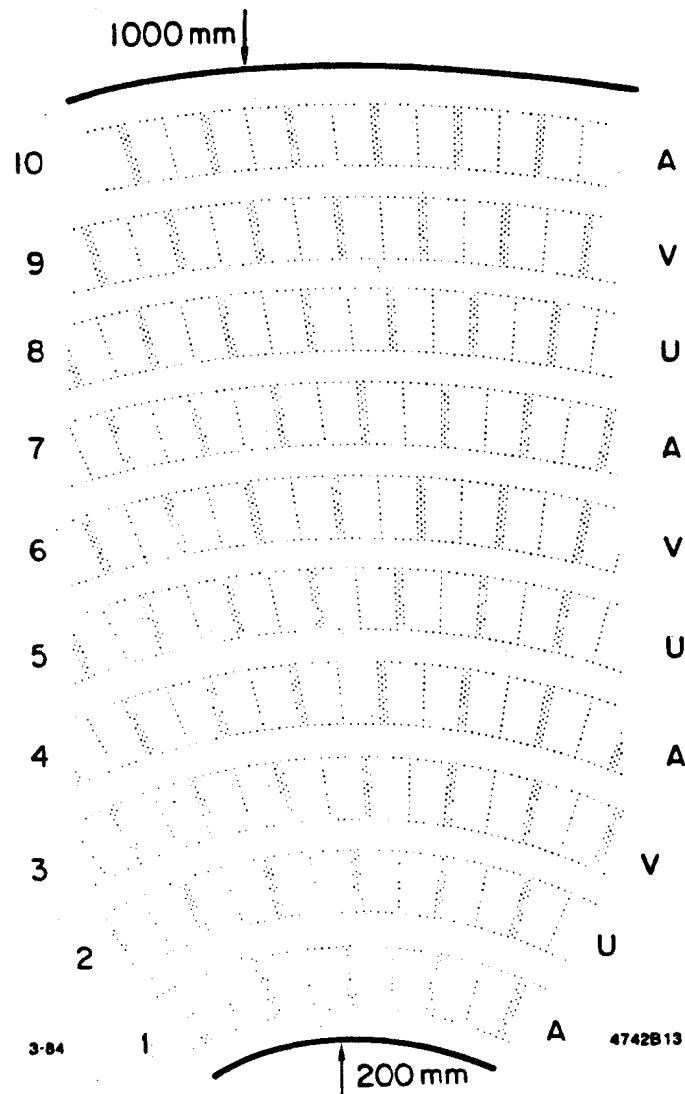
Figure 5.25. A section of the central drift chamber, showing wire patterns. The notation *A*, *U*, and *V* refer to axial and two stereo angles 0 and ± 50 mrad, respectively.

5 - 40

Table 5.3.
Geometry of the Central Drift Chamber

Element	ΔR mm	R_i mm	R_c mm	R_o mm	N	Cell Width mm
Inner Wall	10.00	200.00	205.00	210.00		
gap	26.90	210.00	223.45	236.90		
SuperLayer1 (A)	49.81	236.90	261.80	286.71	28	58.75
gap	24.62	286.71	299.03	311.33		
ax-st gap	3.27	311.33	312.98	314.60		
SuperLayer2 (U)	49.81	314.60	339.50	364.41	36	59.25
gap	24.19	364.41	376.51	388.60		
SuperLayer3 (V)	49.81	388.60	413.50	438.41	44	59.05
gap	24.19	438.41	450.51	462.60		
SuperLayer4 (A)	49.81	462.60	487.50	512.41	52	58.90
gap	24.30	512.41	524.56	536.71		
ax-st gap	1.89	536.71	537.66	538.60		
SuperLayer5 (U)	49.81	538.60	563.50	588.41	60	59.01
gap	24.19	588.41	600.51	612.60		
SuperLayer6 (V)	49.81	612.60	637.50	662.41	68	58.90
gap	25.19	662.41	675.01	687.60		
SuperLayer7 (A)	49.81	687.60	712.50	737.41	76	58.90
gap	24.36	737.41	749.59	761.77		
ax-st gap	1.33	761.77	762.44	763.10		
SuperLayer8 (U)	49.81	763.10	788.01	812.91	84	58.94
gap	24.69	812.91	825.26	837.60		
SuperLayer9 (V)	49.81	837.60	862.50	887.41	92	58.90
gap	25.19	887.41	900.01	912.60		
SuperLayer10 (A)	49.81	912.60	937.50	962.41	100	58.90
gap	27.59	962.41	976.21	990.00		
Outer Wall	10.00	990.00	995.00	1000.0		
TOTAL	800.00				640	

where:

ΔR = radial thickness of the element.
R_i = radius at the inner surface.
R_c = radius at the middle.
R_o = radius at the outer surface.
N = number of cells in the superlayer.
Cell Width = full width at the middle of the layer.
ax-st = gap needed for axial to stereo transition.

chamber. It is well known that tracks are best found in the axial projection, where all trajectories are arcs of circles independent of their dip angles. However, stereo layers are needed in order to measure the z vertex coordinate and the inclination of tracks. To increase the pattern recognition power of the CDC, charge division is to be implemented on every sense wire.

A good determination of the z coordinate of the hits in a stereo layer would allow projection of the hits into the midplane of the chamber with an accuracy given by

$$\sigma_{stereo} = \sigma_z \sin \theta_{stereo}$$

where σ_z is the z resolution. A value of $\sigma_z = 0.27\% \, \ell$ has been achieved in a 1-m-long prototype chamber by Bartalucci et al.[3] For a wire length of ℓ=180 cm and 50 mrad stereo, a σ_z of $\pm 1.0\% \, \ell$ gives a σ_{stereo} of 940 μm. It can be shown (Section 5.5.3) that this value of σ_{stereo} is comparable to the error incurred in linking the axial superlayer vectors. Hence these stereo layer hits are usable in pattern recognition.

The high multiplicity of the events requires that the charge associated with particular hits be identified: simply integrating all charge emerging from the wire is not enough, as there may be contributions from more than one hit. The solution proposed for this problem is to use waveform samplers to record the pulse shapes at each end of the wire as functions of time. For hits whose drift distances are separated by more than 2-mm, it will be possible to separate the integrated charge, as illustrated in Figure 5.26. Measurement of the z coordinate is not possible for those hits inside this dead region.

An analysis[5] of the requirements for low noise and linearity in the charge division, as well as for good drift time measurement indicates that the optimum wire resistance is well met by 30-μm stainless steel wire.

As mentioned previously, the signals from each end of the wire are input to waveform samplers (Section 5.2.5), whose design differential nonlinearity is better than 0.5%. Tests will be made with a prototype chamber to evaluate the precision we can attain. However, the results of Bartalucci et al. indicate the level of accuracy that has been achieved previously.
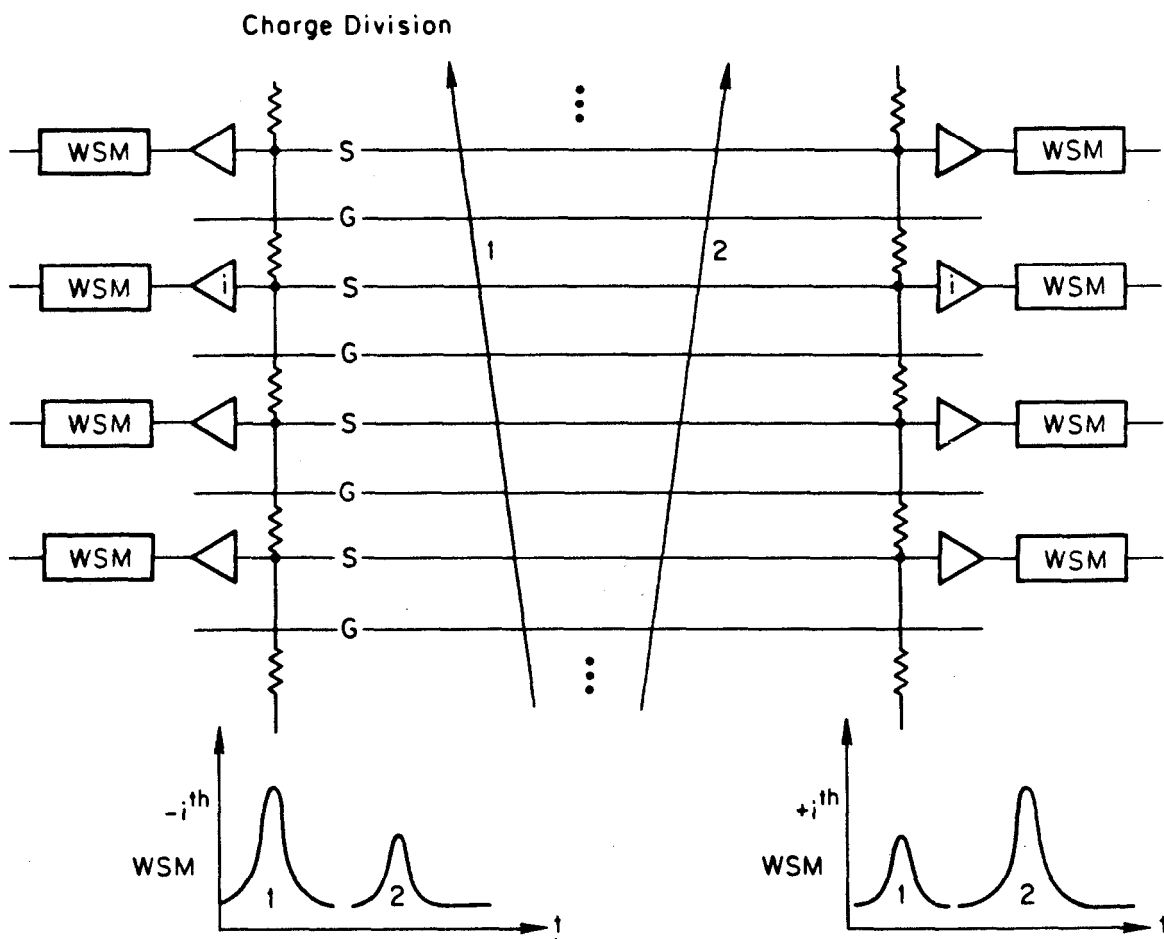
Figure 5.26. Schematic drawing of readout of wires by waveform samplers. Pulses for two tracks, 1 and 2, are shown for the ith sense wire. The times of arrival are different and the ratios of the charges on the two ends reflect different z coordinates. Multiple hits on wires can be distinguished in this system.
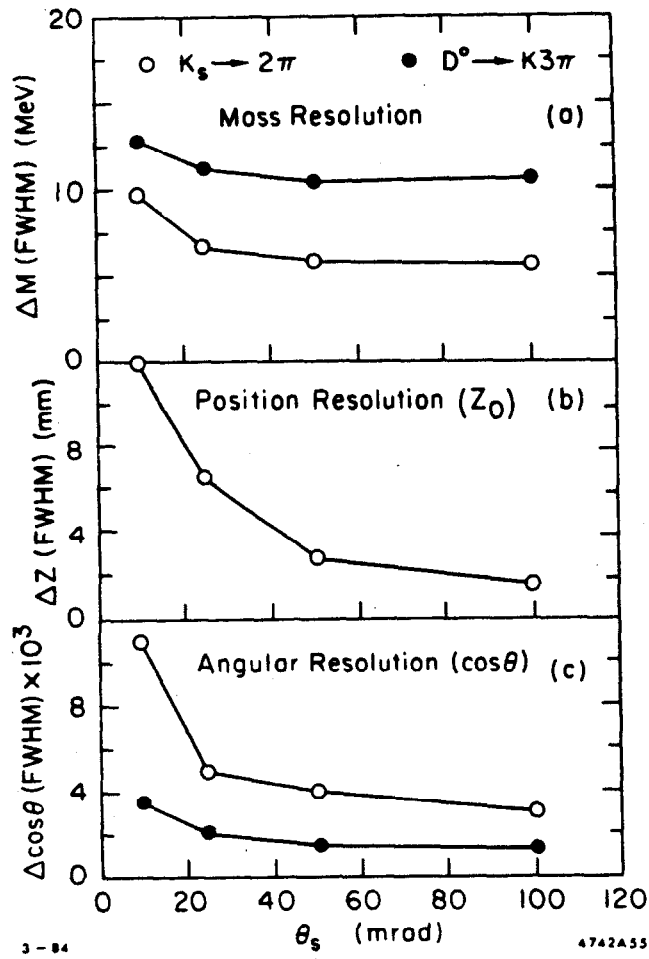
Figure 5.27. (a) Expected mass resolution of D^0 and K_s vs stereo angle. (b) Expected z_0 resolution vs stereo angle. (c) Expected polar angle resolution vs stereo angle. The mass and dip angle resolutions plateau above 35 mrad, while the z_0 resolution continues to improve.

5 - 44

The effect of the stereo angle on mass resolutions and track parameters has been estimated in a Monte Carlo simulation of the drift chamber. Mass, z-position and polar angle resolutions as functions of stereo angle, θ_{stereo}, are shown in Figure 5.27. The polar angle and mass (K_s and D^o) resolutions plateau above $\theta_{stereo} = 35$ mrad, while the z-position resolution continues to improve as the stereo angle increases. Good z-position resolution improves the ability to join up tracks from the drift chamber with the CCD vertex detector hits.

A stereo angle of 50 mr yields a resolution in the $x - y$ plane comparable to the estimated linking error. As θ_{stereo} increases, σ_{stereo} increases, and the stereo layers become less competitive with the axial layers in the pattern recognition. These criteria limit the stereo angle to lie within

$$35 < \theta_{stereo} < 50 \text{ mrad} .$$

A simulated $e^+ e^- \to Z^o \to t\bar{t}$ event including background hits is shown in Figures 5.28, 5.29, 5.30 and 5.31, illustrating the hit pattern in the CDC in the r vs ϕ view. Figure 5.28 shows the information available from the axial layers alone; Figure 5.29 includes the stereo layers by dint of the charge division projection into the midplane. Figure 5.30 shows an expanded view of a region in ϕ; the tracks are very clearly visible to the eye. Figure 5.31 shows the hit pattern in the z vs ϕ view after the hits have been correctly associated with tracks. This illustrates the quality of the initial guess of the polar angle that the track fitting will have available to it from the charge division information. Straight lines are expected with slope proportional to $tan\ \lambda$, where $\lambda = \pi - \theta$.

5.2.5 Electronics

Specifications

The electronics for both the central drift and endcap regions are similar; the minor differences are discussed in Section 5.3.1. The proposed electronics can measure both the time of arrival and the charge of the ionization pulses in a single device, the waveform sampler. The gas mixture has drift velocity of 10 μm/ns, which for the wire spacing of 3 cm gives a maximum drift time of 3 μs.

6. Particle Identification (CRIDS)

6.1 PRINCIPLES OF OPERATION

6.1.1 General

The flavor tagging in *SLD* will be accomplished by the very powerful combination of the high-precision vertex detector and the Čerenkov-ring-imaging detector (*CRID*). This will be a unique approach to the problem since the *SLC* machine parameters permit installation of the vertex detector close to the interaction point and, consequently, rather high tagging efficiency for the weak decays of heavy quarks and leptons. The final state particle identification from the Čerenkov counter together with this secondary vertex tag allows extremely clean charm and bottom signals to be obtained with high efficiency. As examples of the power of this system, the D signal in $K\pi$ and $K\pi\pi$ mass plots as derived from $Z°$ decay jets using the *SLD* flavor tag system are shown in Figures 6.1 and 6.2. Very clean mass peaks are observed, permitting background-free detailed studies of *CP* violation or cascade decay parameters. The efficiency and cleanliness of an inclusive D meson tag are summarized in Figure 6.3.[1]

The *CRID* differs from the classical Čerenkov counter in that it provides e, π, K and p separation over a wide range of momenta, and not a simple binary yes/no decision between two particle species over a limited momentum range. The principle was first put forward many years ago by Arthur Roberts[2] and recently given a new lease on life by the practical proposal from Ypsilantis and Seguinot.[3] It has now been adapted to several quite different experimental geometries.[4]

6.1.2 Principle of Ring-Imaging Detectors

When Čerenkov light from a charged particle is optically focused onto a detector, the radius of the circle of Čerenkov light is a measure of the Čerenkov angle, which in turn is a measure of the velocity of the particle. The information on the velocity and the momentum of the particle permits an estimate of the particle mass. A device with gas and liquid radiators and with an ultraviolet photon detector allowing a few percent determination of the Čerenkov angle,
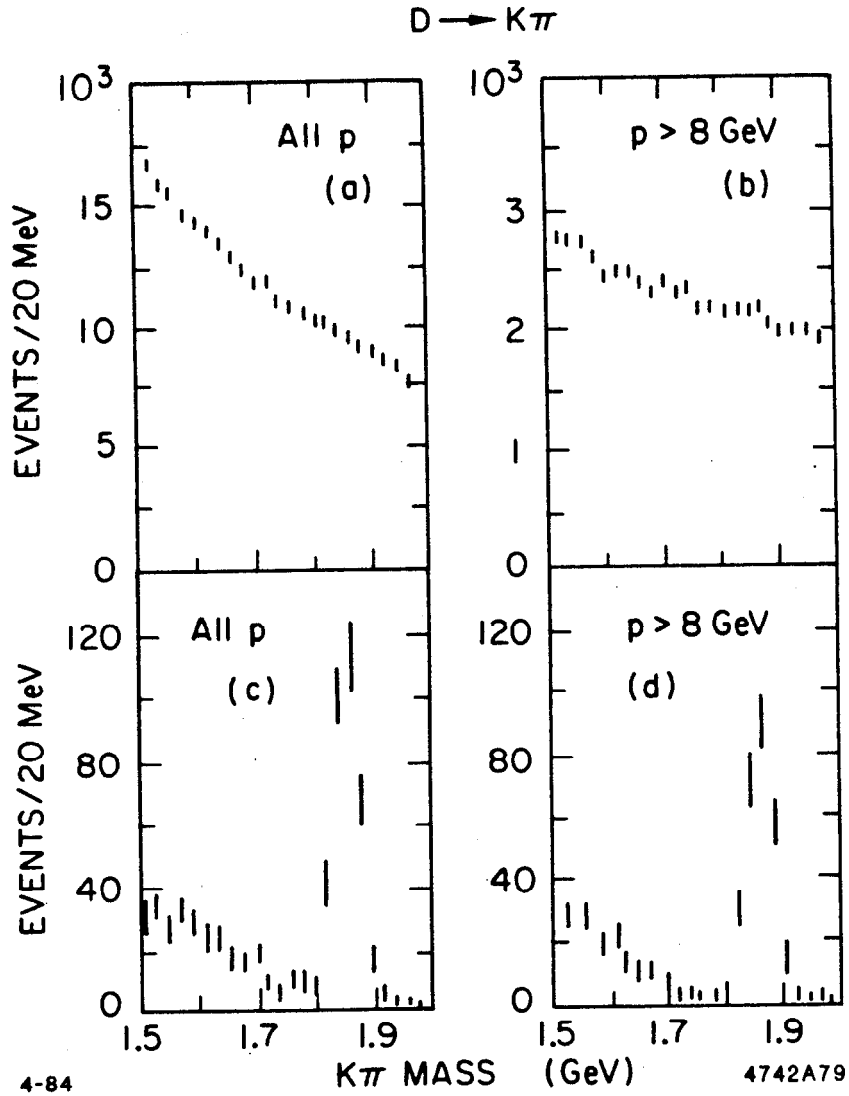
Figure 6.1.   The number of events versus $K\pi$ mass for two particles from the same side jets produced in Z^0 decay; (a) and (b) for all neutral charge combinations; and (c) and (d) after topology selection and particle identification in the SLD. (a) and (c) include all secondary momenta while (b) and (d) include high momenta only ($p_{tot} > 8$ GeV/c).
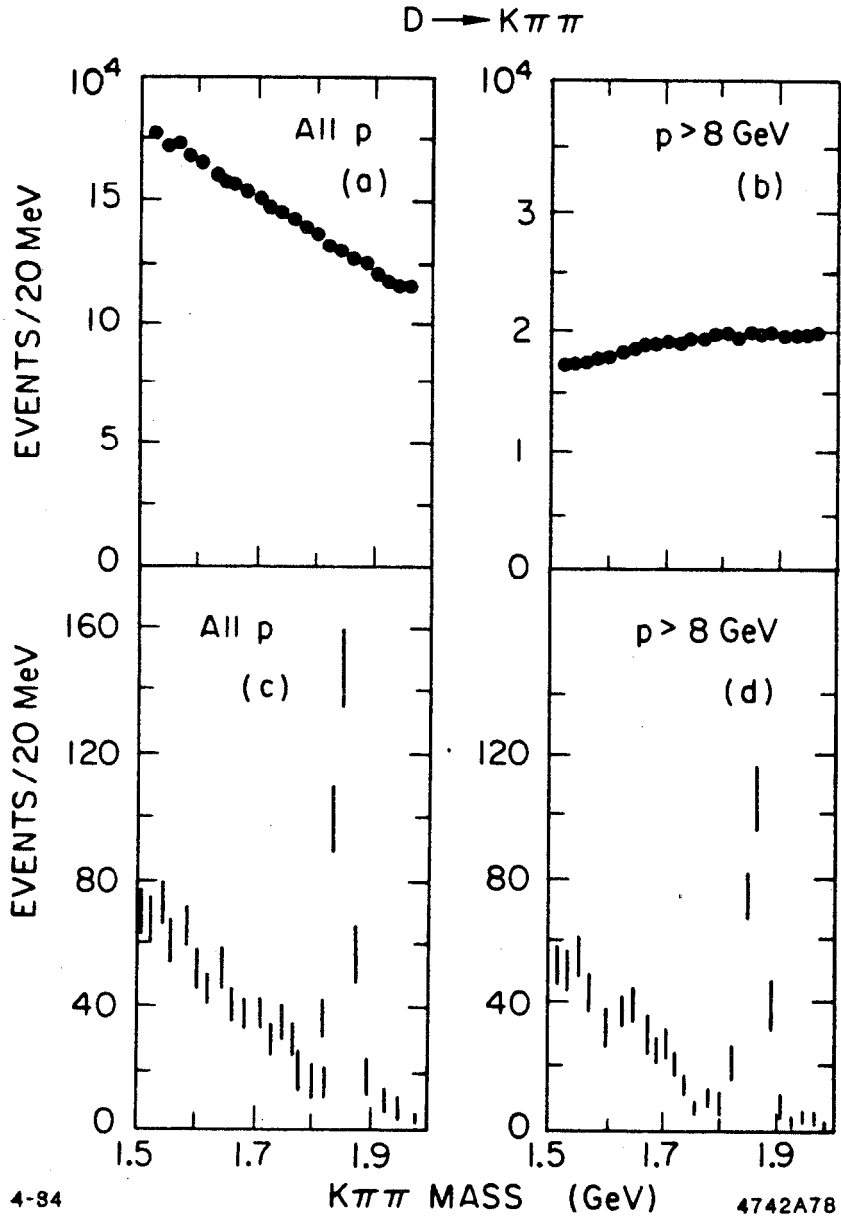
Figure 6.2. The number of events versus $K\pi\pi$ mass for three particles with total charge plus or minus one from same side jets produced in Z° decay; (a) and (b) for all combinations; and (c) and (d) after topology and particle identification cuts in the *SLD*. (a) and (c) include all secondary momenta while (b) and (d) include high momenta only ($p_{tot} > 8$ GeV/c).
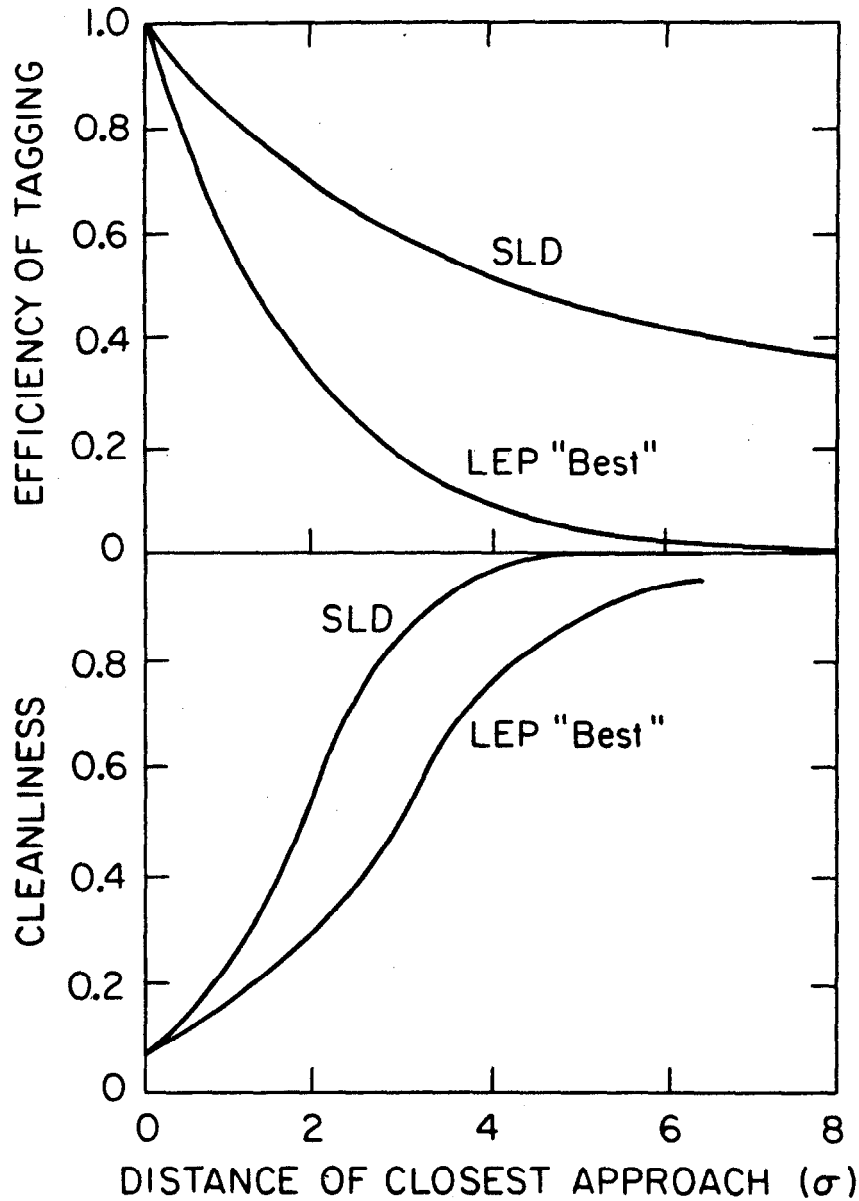
Figure 6.3. (a) The fraction of D decays containing a charged K which can be tagged (efficiency) versus the number of standard deviations by which the track misses the origin for the SLD and for a 'best' LEP detector. The LEP detector is assumed to have a ring imaging Čerenkov system allied to a good vertex detector, but placed much further from the interaction point, consistent with the design of the LEP machine. (b) The fraction of identified K tracks which miss the origin by more than the given number of standard deviations which come from D decays.

6 - 4

will provide good π, K and p separation over essentially the full momentum range of *SLC*. Combined with the calorimetry, this also provides good lepton and hadron identification over the full momentum range.

In Figure 6.4(a), a charged particle passes perpendicularly through a thin liquid radiator producing light at approximately 45° depending on the particle velocity and the index of refraction of the liquid. If this Čerenkov light is allowed to propagate some distance before encountering the photon detector, it will form a 'proximity focused' image at the detector. Light produced in the gas radiator is focused back onto the photon detector by spherical mirrors and forms a sharp image whose radius depends on the magnification of the optical system, the index of refraction of the gas, and the velocity of the particle. Using liquid (*FC-72*) with an index of refraction $n = 1.277$ and isobutane with $n = 1.0017$, the proximity focused circle for a relativistic particle would be around 17 cm radius and about 1.5 cm thick for the liquid, and approximately 3 cm in radius and less than 1 mm thick for the gas as shown schematically in Figure 6.4(b).

The Čerenkov photons from the charged particle of interest pass through quartz windows on the front and back of the detector box and are converted by photo-ionization of gaseous *TMAE* (Tetrakis Dimethyl Amino Ethylene), which has a very high quantum efficiency in the range 1700 to 2200 Å. The detector box is wound with a field cage establishing an electric drift field along the axis of the detector box, as shown in Figure 6.5. The photoelectrons drift at constant velocity down the box until they arrive at the detector, which is a picket fence of multi-wire proportional counters. The coordinates of the point of origin of the photoelectron are recorded as the drift time of the electron and the wire address at which the electron was counted. The conversion depth which gives the parallax error comes from the third coordinate information. The Čerenkov angle for the many photons from each charged particle may, in principle, be measured to an accuracy of a few percent, allowing unambiguous identification of final state particles from below 1 GeV/c up to over 35 GeV/c.

Table 6.1 summarizes the properties and parameters of the proposed *SLD* Čerenkov Ring Imaging Device.

(b)

20
15
cm 10
5
0

Liquid
Radiator
Image

Gas
Radiator
Image
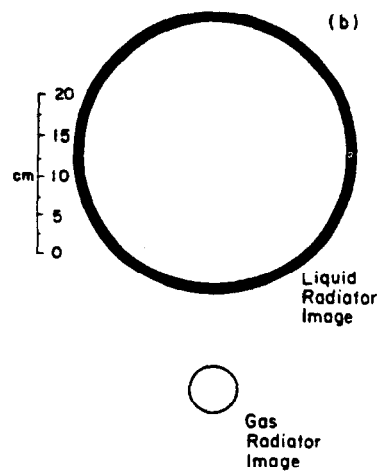
SCHEMATIC OF RING IMAGES

4-84   4742A122

(a)

PHOTOELECTRON
CONVERSION AND
DRIFT REGION

SPHERICAL
MIRROR

LIQUID
RADIATOR

GAS RADIATOR

4-84
4742A123
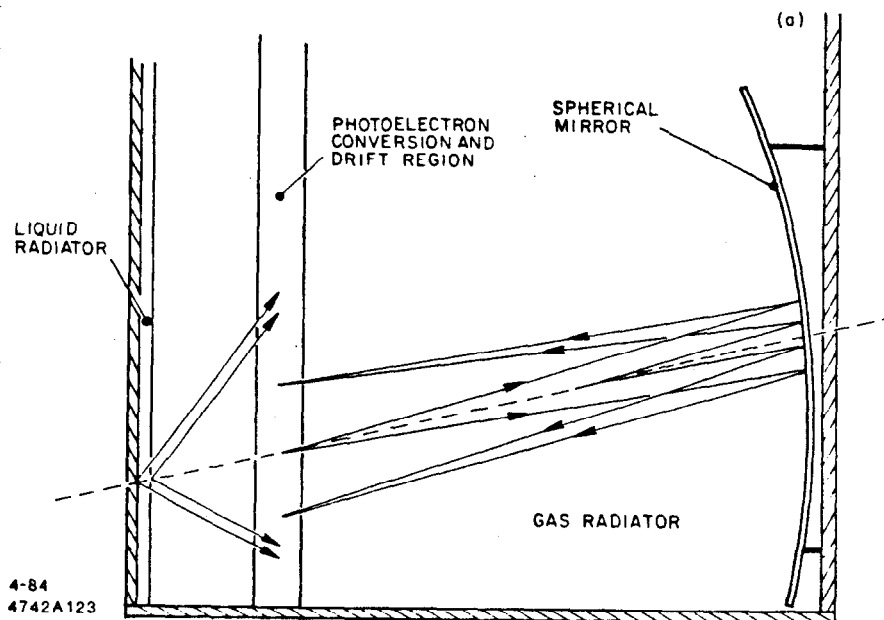
Figure 6.4.   (a)   The *CRID* principle for a two-radiator system. (b)   Size and thickness of ring images produced at 90° in a liquid and gas radiator.

6 - 6

PHOTONS FROM
GAS RADIATOR

CATHODE PLANE
THIRD COORDINATE

ANODE WIRE
PLANE

e⁻

TIME

WIRE
ADDRESS

PHOTONS FROM
LIQUID RADIATOR

4-84

4742A121
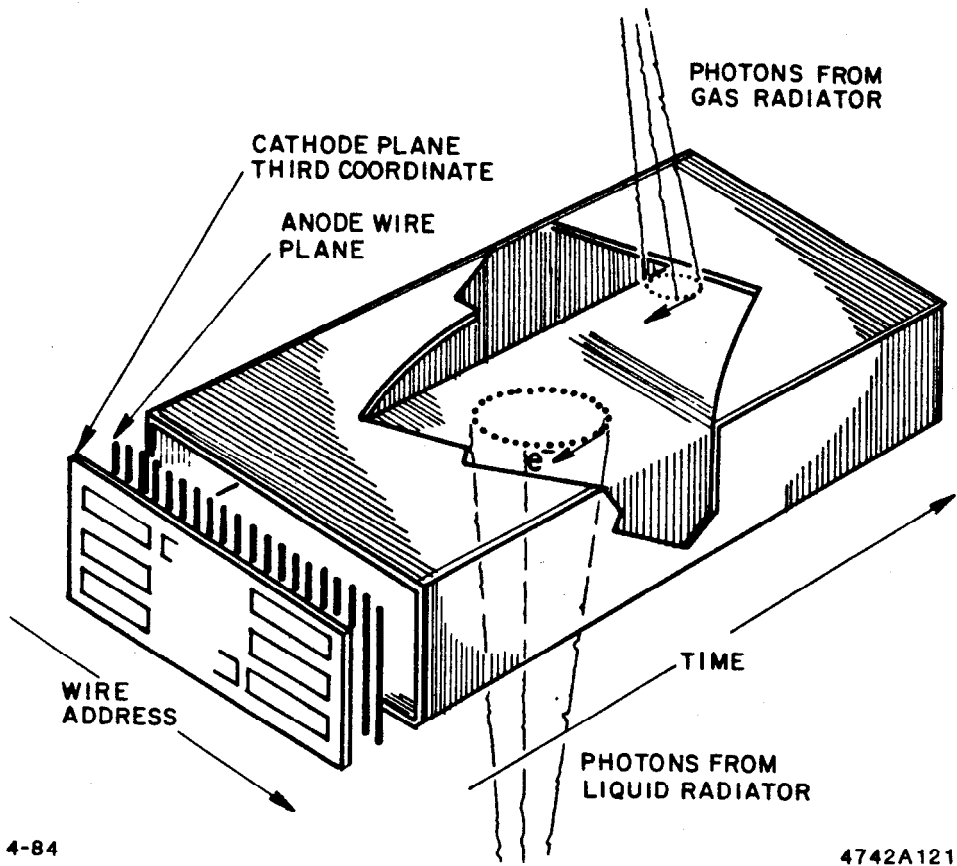
Figure 6.5. Photon detector schematic.

Table 6.1.
Summary of Parameters of *SLD CRID*

			Liquid	Gas
1.	Solid Angle Coverage		98%	94%
2.	Angular Coverage	(Endcap)	10.5°—37°	8.5°—33°
		(Barrel)	37°—90°	38°—90°
3.	Radiator Material		*FC-72*	isobutane
4.	Index of Refraction	(at 6.5 eV)	1.277	1.0017
5.	Thickness of Radiator		1 cm	$\sim$ 45 cm
6.	Focusing Method		proximity	spherical mirror
7.	Čerenkov Threshold γ		1.61	17.52
8.	Čerenkov Angle	(for $\beta = 1$)	670 mrad	58 mrad
9.	Radius of Čerenkov Ring	(for $\beta = 1$)	17 cm	2.8 cm
10.	Number of Photoelectrons	(for $\beta = 1$)	23	14
11.	Momentum Threshold	(for 3 p.e.)		
	e		~ 1 MeV/c	~ 10 MeV/c
	π		0.23 GeV/c	2.6 GeV/c
	K		0.80 GeV/c	9.5 GeV/c
	p		1.50 GeV/c	17.8 GeV/c
12.	Particle Separation Range at 90° (3 σ Level)		[both radiators]	
	e/π		(0.2 to 7 GeV/c)	
	μ/π		$\begin{cases} (0.2 \text{ to } 1.1 \text{ GeV/c}) \\ (2.1 \text{ to } 4 \text{ GeV/c}) \end{cases}$	
	π/K		(0.230 to 32 GeV/c)	
	K/p		(0.800 to 55 GeV/c)	

6.1.3 Measurement Errors

The accuracy with which a CRID measures the Čerenkov angle, θ_C, of a particle is determined by the individual contributions from five separate sources of error,[5]

$$\delta\theta_C = \left[\delta\theta^2_{\text{chrom}} + \delta\theta^2_{\text{meas}}\right.$$

$$+ \frac{\delta\theta^2_{\text{mult scatt}}}{p^2}$$

$$\left. + \delta\theta^2_{\text{geom}} + \frac{\delta\theta^2_{\text{mom}}}{p^2}\right]^{\frac{1}{2}}$$

for a single photoelectron.

    (a)   Chromatic error

This error comes from the variation of index of refraction (and hence, the Čerenkov angle) as a function of the wavelength of the light detected. For the liquid radiator (FC-72), this is a $\pm$ 3.1 mrad contribution over the wavelength range where TMAE photo-ionizes and the gases and quartz transmit (i.e., $1700 < \lambda < 2200$ Å). For the gas radiator (isobutane) the chromatic term amounts to $\pm$ 1.1 mrad uncertainty in the measurement of the Čerenkov angle.

    (b)   Measurement error

This contribution comes from the granularity of the Čerenkov photo-electron detector, and from non-uniformities in the spatial resolution of the detector. For the liquid radiator, these errors are about ± 1.5 mrad due to the resolution in the detector plane ($\sigma_x \approx \sigma_y \approx 0.8$ mm) and about ± 3 mrad due to the resolution in determining the conversion depth of the photoelectron ($\sigma_Z \approx 1.4$ mm). For the gas radiator, the spatial resolution in the detector plane ($\sigma \approx 0.8$ mm) gives an angular uncertainty of $\pm$ 1.7 mrad.

    (c)   Multiple Scattering

This term is driven by the scattering of the charged particle in the outer wall of the drift chamber and the inner wall of the CRID, the

quartz and liquid freon and the detector box. It is not an important contribution, being $\pm\frac{1.4}{p}$ mrad for the liquid radiator and $\pm\frac{0.4}{p}$ mrad for the gas radiator.*

(d) Geometric

This term is driven by aberrations of the image of the Čerenkov circle due to the optical arrangement employed—either the focusing mirror system or the proximity focus of the thin radiator. In the case of the liquid radiator this term contributes $\pm$ 5.1 mrad at 90°. This error depends rather strongly on the production angle of the charged particle under study, and for each production angle it varies strongly with the azimuthal angle of emission of the Čerenkov photons. The envelope of this error contribution runs from about 3.5 mrad up to about 15 mrad. For the gas radiator the error is $\pm$ 0.1 mrad, and comes mainly from the aberrations in the detector plane from off-axis rays being reflected from the extreme areas of the spherical focusing mirrors.

(e) Momentum Smearing

This term is due to the change in the trajectory of the charged particle as it passes through the radiator volume, under the action of the magnetic field. This causes a blurring, or smearing, of the Čerenkov circle image. The error contribution to the Čerenkov angle measurement depends on the angle of emission of the photon, ranging from zero for photons emitted parallel to the magnetic field, up to a maximum value for photons emitted normal to the magnetic field. For the liquid radiator the average contribution is about $\frac{0.6}{p}$ mrad, while for the gas it is $\frac{30}{p}$ mrad. The momentum resolution of the central drift chamber does not significantly add to the uncertainty of the particle identification determination.

---

* The effect of the multiple scattering error is algorithm dependent. The particle multiple scatters in an inner wall causing the entire image to shift. If the photoelectrons are fit to the expected ring image size and shape, the Čerenkov angle is determined without referencing the incident particle track.

ANGULAR RESOLUTION OF SLD CRID
FOR RELATIVISTIC PARTICLES
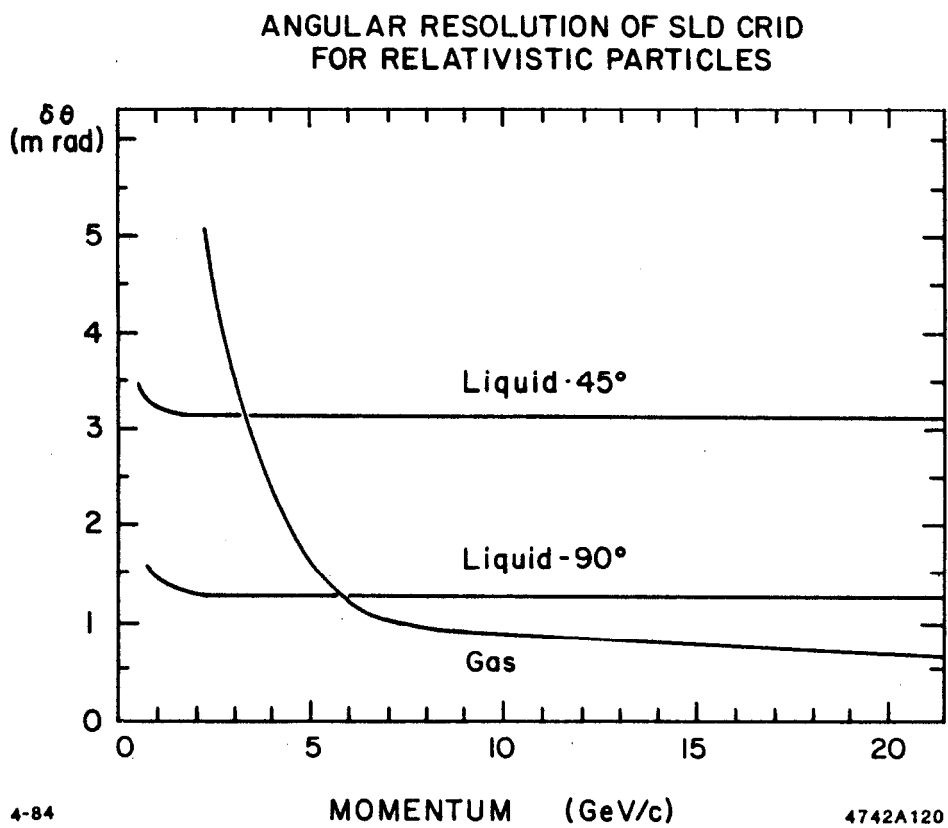
Figure 6.6. Čerenkov angular resolution versus momentum, for relativistic pions.

For the liquid radiator each photoelectron detected contributes an uncertainty of about ±7 mrad, and the Čerenkov angle (using the information from all of the photoelectrons) should be measured to an accuracy of about ±1.5 mrad. The angular resolution for the gas radiator is quite momentum dependent, but for momenta above 5 GeV/c each photoelectron should allow about (2-3) mrad accuracy. Thus the Čerenkov angle for a track should be measured to better than 1 mrad. The angular resolution measurements are summarized in Figure 6.6.

6.1.4 Problems

The problems that must be solved in the design and realization of a *CRID* are:

    (a)   Minimizing all sources of aberrations of the Čerenkov circle on the detector plane;

    (b)   Developing a large-area, high-quantum efficiency photocathode to detect the image of the Čerenkov circle;

    (c)   Developing an efficient, single-electron detection system which is immune to the regenerative photon feedback background;

    (d)   Keeping all gases, liquids, and surfaces clean such that the far *UV* reflectance and transmission are maintained near their maximum value for the life of the experiment;

    (e)   Maintaining good control of all fields affecting the drift of the single photoelectrons;

    (f)   Signal processing, and

    (g)   Pattern recognition.

6.1.5 Choice of Materials for the CRID

    (a)   The Liquid Radiator

        The choice of the material for the liquid radiator is driven by the need to have good transparency in the far ultraviolet with small chromatic dispersion and as low an index of refraction as possible. The best candidate (without using materials that require cryogenic temperature

Figure 6.7.   Index of refraction as a function of wavelength for *FC-72* and isobutane

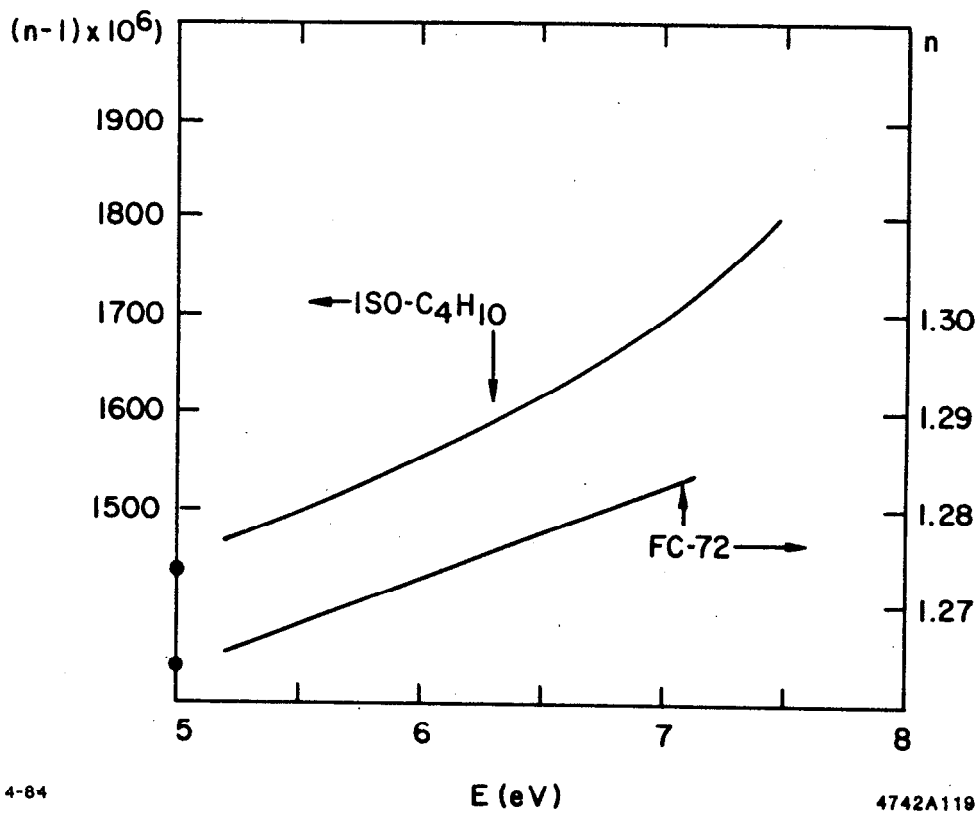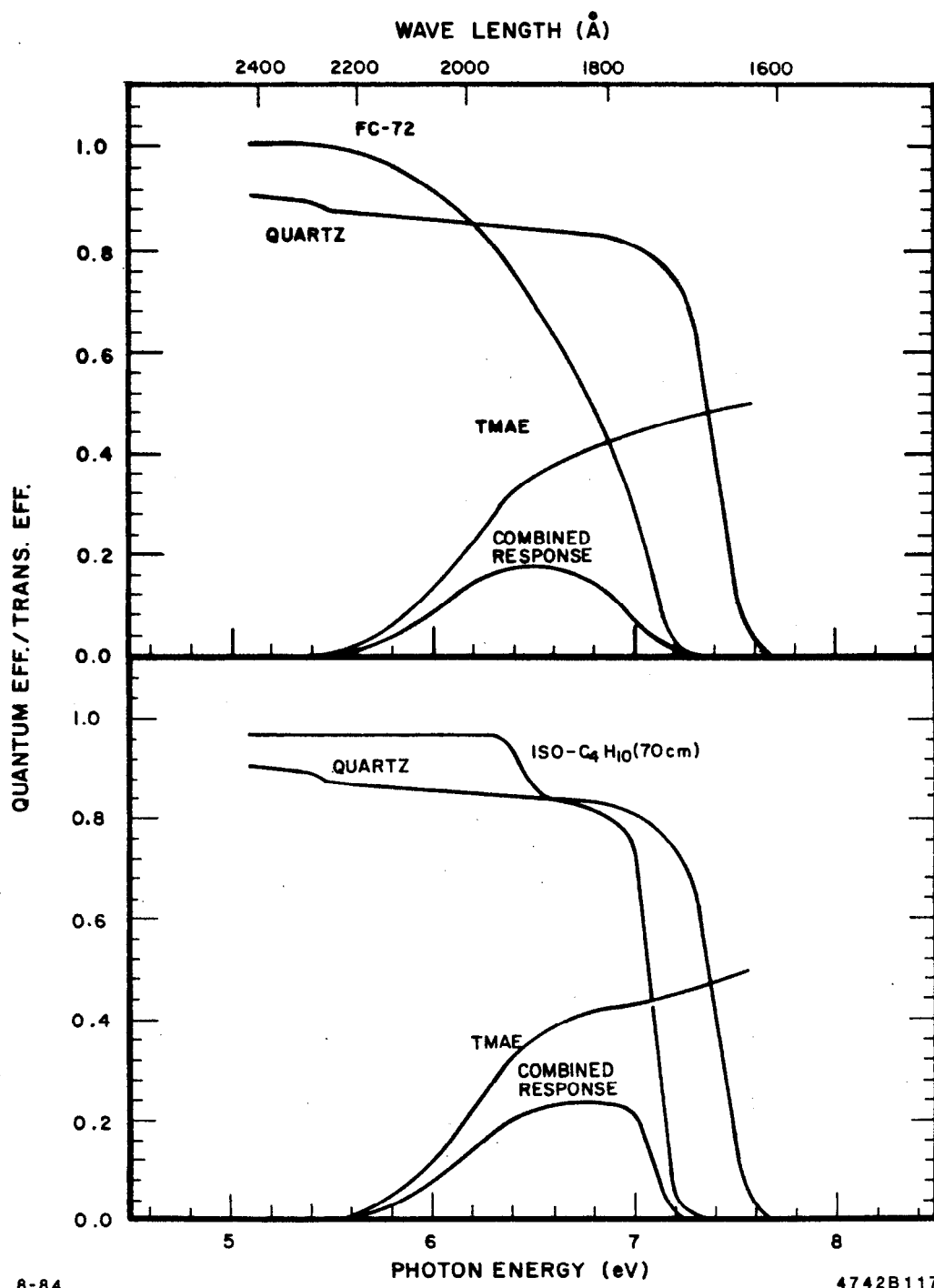Figure 6.8. (a) Transmission curves for quartz, isobutane, and the quantum efficiency of *TMAE* versus photon energy. (b) Transmission curves for quartz, *FC-72* and the quantum efficiency of *TMAE* versus photon energy.

control to remain liquid) is *FC-72*: C_6F_{14}, perfluoro-n-hexane, with small admixtures of other isomers and some other perfluoro-paraffins. It has an index of refraction around 1.277 in the wavelength region of interest, and a rather small chromatic dispersion (See Figure 6.7). The useful wavelength window for the *SLD CRID* is given by the absorption and transmission properties of the materials chosen; the resulting window is 1700-2200 Å as summarized in Figure 6.8.

The great affinity of *FC-72* for absorbing gases (see Table 6.2), especially oxygen, can cause reduced *UV* transmission and, hence, reduced overall quantum efficiency. Thus it is essential to keep the *FC-72* free of dissolved gases. The transmission of *FC-72* is shown in Figure 6.9 for a liquid at three different levels of cleanliness: a) spectroscopic grade C_6F_{14}, b) an *FC-72* sample after passing through an Oxisorb filter, and c) an *FC-72* sample left standing in a partially sealed container. The properties of the *FC-72* radiator are listed in Table 6.3. As discussed in more detail below (Section 6.2) the *UV* transmission of *FC-72* will be maintained by continuously circulating the liquid through a purification system.

(b)   The Photon Detector

TMAE is the photocathode material. It has a good quantum efficiency of about 50% at wavelengths that allow the use of quartz windows (instead of calcium fluoride) and makes the device much less sensitive to oxygen and water-vapor poisoning. The quantum efficiency of *TMAE* is displayed in Figure 6.8, while the transmission coefficients of O_2 and H_2O are given in Figure 6.10. Since *TMAE* has a rather small vapor pressure at room temperature, and a rather long absorption length for the Čerenkov photons, the *TMAE* bubbler will be heated to 28° C, where the attenuation length in the 1700-2200 Å region will be about 12 mm (see Figure 6.11).[6] To avoid *TMAE* condensation the whole *CRID* will be run at a temperature of 35°C.
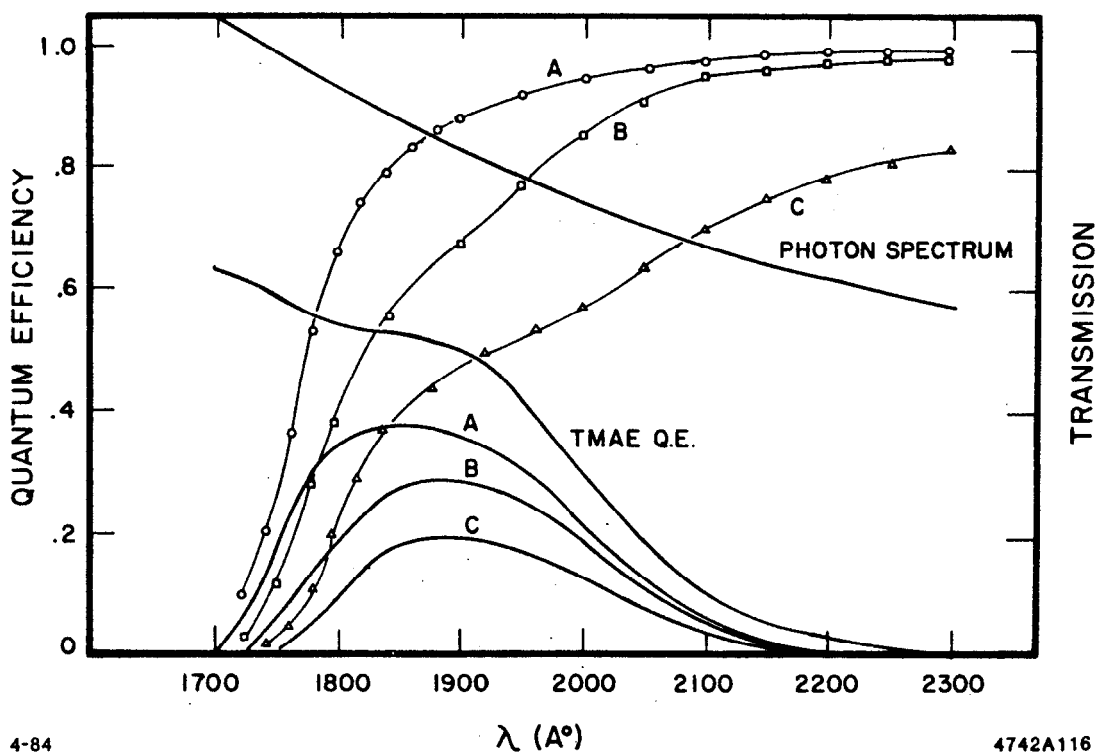
Figure 6.9. Transmission of three *FC-72* samples as a function of wavelength:

    (a) Spectroscopy grade C_6F_{14}.

    (b) After circulation through Oxisorb filter.

    (c) *FC-72* after exposure to air (O_2 and H_2O, etc.).
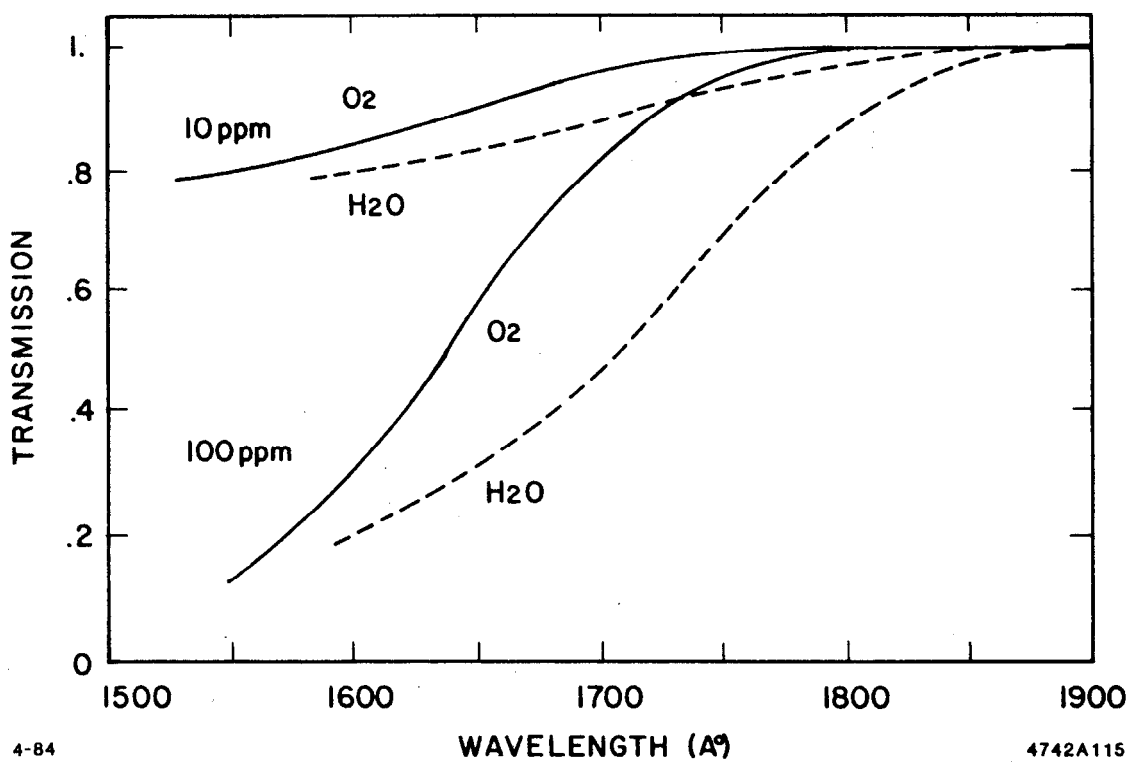
Figure 6.10. *UV* transmission of 1 meter of oxygen and H_2O at 10 and 100 ppm.
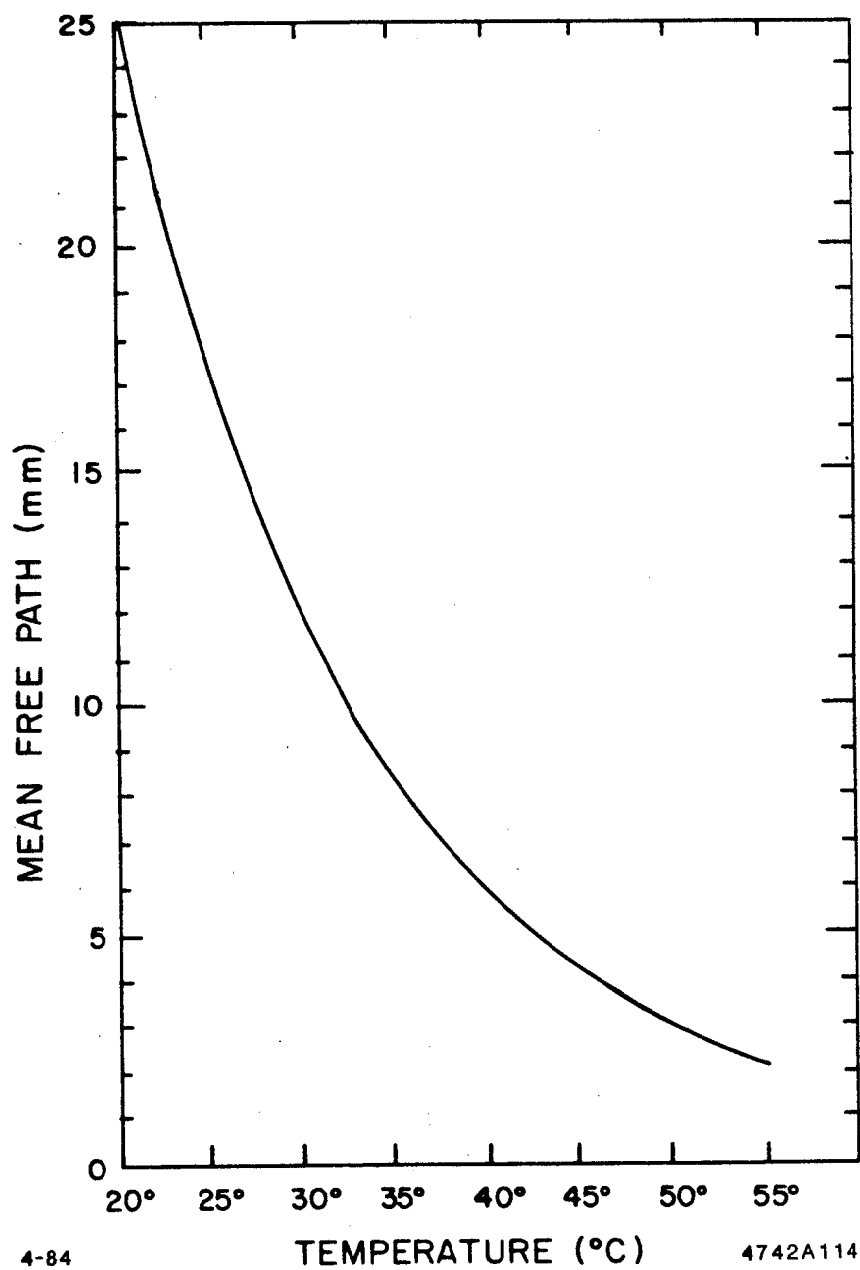
Figure 6.11. The absorption length for (1700-2200) Å *UV* light in a saturated *TMAE* vapor, as a function of the temperature of the system.

Table 6.2

Solubilities of Various Materials in *FC-72*

		Removed by Oxisorb?
H_2O	10 ppm	Y
Air	48 ml (gas)/100 ml (liquid)	-
Oxygen	65 ml (gas)/100 ml (liquid)	Y
CO_2	248 ml (gas)/100 ml (liquid)	Y
CH_4	92 ml (gas)/100 ml (liquid)	N

Table 6.3

Properties of *FC-72*, ($C_6 F_{14}$)

Boiling Point	56°C
Radiation Length	34.7 g/cm^2
Refractive Index (6.5 eV)	1.277
Vapor Pressure (at 25°C)	232 torr
Density	1.68 g/cm^3 (at 25°C)
	1.65 g/cm^3 (at 30°C)

(c) The Gas Radiator

The gas radiator choice is motivated by the desire to close the momentum gap between the upper limit of the liquid radiator performance curves and the thresholds for the gas counter. Other considerations are good transparency between 1650 and 2200 Å and low dispersion of the index of refraction. Candidate gases are isobutane and *FC-87* vapor. The former has good transparency and a reasonable index, whereas *FC-87* has a slightly better index at 40°C [(n-1) $\times 10^6$ = 1800 versus 1700 for isobutane] and has the additional advantages of being non-flammable and an excellent insulator. Even though *FC-87* appears to offer superior performance, there is no experience with it at this time and its low vapor pressure introduces operational and design difficulties which need to be understood. Isobutane is the present choice for the *CRID* design, and studies of *FC-87* are continuing.

The dispersion and transmission properties for isobutane are given in Figure 6.7 and Figure 6.8(a), respectively. Oxygen and water vapor must be kept below the 20 ppm level to maintain good transparency along the 100 cm path length to and from the mirrors.

6.2 SYSTEM DESIGN

6.2.1 Geometry and Optics

Geometry

The *CRID* design is motivated by the desire to cover 4π solid angle as completely as possible within the constraint of the solenoidal field geometry chosen for the detector. The practical design consists of a barrel region plugged at both ends with endcaps as shown in Figure 6.12. Each of these regions contains an inner liquid radiator, an outer gas radiator, and a photon detector capable of detecting photons entering through either the inner or outer surfaces. In the barrel the three components are concentric cylinders with the photoelectrons drifting parallel to the collinear electric and magnetic fields. In the endcaps the components are coaxial disks with the photoelectrons drifting transverse to the magnetic field.

Gas Radiator Region

Spherical
Mirrors

Field Cage

Detector

High Voltage

Detector

Drift Region

FC-72 Radiator

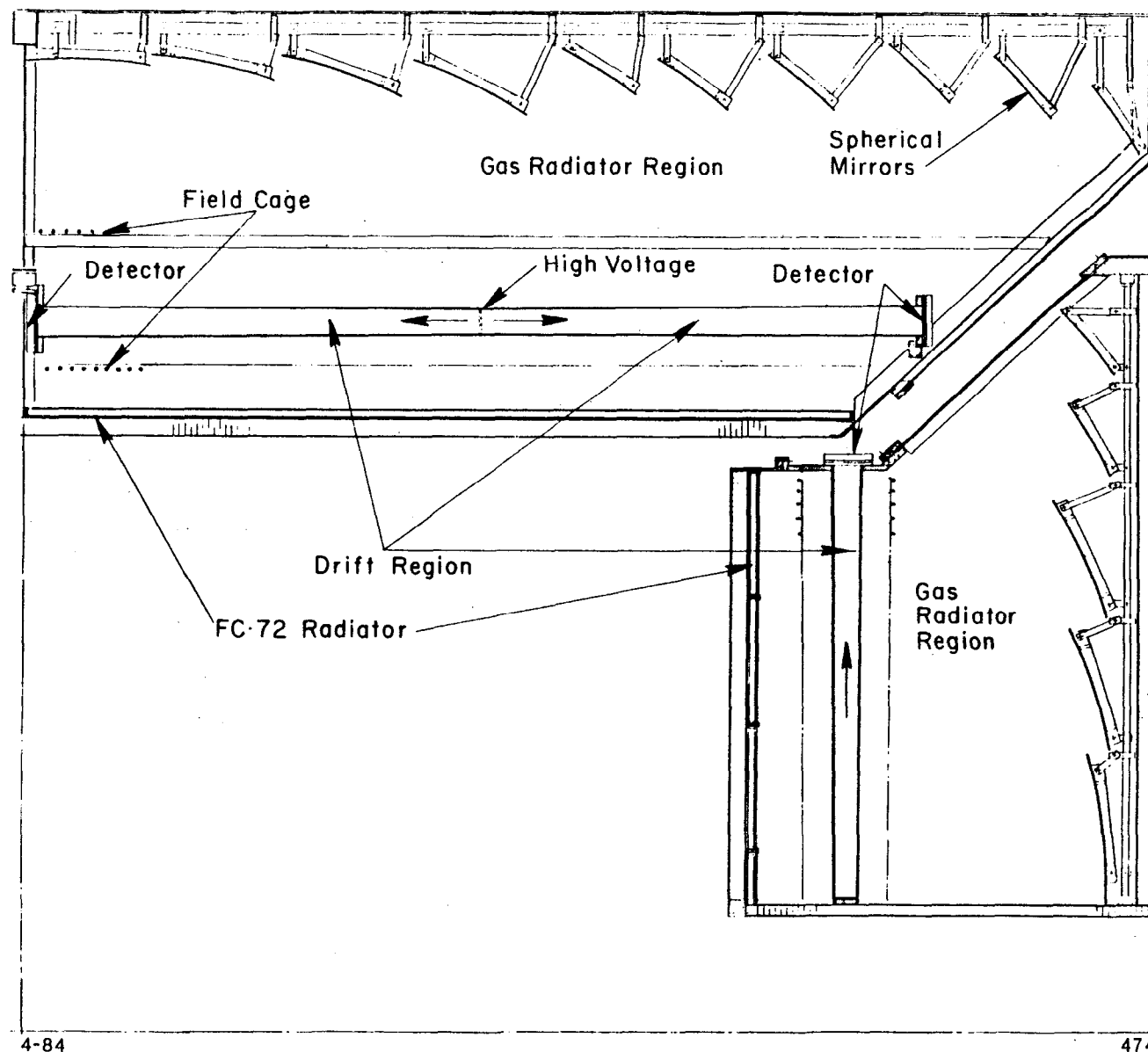Gas
Radiator
Region

4742A132

Figure 6.12.   Schematic of barrel and endcap longitudinal section.

The photoelectron detectors in the barrel are long staves in which the electrons drift parallel to the magnetic field under the influence of a uniform electric field. To reduce the overall drift length of any one element and to keep the maximum voltages to moderate values, the barrel staves are divided into four sections with proportional wire detectors at each end. High voltage is applied at the one-quarter and three-quarter points along the barrel with electrons drifting either toward the mid-plane or toward the ends of the barrel.

The barrel ends are closed by the endcap *CRID* devices. The relative positions of the liquid and gas radiator and the photon detector are the same as in the barrel region. The liquid radiator is held in a flat vertical disk by containers described in Section 6.2.2. The photon detector is also a flat, vertical disk with windows on both sides to accept photons from either radiator. The special problem of drifting photoelectrons transverse to the magnetic field is discussed in Section 6.2.3. The 128 mirrors in each endcap are also held in a flat array, each aimed back to the interaction point. A 20-cm-radius hole through the center of the three disks accommodates the beam line.

Optics

The optical systems for the two radiators will produce and focus Čerenkov light from particles emerging from the interaction region over the maximum possible solid angle. In the case of the liquid radiator the ratio of the passive radiator support system to active radiator surface must be minimized. For the gas radiator, the mirrors must intercept and image as much Čerenkov light as possible within the mechanical constraints of construction.

The geometrical optics of the mirror-imaged and proximity-focused rings is nearly ideal in equatorial (90°) and polar (0°) regions where the rings are full circles. In the 45° region, the optical distortions are always either small or comparable to other sources of error. In the equatorial and polar regions the images from the liquid form circles of approximately 17 cm in radius. As the polar angle goes toward 45°, the circles distort into ovals. For angles smaller than about 77° in the barrel, part of the oval is lost due to total internal reflection inside the liquid radiator. The loss of photons to internal reflection is compensated

partially by the particle's increased path length through the radiator.

In the gas counter the image is produced by a spherical mirror whose optic axis points back to the origin. With this orientation it is possible to produce high quality images at the detector surface, provided that the mirror dimensions are kept small. Though such a configuration requires the manufacture of many mirrors, their simplicity and small size makes their manufacture straightforward. This configuration has the additional virtue of matching well to the photon detector size demanded by the liquid counter. The optical characteristics of the mirror system are illustrated in Figure 6.13 for the gas section and in Figures 6.14 and 6.15 for the liquid system. Details are discussed in the performance section below (Section 6.4).

Mirror Construction

Mirrors of similar size and quality have been manufactured in substantial volume by groups elsewhere[7] and the techniques are rather well understood. The optical surfaces of the mirrors must be better than those required by conventional threshold Čerenkov counters, but need not be of astronomy quality. The reflectance must be high and optimized for the 1700-2200 Å region. The standard technique is to slump glass sheets over a spherical mold, and to follow with a polishing step to bring the image quality to the 0.25 mm tolerance needed to avoid dominating other sources of error. The mirrors are then aluminized and overcoated with MgF_2. Mirror reflectances of greater than 80% have routinely been attained in the wavelength region of interest between 1700 and 2200 Å. The number of mirrors is large (480 in barrel and 216 in two endcaps) but the small size of the mirrors lends itself to setting up several production lines based on groups with a common radius of curvature.

The Barrel Vessel

The barrel liquid radiator, drift boxes and mirror array are contained in a vessel whose inner wall is a cylinder made of 30-mm hexcell with 0.25-mm aluminum skins, and the outer wall is a cylinder of 3-mm aluminum. There are three structural rings on the outer cylinder made of G-10 and attached to the outer cylinders as shown in Figures 6.16 and 6.17. The rings are at the

45° Trajectory

Spherical Mirror

$f \sim 50\,cm$

Field Shaping Electrodes

Čerenkov
Photon

θ_c

Particle
Trajectory

Focal Plane
$f \sim 50\,cm$

Drift
Region

Drift
Region

Particle
Trajectory

Focal Plane

4742A113

4-84

4742A130

4-84
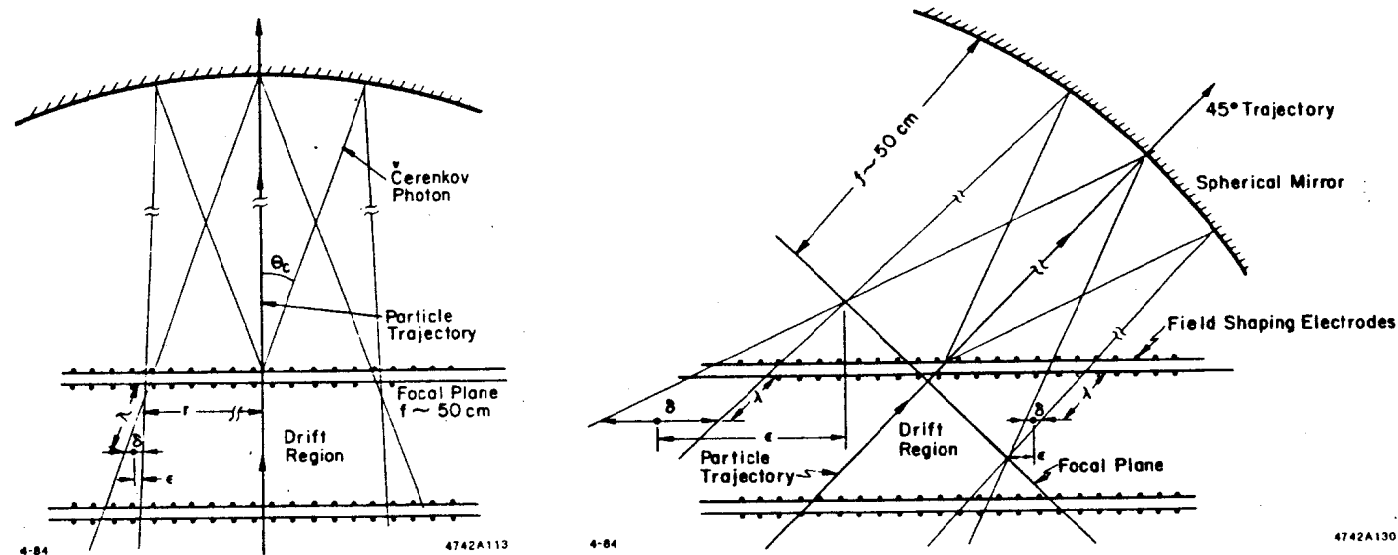
Figure 6.13.   Schematic representation of gas radiator optical arrangements.

(a) 90° region. In the 90° and 0° regions the focused image of the Čerenkov ring
intercepts the detector box at normal incidence and the focal plane is parallel to
the surface. The image is broadened (δ) due to the finite absorption length (λ) of
TMAE. This defocusing error cannot be corrected. (b) 45° region. In the chosen
optical arrangement for the gas radiator, the mirrors point toward the interaction
point. Consequently, the focal plane of the imaged ring is inclined with respect
to the detector plane. This is illustrated here for the worst case near 45°. The
image is broadened by δ due to the finite absorption length and the rotation of
the focal plane. However these effects are counterbalanced by the elongation of
the ring into an oval, thus keeping $\Delta R/R$ approximately constant. In addition,
the image suffers a parallax error (ϵ) due to the incident angle. Measurement of
the conversion depth (third coordinate) removes this error.
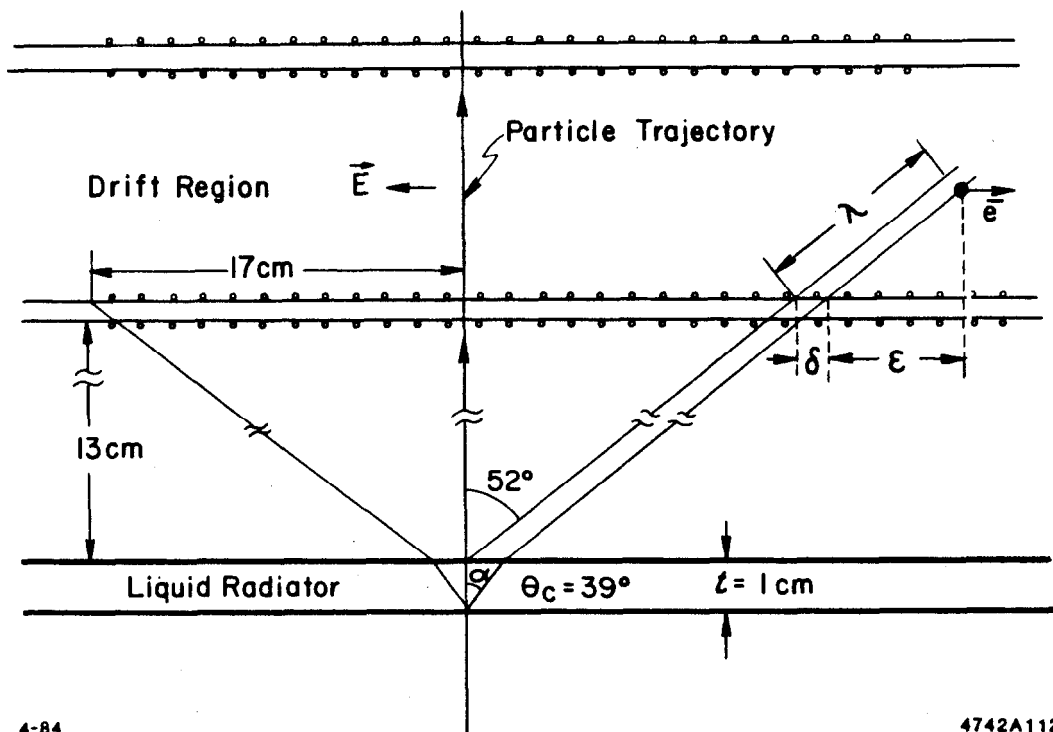
Figure 6.14.   Schematic representation of liquid radiator optical arrangements.

90° region. In the 90° and 0° degree regions the proximity-focused Čerenkov light forms a circular image in the detector box. The proximity-focused image has an inherent width (δ) due to the thickness (t) of the radiator. In addition, the large Čerenkov angle (39°) and refraction angle (52°) coupled with the finite absorption length ($\lambda \simeq 12$ mm) results in a parallax broadening (ϵ). The depth (third coordinate) measurement removes this contribution to the ring width.

Figure 6.15. Schematic representation of liquid radiator optical arrangements.
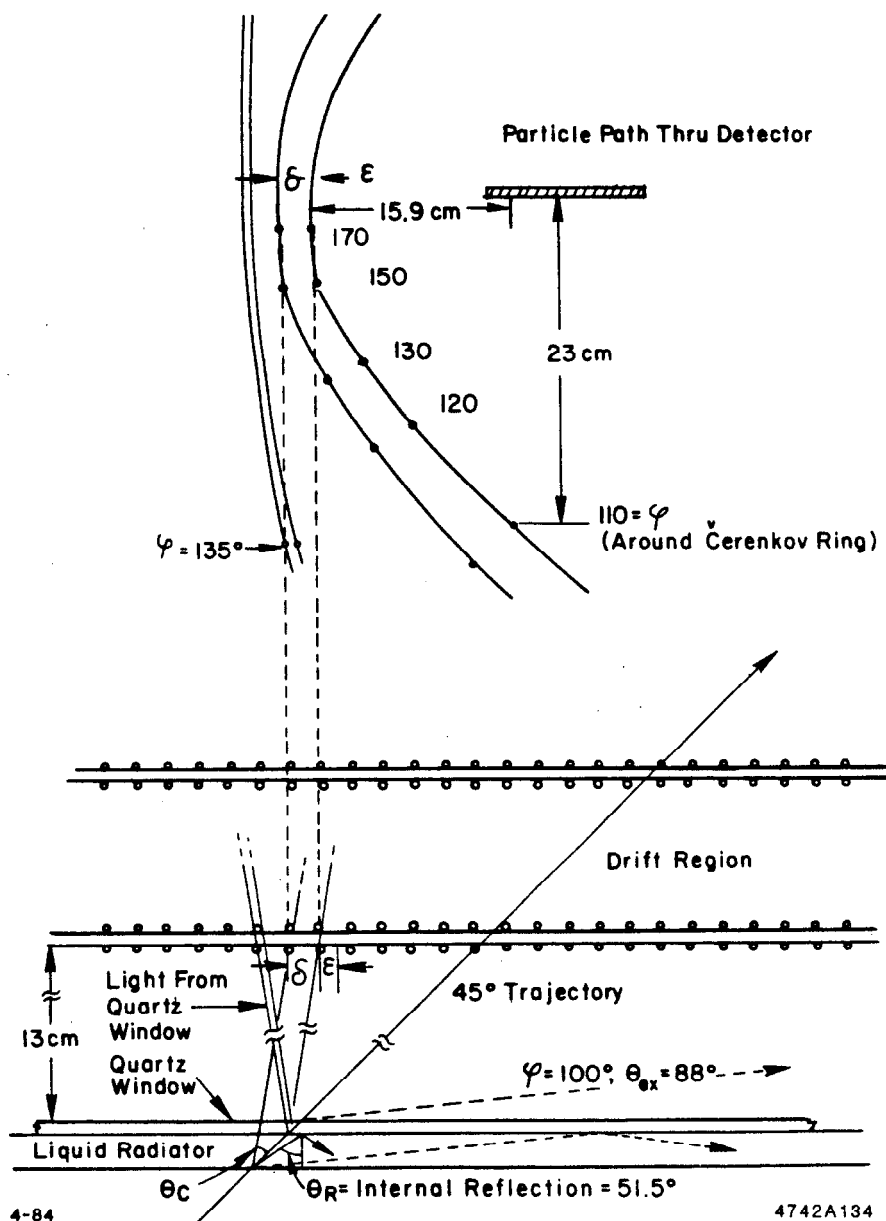
45° region. For track angles less than 77°, part of the Čerenkov light is internally reflected. At 45° more than half of the ring is lost to internal reflection. This results in a crescent shaped image with legs tailing off to infinity. The width of the image (δ) due to the radiator thickness (t) is increased due to the increased length of the trajectory through the radiator. The number of photons is also increased. The parallax broadening is reduced on the back portion of the crescent. The long lever arm of photons detected on the crescent legs decreases the error on the Čerenkov angle. The combination of these effects results in an approximately constant error on the Čerenkov angle over the entire detector.

Figure 6.16.   Engineering detail of barrel and endcap in a longitudinal layout.

6 - 27

Figure 6.17. Engineering detail of barrel: cross section.

mid-plane and ends of the cylinder and provide: (1) mechanical strength, (2) a support structure for attaching the internal components, and (3) an O-ring surface for sealing the ends. The end rings are 80 mm deep radially and contain all the liquid, gas, electric, and electronic feedthroughs. A number of spokes and struts tie the inner and outer cylinders together. The spokes are made of aluminum sheet metal with a 90° fol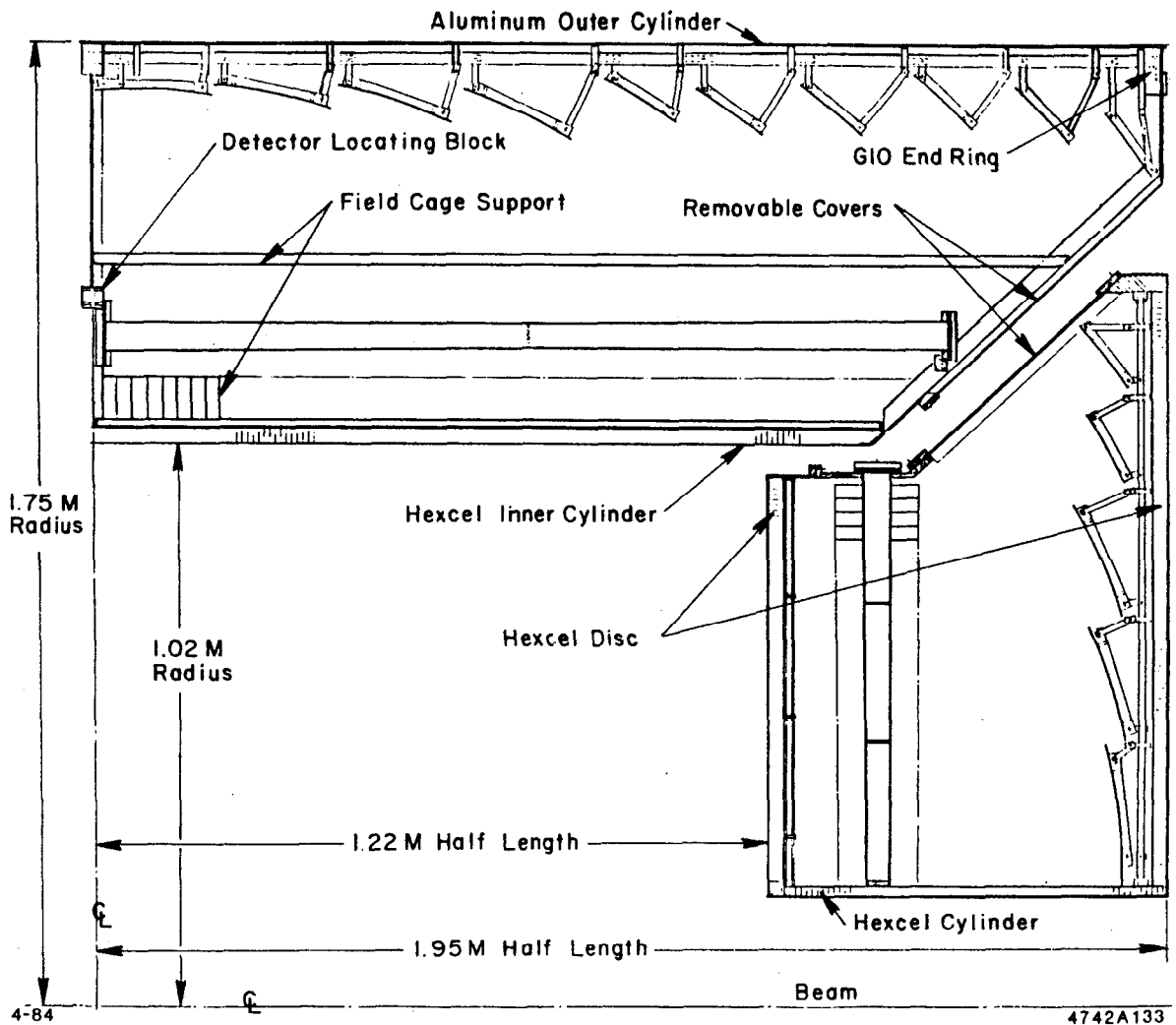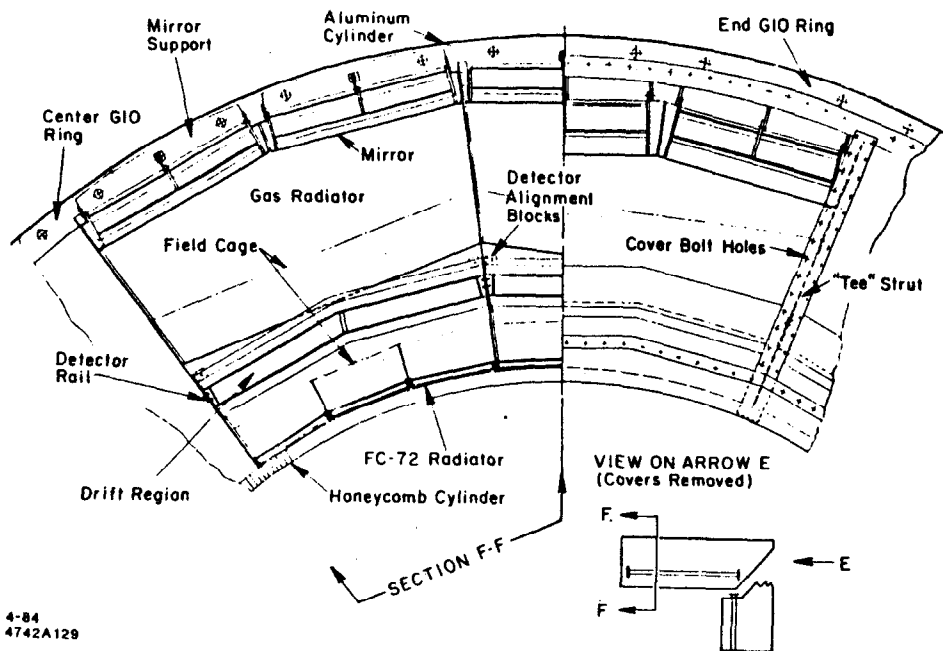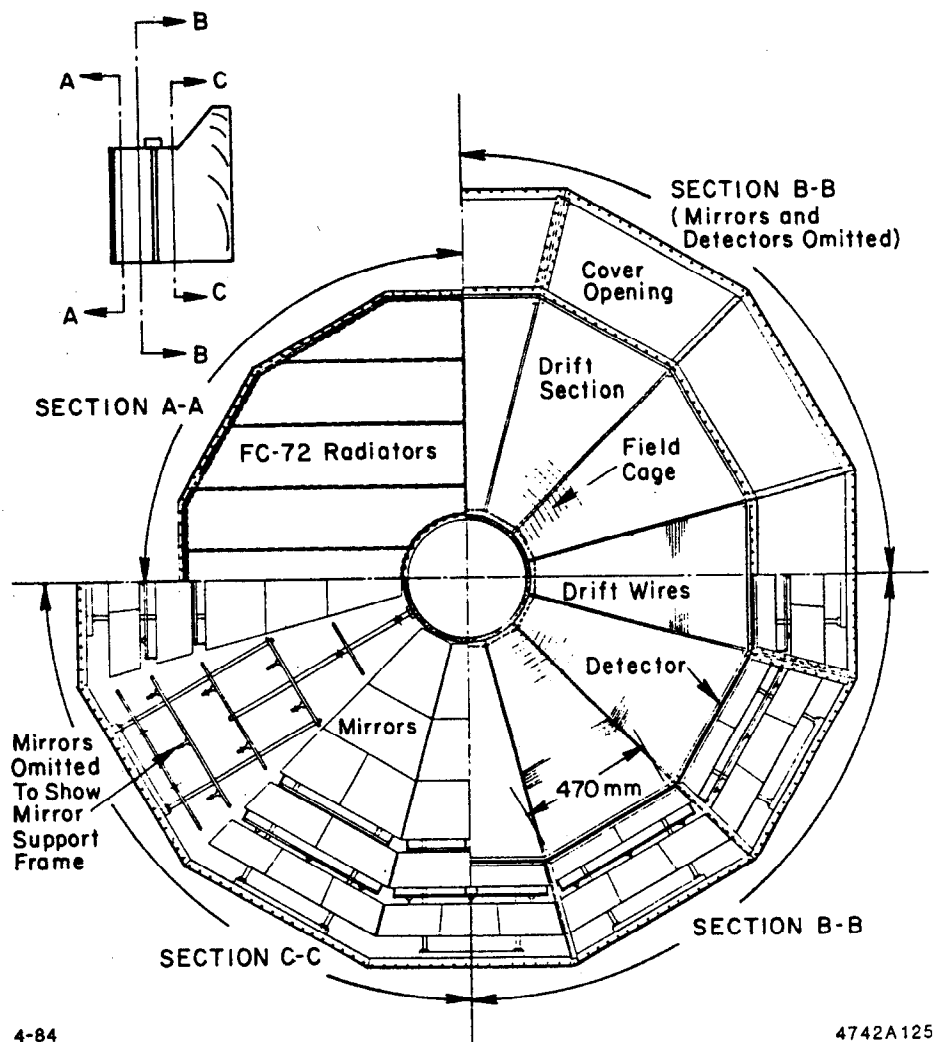d at one edge to provide strength. At the mid-plane the spokes are radial; at the ends they are approximately along radii at a polar angle of about 50°. At the ends four of the twelve spokes are replaced by 'tee' struts. These struts divide the endplate into quarter panels which can be individually removed for access. Three sets of double detector boxes are accessed through each quarter panel. The pie shaped panels are made of thin aluminum sheets edged with a 5-mm-thick by 25-mm-wide sealing surface for the O-rings.

The Endcap Vessel

The endcap vessel consists of two hexcell disks with 200-mm-radii holes at the center. The disks are joined at the inner radius by a 200-mm-radius hexcell tube which is 2 cm thick. At the outer radii there are structural rings attached to the disks. The two disks are connected at the outer radii by tee struts between the two rings. The struts and rings provide a surface for sealing the cover panels. There are four panels which together form the conical section of the endcap. Access to the detectors, mirrors, and liquid radiators is through the panels. Plumbing and electrical connections are through the structural rings. The endcap vessel engineering details are shown in Figure 6.18.

The endcap drift box is a 12-sided polygon (dodecagon) with the 12 detector MWPCs at the periphery. This disk shaped structure is mounted on the 200-mm-radius hexcell tube at the center. Structural hexcell disks fasten to each end of this central tube. The liquid radiator cells are mounted on the inner disk and the mirror array on the outer disk. The outer radius of the outer disk is joined to the detector box by struts and closed with access panels. The inner disk, which can be removed with the liquid radiator cells attached, is bolted at its rim to a flange that is part of the detector structure.

SECTION B-B
(Mirrors and
Detectors Omitted)

Cover
Opening

Drift
Section

Field
Cage

SECTION A-A

FC-72 Radiators

Drift Wires

Detector

Mirrors
Omitted
To Show
Mirror
Support
Frame

Mirrors

470 mm

SECTION B-B

SECTION C-C

4-84

4742A125

Figure 6.18. Engineering detail of endcap.

Cable and Fluid Plumbing Access

The 6000 twisted pairs from each end of the central tracker will pass through the 5° conical channel that separates the barrel and endcap regions. The *CRID* itself has a total of 32,800 twisted pairs. The wires from the detectors at the mid-plane of the detector will be brought radially outward along the support struts at the mid-plane where they will not interfere with optical paths from the mirrors. They will then be brought to the end of the barrel region behind the mirror arrays. From the ends of the barrels and endcap detectors, the cables can easily be brought up the 5° conical channel. Gas and liquids will be brought down the 5° channel for easy access to fittings in that region.

6.2.2 Čerenkov Radiators

Liquid Radiator

The liquid radiator consists of a uniform 10 mm layer of *FC-72* covering the inner surfaces of the *CRID* vessels as completely as possible. The liquid is contained in long flat 'cells' with *UV* quartz windows facing the photon detector. The size of the cells is a compromise between the conflicting desires of minimizing the area lost to cracks, making the windows as thin as possible (to reduce background photons as well as cost) and withstanding the hydrostatic pressure of the liquid. In addition the great affinity of *FC-72* for absorbing gases (especially oxygen) requires that the liquid be continuously circulated through a purification system discussed in Section 6.2.4.

The liquid container system is divided into individual cells and into isolated hydrostatic levels. The cells are made entirely of quartz. The window is *UV*-grade fused silica; the walls and back panel are inexpensive, commercial grade quartz. The seams of the cells are fused together and are therefore gas tight. At one end there are inlet and outlet tubes for filling and circulation. The cell width is determined by the maximum hydrostatic pressure allowed by an unsupported 3-mm quartz window. The current plan has 36 cells of 180-mm width around the barrel, making 18 separate liquid levels [see Figure 6.24]. There are 14 liquid levels in the endcap. The barrel cells are divided at the mid-plane and are 1430 mm long. In the endcap the cells are placed horizontally and are of varying

length to cover the angular endcap region.

The cells are strong and easy to handle, simplifying installation, removal and cleaning. The fused cell structure minimizes the possibilities of fluid leaks and contamination. Also, the area lost to cracks is minimized because the walls are thin (2 mm).

The barrel cells are half the barrel length. They can be installed or removed individually. At the mid-plane they are captured by a retainer lip on the structural ring of the inner wall of the barrel. At the outer end they are retained by a flange that fastens in place after the cell is installed. Along the length there are thin posts between the cells that support the high voltage field cage. Retainer rings clip to these posts and provide support for the cell.

The Gas Radiator

The gas radiator fills the entire volume of the barrel and endcap vessel, including the region between the liquid radiator and the photon detector. The Čerenkov light produced in this region will be 25% of that produced in the area between the detector and the mirrors. The non-imaged photoelectrons will be less than 7.5 mm from the ionizing track in the detector and most of them will merge with it, whereas the imaged photoelectrons will typically appear 2.8 cms from the particle track.

6.2.3   Photon Detectors

To minimize the number of electronic channels implied by the three-dimensional space point measurements required, the long-drift time-projection technique has been adopted. This technique is well matched to the SLC time structure; during the period between pulses the photoelectron images can be drifted over a long distance with a low drift velocity. This makes it feasible to digitize one time and two space coordinates for large densities and multiplicities of tracks with relatively modest electronics.

Drift Boxes

In each half-barrel there are 24 photon detector boxes, 1560 mm long by 300 mm wide and 40 mm deep. The boxes are paired azimuthally in chevrons joined

at a 15° angle to minimize acceptance losses, to insure complete gas circulation, and to provide mechanical strength. Thus there are 12 chevrons around the barrel and two along the length making 24 separate units. To reduce the maximum drift length and keep the voltage to a moderate value (< 35 kV) the boxes are electrically divided, with the maximum voltage electrodes at the middle and *MWPC* detectors at each end. The most negative potential is at the one-quarter and three-quarter points along the staves. Electrons drift away from these points toward the mid-plane or toward the ends. (See Section 6.2.3 for details on the electrostatics).

Each of the two endcap drift boxes is a single dodecagon with a 400 mm diameter hole at the center. There are no inner walls between sectors of the dodecagon so that electrons can drift from one sector to the next. There are two metal support posts at each sector interface. The field-shaping electrodes are concentric 12 sided rings grading the drift voltage uniformly from the inner radius out to the periphery where the detector *MWPCs* are located.

Photoelectron Detection

After photoelectrons have drifted to the ends of the drift boxes, they are amplified by the multi-wire proportional chamber 'picket fence' before being further amplified electronically so that their arrival time and amplitude can be digitized. The combination of 70% methane and 30% isobutane provides sufficient gain when combined with a low noise hybrid preamplifier. A standard *MWPC* picket fence with 20 μm wires, filled with this gas mixture, would be sufficient if it were possible to read out only the photoelectrons. However, the picket fence will also amplify the large dE/dx ionization loss from a charged particle passing through the 40-mm-thick drift box. Up to several hundred primary electrons will also undergo the gas gain seen by single photoelectrons at the picket fence. It is well known that proportional avalanches create ultraviolet light around the wire; however, it is usually absorbed by one or more of the component gases (e.g., freon in magic gas). In a photosensitive gas detector *UV*-absorbing gas cannot be used unless it is photo-ionizing. The photo-ionizing *TMAE* vapor has a long absorption length of 12 mm, so some avalanche photons are converted several

centimeters away at neighboring wires or back in the drift region, resulting in a feedback mechanism.

Inhibiting this feedback can be accomplished by placing opaque, vertical blinds between wires of the picket fence. These blinds can also be useful if made out of thin printed circuit board material to control the electric field around each amplifying wire, improving the gain and stability of the structure. The tall blinds prevent avalanche photons from feeding neighboring wires.

The photon detector for one drift tube will consist of one picket fence of 100 anode wires on a 2.5-mm pitch with 12-mm-tall G-10 blinds (shown in Figures 6.19(a) and (b)). The anode wire is displaced 2.5 mm from the bottom of the blinded channel. The structure on the back cathode is segmented in eight 5 mm pads for conversion depth information. Since each cathode pad covers eight neighboring wires, the number of cathode and anode electronic channels are equal. The successful operation of photon detectors of this type is discussed below in Section 12.

An alternate device shown in Figure 6.20(a) is being studied for the actual *CRID* device. The key elements are:

1. Separation of the gain mechanism into a low-gain preamplification gap and a low-gain proportional tube;

2. Nearly complete blocking of feedback photons by the tube;

3. Reduced positive ion feedback from the tube into the drift region by the preamplification gap; and

4. Improved spatial resolution along the picket fence as a consequence of the large electron cloud emerging from the preamplification gap which enters one or two neighboring proportional tubes.

Preamplification gaps have been used in recent years, especially for detecting single photons,[8] with high gains in a variety of gases, although here we need only a modest gain of 25 (after transfer gap losses). The electrostatic study shown in Figure 6.20(b) indicates that collection efficiency of charge from the preamplification gap into the split tube is 100%.
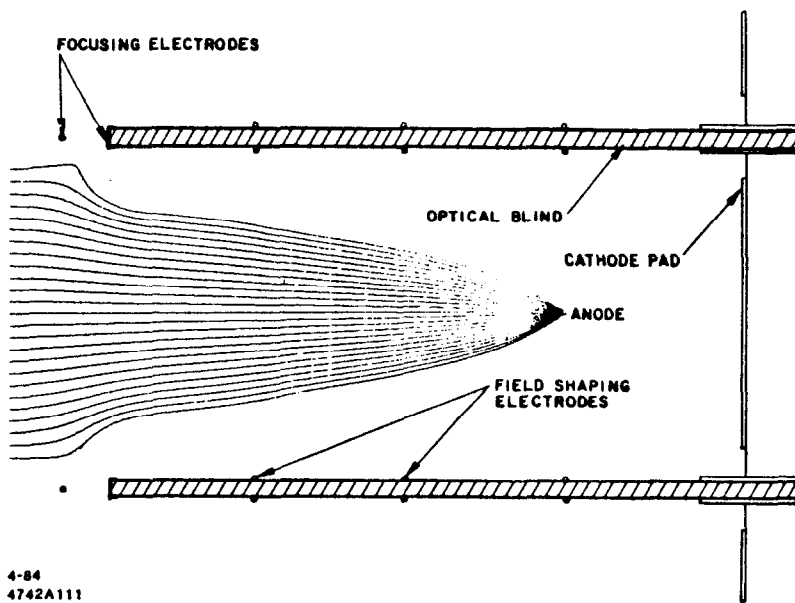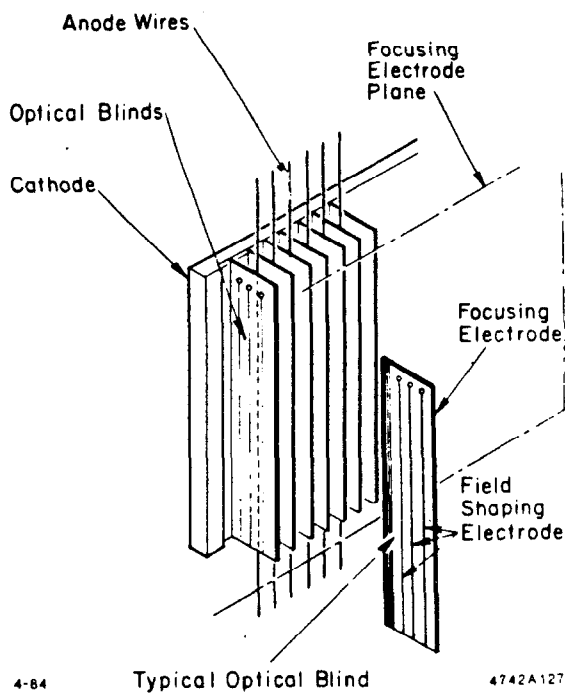
Figure 6.19. (a) A photon detector using graded printed circuit blinds.

(b) Electrostatics of detector shown in Figure 6.19(a).

Amp

Sense Wire

Cathode

40mm

Focusing Grid

Amp

2.5mm

4-84
4742A110

$\eta = .99$ $\eta = .1$

FOCUSING POLE

ANODE

FOCUSING POLE

DRIFT REGION

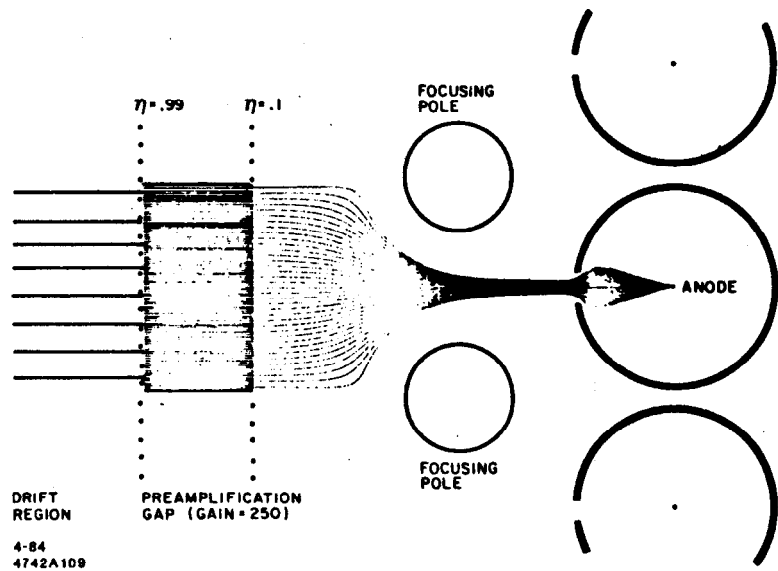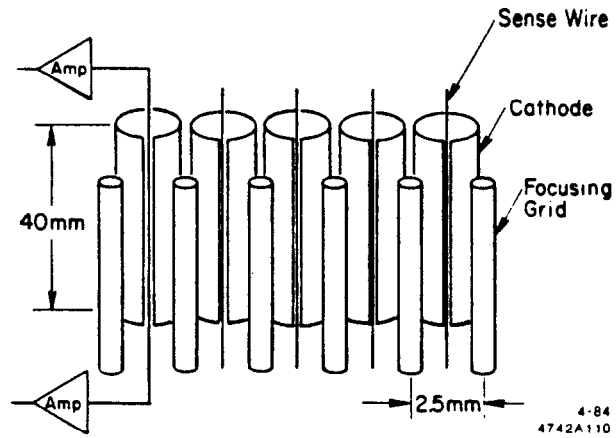PREAMPLIFICATION GAP (GAIN = 250)

4-84
4742A109

Figure 6.20.   (a) A photon detector using slit tubes.

(b) Electrostatics of detector shown in Figure 6.20(a).

6 - 36

Third Coordinate Readout

Because the absorption length in *TMAE* is long (12 mm), the detector must be capable of measuring the conversion depth of the photoelectron. For the liquid proximity focusing, the error on the calculated Čerenkov angle for a single photoelectron is directly related to the uncertainty in the drift length. The radiator thickness sets the fundamental scale of uncertainty. The measurement of the depth should be sufficiently good that it does not add significantly to this drift distance error. In the case of the mirror-focused rings the focal plane is tilted up to 48° and the depth measurement is required to allow the projection into a plane. Since the tangent of 48° is greater than one, this effect sets a rather stringent limit, essentially requiring that the depth measurement be as accurate as the distance measurement from the drift time. Finally, it is very useful to have a reasonable depth measurement to allow the separation of gas and liquid rings at the pattern recognition and fitting stage.

The third coordinate can be read out by using eight cathode strips over the 40 mm wire length. The induced image charge spreads over two 5 mm strips, so that the centroid can be found by interpolation.

The third coordinate can also be determined using charge division along the 4-cm-long anode wire in the picket fence. Others have reported charge division resolution from single photoelectron avalanches of 3.2 mm (2.3%) along 14-cm wires.[9] This alternative is discussed in the Section 6.3.

Electrostatics

The drift boxes in the barrel consist of two back-to-back drift regions which are graded from about 35 kilovolts at the center down to ground at the readout anodes at both ends. The drift boxes are constructed of two 156-cm fused quartz windows separated at the sides by printed circuit boards that hold the windows apart and complete the electrostatic cage around the box. The electric field is kept under strict control with metallic strips every 2.5 mm on the inside and outsides of all sides of the box. In addition, two transparent guard wire cages are spaced 5 and 10 cm from the quartz windows to further isolate the electric field inside the drift box from external ground planes such as the vessel cylinders
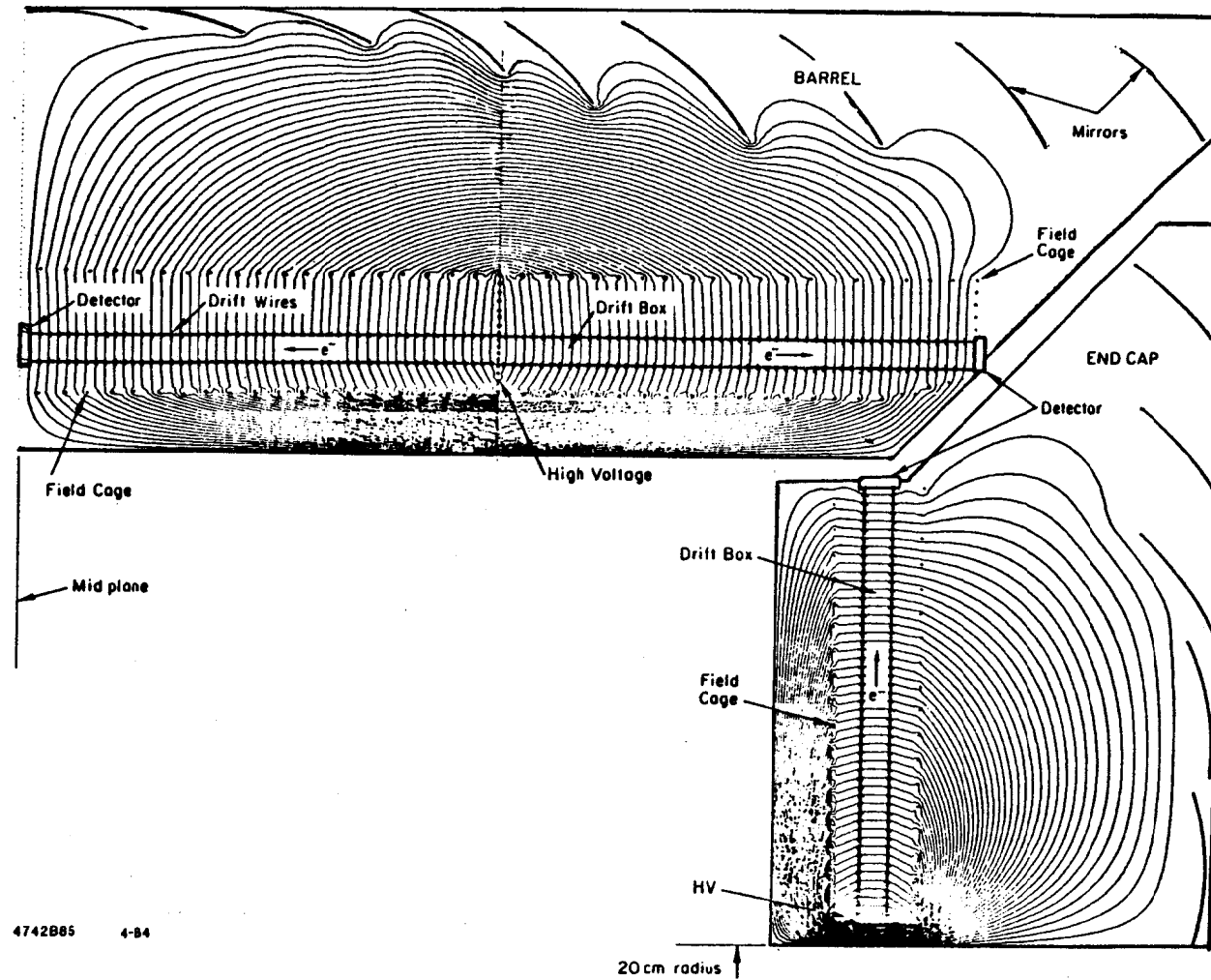
and the mirrors.

Photoelectrons created in the gas of the detector boxes drift in the uniform electric field for up to 80 cm. This requires not only that the gas be free of electronegative elements such as oxygen at the part per million level but also that the electric and magnetic fields be uniform. The mean absorption length of *TMAE* at the operating concentration of 0.1% is about 12 mm. Since the average incidence angle is large, half of all electrons are produced within a few millimeters of the window. Therefore, the magnetic field must be reasonably homogeneous over the volume of the *CRID*; specifically, the integral of the radial component of the field along the barrel drift box should be less than 200 gauss-meters.

An electrostatic field-shaping grid has been designed to insure a drift field inhomogeneity of less than 0.1% over the detector volume in both the barrel and endcap regions. The grid consists of three layers on each side of the drift boxes: grids on the inner and outer surface of the quartz window and an external field cage. The inner and outer grids prevent charge accumulation on the quartz surfaces as well as defining both the magnitude and derivative of the field in the boxes and in the quartz. The external field cage controls the external field shape to minimize inhomogeneities in the drift region.

To allow for slight misalignments and local field irregularities close to the windows, the windows are inclined at 4 mrad to the electric field and open toward the detector end, so that the electrons drift away from the windows at a small angle. The field shape and shielding have been studied using Poisson, and the required mechanical and electrical tolerances are well within the limits of standard components and construction methods.

Figure 6.21 shows the result of an electrostatics study of the barrel and endcap drift regions. Since the voltage is applied far from external walls and structural members, field distortions due to leakage currents are minimized. The moderate high voltage does not have corona problems. The maximum drift distance is one-quarter of the barrel length so electron diffusion will be less than 1.4 mm.

The endcap photon detector is a twelve-sided box with a radial electric field

BARREL

Mirrors

Field Cage

END CAP

Detector

Drift Wires

Drift Box

e^-

e^-

Detector

High Voltage

Field Cage

Mid plane

Drift Box

Field Cage

e^-

HV

20 cm radius

4742B85   4-84

Figure 6.21.   Electrostatics study of barrel and endcap regions.
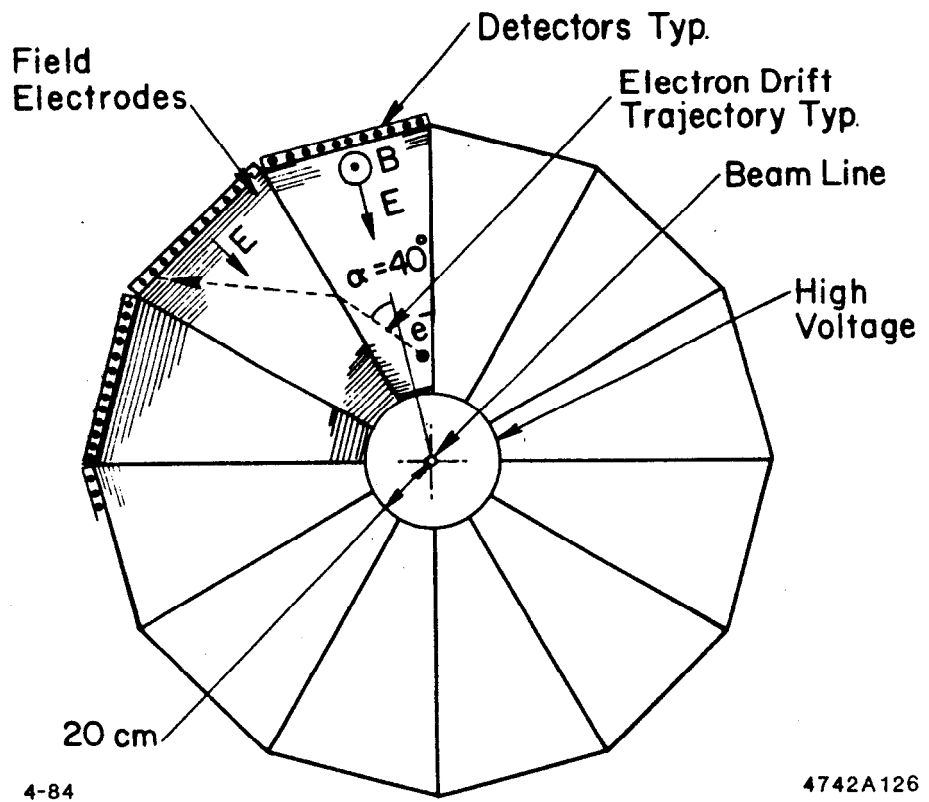
DODECAGON ENDCAP DETECTOR

Figure 6.22. Endcap photoelectron drift spiral.

along the center line of each sector as shown in Figure 6.22. The electrons drift outward at an angle α to the electric field. The field grid arrangement is similar to that in the barrel with three grids on each side; the grids bend 30° at each sector interface. The endcap drift boxes have a special problem created by the Lorentz force. An electron with a drift velocity of 5 cm/μsec in an electric field of 1000 V/cm and in a magnetic field of 10 kG drifts at an angle of 40° with respect to the electric field. As the electron moves radially outward, it also moves azimuthally as shown in a typical trajectory in Figure 6.22. For the *SLD* endcap *CRID*, the photon detector is a large disc-shaped enclosure with no dividing walls; a photoelectron can drift between the twelve sectors shown in Figure 6.22. When the electron comes to the edge of a sector it passes into the next sector. Since there are no internal walls, it bends 30° as it passes through the boundary and continues at the Lorentz angle α with respect to the new electric field, out to the picket fence detector. The quartz disks are not flat, but flare out at 4 mrad to move electrons away from the window surface.

Inventory of Materials

Tables 6.4 and 6.5 show the thicknesses of materials in centimeters and radiation lengths that a particle traverses in the barrel and endcap *CRID* devices.

6.2.4 Fluid Control and Delivery System

The Gas System

The *CRID* gas system is composed of two parts:

(a) a gas radiator volume of about 27,000 liters of isobutane within which exists an optical focusing system of mirrors that focuses Čerenkov light onto the long drift box detectors, and

(b) a number of long drift detector boxes containing the detector gas of methane (70%), isobutane (30%) and *TMAE* (0.1%).

The boundaries between the two systems are 3-mm-thick quartz windows approximately 300 mm by 1500 mm in area (barrel region). The differential pressure between these two volumes must be accurately monitored and controlled to less than 0.1 inch of water. This requirement must prevail during startup, purge,

and power failure, as well as during stable system operation. An intrinsically safe control and delivery system that will insure the integrity of the system in all of

Table 6.4

Barrel *CRID* Material

Component	Material	Position in Radius	Thickness	
		m	mm	$10^{-3} X_0$
Inner Cylinder	Aluminum-Clad Hexcell	1.02	30.0	6
Liquid-Radiator Cell	Quartz/Freon/Quartz	1.05	16.0	85
Drift Box	Quartz/Gas/Quartz	1.20	50.0	36
Mirror	Glass	1.65	3.0	18
Outer Cylinder	Aluminum	1.75	3.2	36
Total				181

Table 6.5

Endcap *CRID* Material

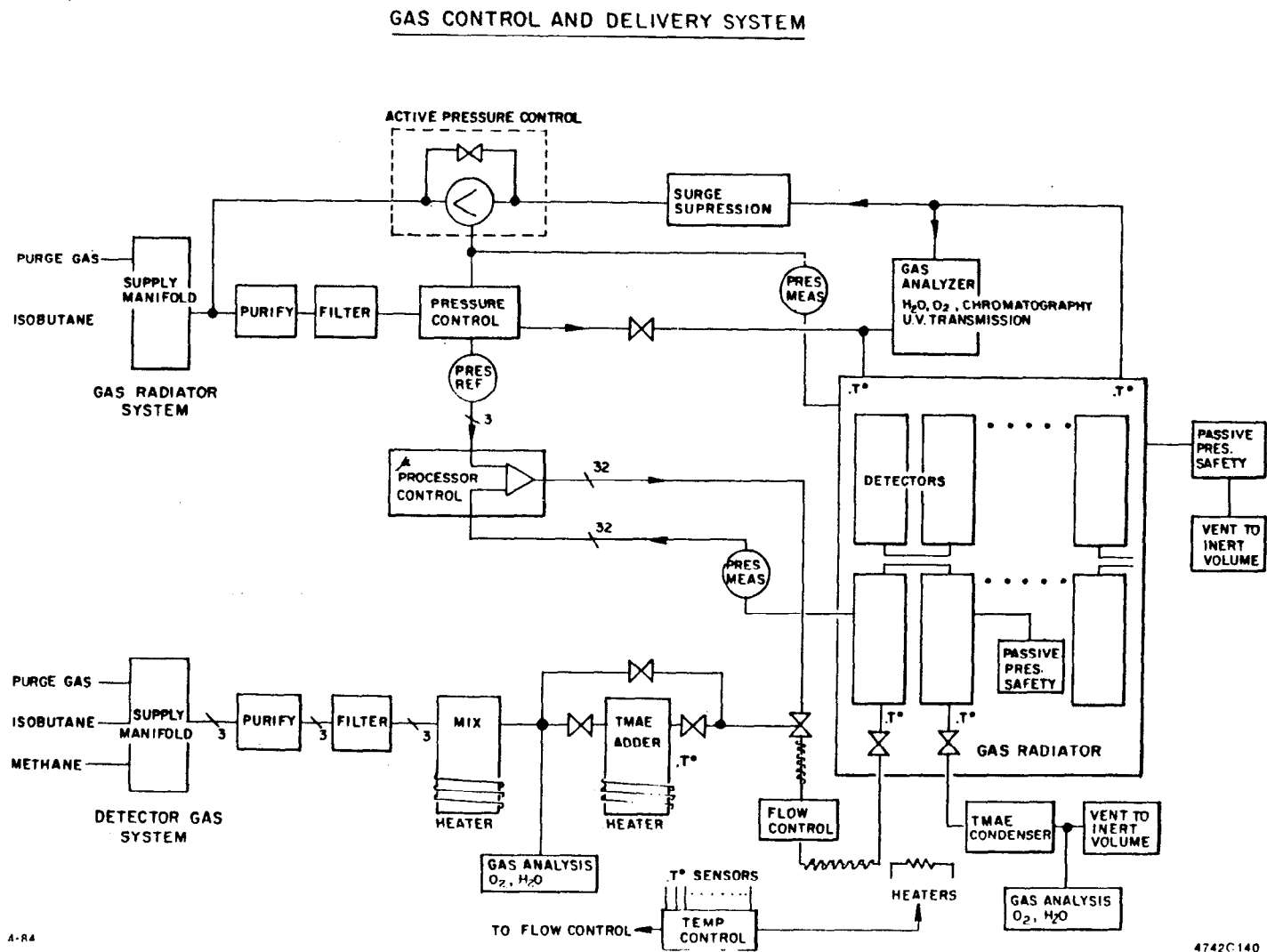| Component	Material	Longitudinal Position	Thickness	
		m	mm	$10^{-3} X_0$
Inner Cylinder	Aluminum-Clad Hexcell	1.22	30.0	6
Liquid-Radiator Cell	Quartz/Freon/Quartz	1.25	16.0	85
Drift Box	Quartz/Gas/Quartz	1.40	50.0	36
Mirror	Glass	1.85	3.0	18
Outer Cylinder	Aluminum	1.95	3.2	6
Total				145

Figure 6.23. Gas system block diagram.

the above cases is shown in Figure 6.23.

The gas system temperature will be elevated above room temperature so that *TMAE* will remain in the proper vapor concentration. The *TMAE* will enter the system at approximately 28°C corresponding to a vapor pressure of 0.75 Torr. The detector volume and the gas radiator volume will be maintained at a temperature of about 35°C to insure that the *TMAE* does not condense within the detector volume. Temperature control and monitoring of better than 1°C are necessary to insure proper performance.

The 35°C temperature required by the detectors will be maintained by pre-heating gases, preheating the liquid radiator, and heaters placed behind the mirror arrays.

Gas purity must be controlled and monitored:

(a) the gas radiator must remain transparent to *UV* photons whose wave length is as low as 1700 Å, and

(b) the detector gas must be free of oxygen and water vapor so that an electron can drift up to 1 meter with a high probability of reaching the photoelectron detector.

The Gas Radiator Volume

The gas radiator system will consist of separate systems for the barrel and two endcaps. Each gas radiator volume will have its own pressure, temperature, purification and flow control system. Since the gas radiator system is the largest and most stable of the systems, it will act as an absolute pressure reference for the detector gas systems. The liquid radiator cells withstand larger pressure differentials than can be allowed in the gas system, and hence will not be coupled to it. The gas will recirculate with a flow rate capable of changing the entire volume once an hour. After purification, the isobutane will be held to less than 20 ppm oxygen, and will be constantly monitored and analyzed as to purity and *UV* transparency. The temperature and pressure will be measured at various points within the common volumes, and the signals transmitted to a microprocessor-based control system.

The Detector Volume

The detector volume contains a mixture of methane, isobutane and *TMAE*. The mixture will be distributed in a non-recirculating system. Input gases are purified and then mixed in a preheated mixing volume; the mixed gases then pass through a heated bubbler, whose temperature determines the *TMAE* concentration in the detector gas. Signals from temperature and pressure transducers in both the reference (radiator) and detector gases determine the flow of gas to the detector system in order to maintain a constant pressure differential and constant temperature. The used gas is passed through a condenser to remove the *TMAE* and then vented to a reservoir for safety. The detector gas is monitored for oxygen and water vapor contamination before the addition of *TMAE* and after the removal of *TMAE* at the output. Contamination levels will be kept to less than 2 ppm.

Pressures and temperatures throughout the system will be measured using solid state transducers. A microcomputer will control the system with a failsafe algorithm to avoid critical problems such as pressure buildup on the vessels or quartz windows, or *TMAE* condensation in the detectors due to a temperature drop.

As accidents tend to occur more frequently during startup and power failures, passive pressure and temperature controls will be used to protect against over pressure and reduced temperature conditions. Commercial differential pressure measuring and control devices have been used on similar applications to maintain pressure differences of less than 0.1 inch of water. Commercial filters, molecular sieves, and hydro purifiers such as Oxisorb will be used to maintain the gases free of oxygen and water vapor.
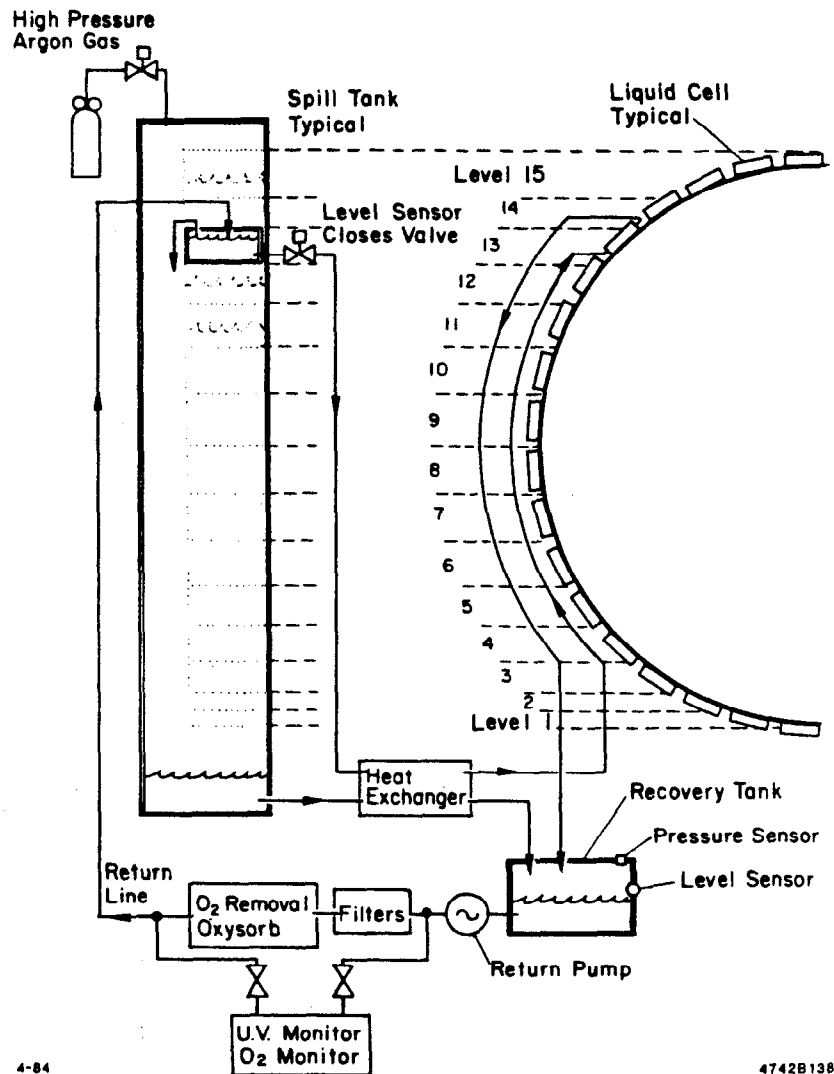
Reliability

This large gas system must run reliably for years. The system will include rugged control components, redundancy in the monitoring and control circuits, doubling of the critical components of the system such as pumps and purifiers for periodic maintenance, and automatic monitors and controls with easy-to-understand diagnostics.

The Liquid System

The liquid circulation system must remove oxygen, water-vapor and other contaminants from the FC-72 to insure the highest UV transmission. FC-72 has a high affinity for oxygen and other gases. Oxygen and water-vapor are particularly troublesome because of their presence in the environment and because they strongly absorb UV below 1800 Å. Oxygen and other gases can be removed by commercially available Oxisorb fitters. Other methods are also under investigation. Nitrogen is transparent in the UV and other gases are not abundant in the environment. The liquid radiator will be periodically degassed and purified in a continuous circulation system capable of replacing the entire 300-liter volume every hour.

Spill Tank Circulation System

The liquid circulation system that will control all pressures in a common system is shown in Figure 6.24. The liquid radiator system is divided into a number of levels determined by the maximum pressure an individual cell can withstand. At each level the hydrostatic pressure is controlled by a reservoir filled to the same depth as the liquid in the cells and placed at the same height. A fill line connects the bottom of this reservoir to the bottom of the lowest cell of that level. A return line from the top of the highest cell of that level returns the cell overflow to a common recovery tank. The pressure in the reservoir is controlled by spilling over the reservoir wall. Reservoirs for all levels are in a common pressure tank filled with argon gas. A small over pressure, δP, causes liquid to flow in all levels. The liquid in the recovery tank is pumped through the filtration and degassification plant and returned to the reservoirs. A pressure release valve on the pressure tank prevents an excessive pressure that could break a quartz cell. Gas released by the overpressure valve is passed through a condenser to recover the FC-72 vapor. This passive circulation system is virtually failsafe. If the recovery pump fails, the circulation simply stops when the level in the reservoirs drops by δP. Level sensors are installed in the reservoirs to detect a leak in an individual level; a solenoid shuts off flow in the event the liquid level drops too low.

High Pressure
Argon Gas

Spill Tank
Typical

Liquid Cell
Typical

Level 15

Level Sensor
Closes Valve

14
13
12
11
10
9
8
7
6
5
4
3
2
Level 1

Heat
Exchanger

Recovery Tank

Pressure Sensor

Level Sensor

Return
Line

O₂ Removal
Oxysorb

Filters

Return Pump

U.V. Monitor
O₂ Monitor

4-84

4742B138

Figure 6.24. Liquid circulation spill tank system.

6 - 47

<u>Monitors</u>

(a) Gas Transparency

The *UV* transparency is monitored using a system shown schematically in Figure 6.25. An *RCA* Quanticon allows phototube gain calibration using the single photoelectron spectrum of the tube itself. The gas transmission monitor cycles through a sequence which includes the sample gas, vacuum, calibration gas, vacuum, etc. A mechanical shutter allows the measurement of the single photoelectron spectrum.

(b) Index of Refraction

The index of refraction of both the gas and liquid radiator will be measured at a wavelength of 1700 Å.

(c) Electron Drift Velocity

The drift velocity of an electron in the system will be monitored continuously in the detector gas system.

(d) Gas Purity

A fine-resolution mass spectrometer will be used for startup and trouble shooting.

(e) Liquid Transparency

Continuous monitoring of the transmission at around 1700 Å is planned using the same type of apparatus that monitors the gas radiator. In addition, oxygen levels will be monitored using a device sensitive at the parts per million level.

6.2.5 Alignment and Calibration

The coordinates of the photoelectrons in the drift tubes must be measured relative to the central tracker and the mirror arrays without systematic errors. Errors can occur by: (1) misalignment of the photon detectors azimuthally, (2) drift velocity changes due to voltage or gas mixture changes, (3) electrostatic distortions, and (4) mirror tilt errors. The errors (1), (2), (3) between the central tracker and the drift tubes can be removed by requiring self consistency in the
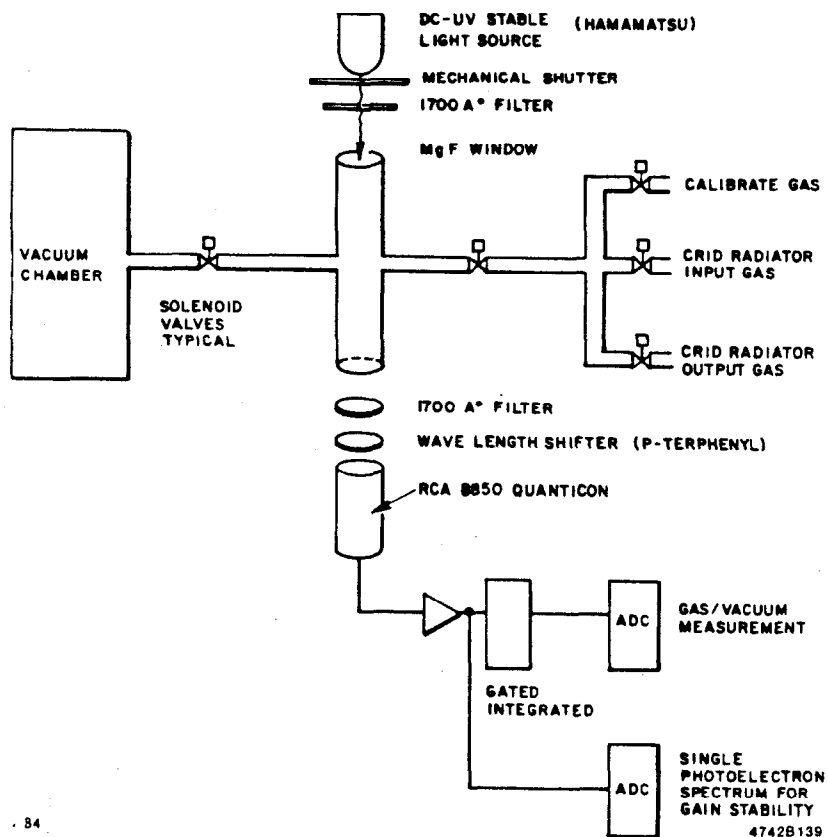
Figure 6.25. Gas *UV* transmission monitor schematic.

tracker-*CRID* data since the particle track is measured both in the tracker and in the *CRID*. The *CRID* also has pulse height information which will make it easy to discriminate the particle track in the drift tube from the single photoelectrons.

The drift velocity can vary with the field voltage, the gas mixture, pressure, and the gas contamination by oxygen. Although these things will be monitored by external systems described in the previous section, a calibration scheme internal to the detector has also been devised to make direct drift velocity measurements in each drift section. Flash lamps are mounted at a few places between mirrors and at the mirror plane to illuminate a mask placed near the end of each drift box. Small masks can be placed at known distances from the picket fence at several places in the gas radiator without obscuring mirror image areas. Flashing the lamps periodically will provide an image of the mask which can be used to check the drift velocity variations from all sources.

The mirror arrays must be aligned during assembly to allow optical ray tracing from the particle trajectory to the image plane to an accuracy of $\frac{1}{2}$ milliradian. In the barrel region an array of ten mirrors will be mounted using three point adjustable supports on two 2-cm thin-wall stainless steel tubes that serve as an optical bench for the array. The two tubes are mounted on the fiberglass rings at the center and two ends of the barrel vessel. The mirrors will first be aligned in an optical laboratory using a fixture that holds the two tubes in the same orientation as their final position in the barrel. The optic axis of each mirror is adjusted to pass through a simulated detector plane at the proper point relative to the optic axes of the other mirrors. Later, the prealigned array of mirrors can be installed in the barrel support system with this alignment preserved. The endcap mirrors will be aligned and mounted in a similar fashion.

6.2.6 CRID System Assembly

The *CRID* system will undergo its final assembly in the interaction region staging area. The barrel hexcell cylinder, the endcap hexcell disks, the outer barrel, aluminum cylinders, the chevron drift boxes, mirror arrays, etc. will be manufactured in shops or laboratories and prealigned and leak checked, where necessary.

The assembly proceeds as follows:

1. Barrel *CRID* assembly

    (a) Install hexcell inner cylinder on temporary fixture.

    (b) Install outer aluminum cylinder around hexcell cylinder with temporary supports.

    (c) Attach and align G-10 rings to outer cylinder.

    (d) Mount L- and T-struts between hexcell inner cylinder and G-10 rings.

    (e) Build a temporary clean room around the vessel and wash the vessel with suitable solvents in preparation for mounting of *UV* optical components.

    (f) Align drift section supports.

    (g) Install liquid radiator cells and plumbing.

    (h) Install inner electrostatic field cage.

    (i) Install prealigned mirror arrays on outer G-10 rings. Check mirror alignment at drift box plane.

    (j) Install drift sections and cabling.

    (k) Install outer field cage.

    (l) Complete gas/liquid distribution feed-through panels.

    (m) Install barrel end covers.

    (n) Leak check gas radiator volume.

    (o) Move barrel *CRID* into magnet.

2. Endcap *CRID* assembly

    (a) Install hexcell disk on dummy beam pipe.

    (b) Install prewired and preassembled 12-sided drift box.

    (c) Leak check drift box.

    (d) Install inner and outer field cages.

    (e) Assemble frame struts to hexcell disk and drift box support.

(f) Position and align mirror support blocks.

(g) Install prealigned mirror arrays-check alignment at detector plane.

(h) Install radiator cells on hexcell disk, connect plumbing, leak check radiators.

(i) Complete gas/liquid system distribution feed-through panels.

(j) Install endcap side covers.

(k) Leak check gas radiator volume.

(l) Install in magnet endcap.

6.3 ELECTRONICS

Specifications

In Section 6.2.3 two methods of readout for the third (depth) coordinate of the photoelectrons were discussed: cathode pad readout of the induced charge and charge division readout of the anode wire. The choice of method to be implemented for the *SLD CRID* will depend on the results of the current research and development program. A program for evaluation of cathode pads, wedge and strip cathodes, and current division in various mechanical configurations is under way. For the purposes of evaluating the electronics requirements of the *CRID*, the following discussion assumes that the charge division method will be used.

A single electronic channel of the *CRID* requires a drift time measurement for an 80 cm drift and a charge division measurement to determine the depth coordinate. The required spatial accuracy is ±0.8 mm over the long drift dimension (1 part in 1600) and ±1.4 mm for the depth direction, which is 4 cm long. The maximum drift time is 20 μsec based on gas drift velocity of 4 cm/μsec.

The *CRID* detects single photoelectrons, so the typical input signal is one primary electron. To limit photon feedback along the drift path and along the *PWC* wire, the gas gain is held to a relatively low value, leading to a typical signal at the collecting wire of $5 \times 10^4 \ e^-$, or 8 fC. If one uses a preamplification gap where the effective gain is (*PA* gain $\times$ transfer efficiency in and out) ≈ 25, then the signal from one electron is about 200 fC.
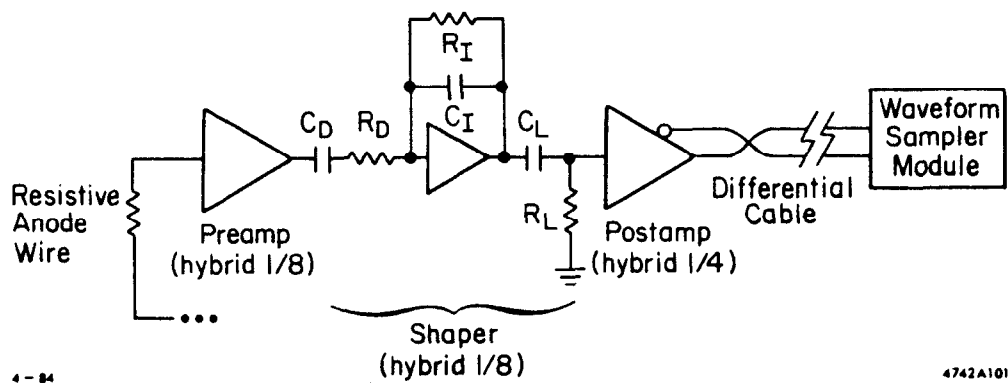
Figure 6.26. Electronic readout channel.

The total number of channels in both the barrel and the endcap regions is 32,800. This assumes 2.5 mm anode wire spacing on the *PWC* detectors and two amplifiers per wire. The basic electronic channel shown in Figure 6.26 consists of a preamplifier, shaper, post amplifier, connecting cable, and a channel of the wave form sampler described in Section 5.2.5.

Preamplification

The typical *CRID* channel signal is extremely small and requires very good signal-to-noise performance to achieve the desired measurement accuracy. Fortunately the drift time is long, so that a relatively slow rise-time (narrow-band) amplifier can be used, which is compatible with this stringent noise requirement.

It will be assumed that the preamplifier is a low input impedance charge sensing amplifier with a gain of $\sim$ 50 mV/pC. The wire to which it is connected will have low source capacitance ($\sim$ 1 pf) and $\sim$ 100 Ω resistance. The amplifier would have about 1000 e^- rms (0.16 fC) noise if its input were connected to a high impedance source. However, since both ends of the wire will be connected to amplifiers, thereby shorting each input to ground through 100 Ω, the input noise will increase to $\sim$ 15,000 e^- rms equivalent or approximately 2 fC. The Johnson noise on a 100 Ω wire at this frequency is $\approx$ 3 fC. Both noise sources together lead to a wire signal-to-noise at either end of the current division wire of about 50:1 assuming a shaping time of $\approx$ 120 nsec.

The 50:1 signal-to-noise is more than sufficient to assure the required accuracy of spatial measurement by current division if the wire resistance is high enough compared with preamplifier input impedances. This is accomplished with a properly designed charge-sensitive amplifier, the input of which appears as a virtual zero impedance. Matching is improved by the use of terminating resistors on each end of the wire in series with the preamplifiers, at very little loss in performance.

The spatial resolution of charge division as a function of position is

$$\frac{\delta X}{L} = \frac{\delta}{i_o} \left\{ 1 - \frac{2X}{L} + \frac{2X^2}{L^2} \right\}^{\frac{1}{2}}$$

where i_o = input signal current

δ = noise current of amplifier

L = wire length

X = fractional position along L.

This shows that the signal-to-noise ratio of 50:1 at the ends of the wire improves to a maximum at the center by $\sqrt{2}$. Ideally the position along the current division wire should be resolvable to $\pm$ 2%, well within the specification.

The time and amplitude readout of the photon detector wires will utilize the same Waveform Sampling Module (*WSM*) described in Section 5.2.5, used by the drift chambers. Since the Analog Memory Unit (*AMU*) of the *WSM* has 256 available time slices, time buckets of 80 nsec width are required to span the 20 μsec maximum drift time. By using 120-nsec pulse shaping in the preamplifier, the pulse will fall into two successive 80-nsec buckets, permitting interpolation of the arrival time to $\frac{1}{6}$ of the bin width, which corresponds to 0.5 mm in drift distance.

Post Amplification

The signal amplitude at the preamplifier output of 10 mV dictates a post amplifier to match the signal range to the data acquisition module *AMU*. Assuming a desired mean signal of 1 volt for the *AMU*, a post-amplifier gain of 100 is indicated. This can be achieved with a μA733 or equivalent device. It is assumed that both the pre- and post-amplifier are mounted as close as possible to the signal source inside the magnetic field for optimum signal-to-noise. It is important that the post-amplifier have a degree of saturation so that minimum ionizing particles having 400 times the ionization are limited to much less than 400 times the signal of a single photoelectron.

Cable Transmission

As in all low-noise systems, a true differential shielded cable transmission system is preferred. In the *CRID* system, the signals are particularly small to begin with, and the overall amplification is high; therefore particular care must be taken with grounding, shielding and isolation. The input connection at the photon detector is single-ended, due to the basic detector construction. The local

preamplifier ground must be made very near the channel's high voltage signal return point. The post-amplifier output will be a differential connection to the data acquisition module at the exterior of the magnet. The proposed design uses multilayer printed circuit transmission cable connected to the edge of the detector and differential shielded cables to the data acquisition modules mounted directly on the detector superstructure.

Data Acquisition Module: Waveform Sampler (WSM)

The data acquisition module described in Section 5.2.5 will serve the identical function for the CRID, with the exception that the write data clock will be slower. The write data cycle is still very fast with respect to the analog memory storage time, so that no change in mode of operation is necessary. A single 256-cell AMU will be used for each channel.

The inherent dynamic range of the AMU is expected to be at least 11 bits, and the ADC will be 12 bits in the WSM design. Signal fluctuations of 10:1 are expected from single photoelectrons in the photon detector. When this is combined with the 50:1 signal-to-noise required for the depth coordinate resolution, it is seen that the 11 bit dynamic range of the WSM is more than adequate.

Miscellaneous Instrumentation

Calibration System

Calibration electronics will be similar to the drift chamber system DAC-controlled pulse generator system with odd/even and segment address capabilities.

High Voltage

The CRID requires one large system supply at 35 kV for each major subsystem, and lower voltages of 2-3 kV for the proportional wires. The high voltage requires overall stability and accuracy of 0.01%. The lower voltages will be derived from standard commercial modular programmable units.

Environmental Control

The CRID must operate at a controlled temperature of 35°C, and a slightly positive pressure controlled to ±0.1 inches of water. Approximately 50 temper-

ature and 150 pressure sensors are required. Film or solid state transducers are preferable. Signal measurement will consist of external conditioning circuits followed by commercial instrument and control modules, operating in a stand-alone, fail-safe configuration, packaged in Camac.

Packaging

The placement of the photoelectron detectors on the mid-plane of the barrel and within the field cage imposes some strict packaging requirements on the electronics. The barrel drift box detectors are 300 mm wide with sense wires every 2.5 mm. Two amplifiers are needed for each sense wire, so that 240 amplifiers are needed adjacent to the detector. The space between the detector and the field cage is 130 mm leaving an average area of 160 mm^2 per channel. This will require hybridization of the preamplifiers, shaper, and post-amplifier. Care in layout must be taken so that amplified output signals do not feed back to the sensitive preamplifier inputs. Shielding, grounding, and power connections will be incorporated within this space as well.

Specification Summary
Preamplifier

1.	Input Signal (single e^-)	= 200 fC
2.	Output Signal (single e^-)	= 10 mV peak
3.	Equiv. Input Noise	= 1000 e^- rms (∞ input impedance)
4.	Equiv. Output Noise	= 0.2 mV
5.	Signal Dynamic Range	= 10:1 nominal
6.	System Dynamic Range	= > 11 bits
7.	Input Cable	= Short stripline to feed-through
8.	Linearity	= $\pm \frac{1}{2}\%$ with calibration
9.	Crosstalk	= $\pm \frac{1}{2}\%$ (electronics only)
10.	Signal Shape	= $f(t) = At^2 e^{-t/t_0}$ (approx.)
11.	Packaging	= 4 channel hybrid mounted close to source
12.	Shaping	= l/t pole cancellation
		$t = 120$ nsec
13.	Output Cable	= Microstrip line

14. Power = 50 mW/ch typ.

15. Environment = 35°C near *CRID*

Post-amplifier

1. Input Signal (typical) = 10 mV peak
2. Output Signal (typical) = 1 V peak
3. Voltage gain (typical) = 100
4. Equiv. Input noise = $< 50\ \mu$V rms
5. Bandwidth (typ.) = 20 MHz
6. Packaging = Hybrid, mounted close to preamplifier
7. Output Cabling = Shielded microstrip line to connector
8. Power (typ.) = 75 mW/ch
9. Environment = Same as preamplifier

Charge Division

Wire Resistance = 100 Ω nominal, 4 cm length

Preamp Input = $<<$ 40 Ω (capacitive)

Required Accuracy = $\pm$3.5% of 4 cm

Data Acquisition Module

Identical to Drift Chamber Unit (See 5.2.5) except single 256 cell *AMU* per channel.

Calibration

See 5.2.5.10

High Voltage

4 35-kV bulk supply at 2 mA, $\pm$0.01% regulation.

40 channels of 2-3 kV standard modules.

Environmental

50 temperature sensors for gas control within 1°C.

150 pressure sensors for gas control within 0.1 inches of water.

Readout packaging: Camac

6.4 PERFORMANCE

6.4.1 Angular Resolution

The particle separation capabilities of the CRID depend on the precision with which the Čerenkov angle is measured, which in turn, depends on the angular precision of each photoelectron measurement and the number of photoelectrons detected. Each photoelectron has an angular error which includes contributions from a variety of sources as discussed in section 6.1.3 and summarized in Table 6.6.

6.4.2 Particle Separation

The particle separation capabilities of the CRID are displayed in Figure 6.27. The vertical scale gives the separation between different kinds of particles in standard deviations and is 'saturated' at 10 σ, since non-Gaussian tails render quantitative estimates of very large separation probabilities unreliable. The 1-cm-thick liquid FC-72 radiator in the CRID should provide an average of 14-23 detected photoelectrons per relativistic particle passing through the counters, depending on the polar angle of the particle. The 50 cm of isobutane gas radiator in the CRID is expected to yield an average of 14 detected photoelectrons per high-energy particle passing through the counter. These photoelectron yields, together with the angular resolutions shown in Table 6.6, result in the excellent particle separations at 90° as shown. At the 3-σ level, e/π separation is achieved up to 7 GeV/c. The π/K separation is above the 3-σ level from 230 MeV/c up to 32 GeV/c, and K/p separation from 800 MeV/c to 55 GeV/c, though, in this case, the separation drops to about the 3-σ level in the region just before gas turnon below 10 GeV/c.

Separation in the gas radiator is essentially independent of polar angle, as can be seen in Figure 6.28(a), which compares the π/K separation at a polar angle of 45° with that at 90°. There is some loss of separation range in the liquid, which is due primarily to the less favorable geometrical arrangement and to the loss of photons from the internal reflection cutoff in the radiator. Taking both radiators together, the π/K separation power is seen to be essentially unaffected by polar angle effects. However, the reduced range in the liquid does lead to a
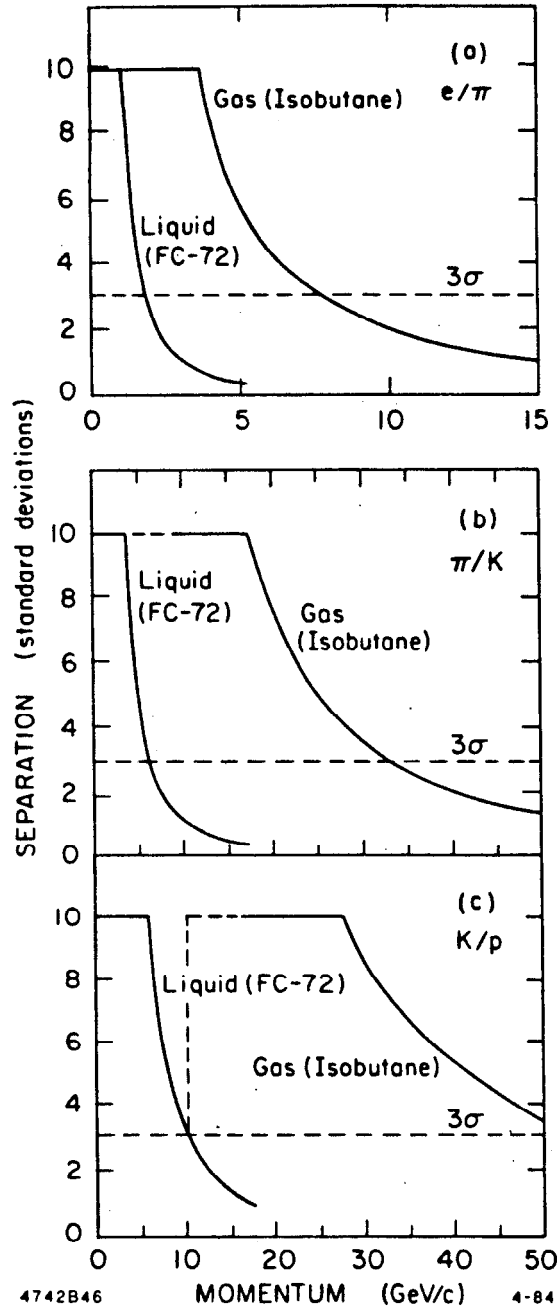
Figure 6.27.   Particle separation capability of the *CRID* system at 90° versus momentum. The performance of the liquid (*FC-72*) and gas (isobutane) radiators are shown separately. The curves are 'saturated' at 10 σ (see text). The dashed line indicates the region where the heavier particle is below radiator threshold. The separation is shown for; (a) e/π, (b) π/K, and (c) K/p.
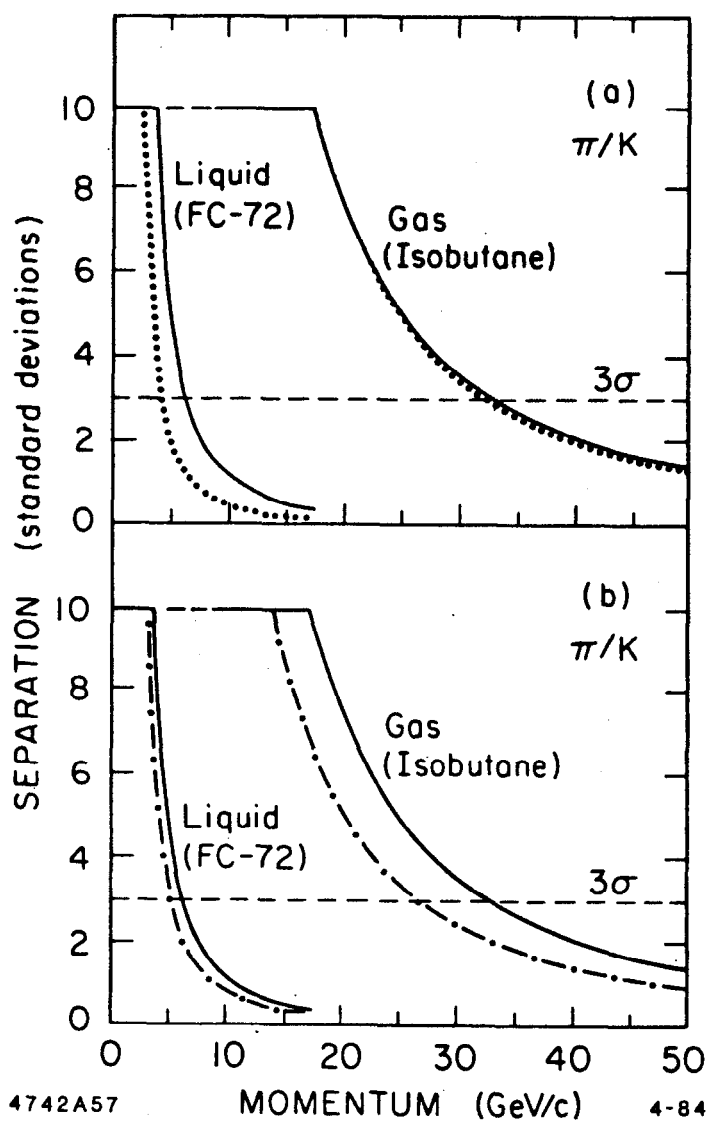
Figure 6.28. The nominal π/K separation of the *CRID* system at 90° (solid line) versus momentum (see Figure 6.27) compared with the performance: (a) at 45° (dotted line), and (b) with the nominal number of photoelectrons divided by two (dotted-dashed line).

6 - 61

Table 6.6

The Contributions to the Angular Resolutions of the Liquid and Gas CRIDs at 90°.

P	θ_C (mrad)	N_{pe}	Geometry	Detector Measurement	Multiple Scattering	Momentum Smearing	Chromatic Aberration	Total	θ_C (mrad)	N_{pe}	Geometry	Detector Measurement	Multiple Scattering	Momentum Smearing	Chromatic Aberration	Total
				GAS — Angular Resolution (mrad)								LIQUID — Angular Resolution (mrad)				
0.5	0								622.2	20.6	5.7	1.9	2.8	1.3	3.3	1.8
1.0	0								660.0	22.8	5.3	1.6	1.4	0.6	3.1	1.5
1.5	0								666.4	23.2	5.2	1.6	0.9	0.4	3.1	1.4
2.0	0								668.8	23.3	5.2	1.5	0.7	0.3	3.1	1.3
3.0	33.2	4.7	0.1	1.7	0.1	10.1	2.8	4.2	670.5	23.4	5.1	1.5	0.4	0.2	3.1	1.3
4.0	45.3	8.8	0.1	1.7	0.1	7.6	1.4	2.5	671.2	23.4	5.1	1.5	0.3	0.2	3.1	1.3
5.0	49.8	10.6	0.1	1.7	0.1	6.1	1.2	1.6	671.4	23.5	5.1	1.5	0.3	0.1	3.1	1.3
10.0	55.4	13.1	0.1	1.7	0.0	3.0	1.1	0.9	671.8	23.5	5.1	1.5	0.1	0.1	3.1	1.3
15.0	56.3	13.6	0.1	1.7	0.0	2.0	1.1	0.8								
20.0	56.7	13.8	0.1	1.7	0.0	1.5	1.1	0.7								
25.0	56.8	13.8	0.1	1.7	0.0	1.3	1.1	0.6								
30.0	56.9	13.9	0.1	1.7	0.0	1.0	1.1	0.6								

gap in K/p separation between about 6.5 and 10 GeV/c where the separation drops below 3 σ.

Good separation is achieved over 98% of the solid angle for the liquid radiator, and for 94% of the full solid angle for the gas system. The difference is mainly due to a dead region of about 5° in polar angle for all azimuths around 40° for cables and gas umbilicals to the inner detectors.

The particle separation performance is robust. If the angular resolution of the detector were worse by a factor of two, for example, then the upper momentum for π/K separation in the gas radiator is only reduced from 32 GeV/c to about 22 GeV/c, and from 6.0 GeV/c to about 3.8 GeV/c in the liquid radiator alone. A similar derating of the resolution in a dE/dx device would result in no satisfactory π/K separation above 1 GeV/c. Furthermore, if the quantum efficiency of the photoelectron detection system should turn out to be only 50% of the advertised value, then the range of particle separation is only slightly reduced. As shown in Figure 6.28(b), π/K separation still occurs at above the 3-σ level over most the *SLC* momentum range. The primary effect is that the 3-σ range moves to 26 GeV/c instead of 32 GeV/c. Similarly, the e/π separation range is up to 6 GeV/c instead of 7 GeV/c, and K/p separation occurs up to 46 GeV/c instead of 55 GeV/c. Soft failure indeed!

6.4.3 Segmentation

The intrinsic segmentation of the *CRID* is about 12 mrad for the gas and 18 mrad for the liquid. Since most particles that remain in the cores of jets at the *CRID* radius are fast, these particles will generally be identified in the gas *CRID*. Therefore, the tagging efficiency should be quite high even for particles within the jet cores. This will be of particular help for the study of electrons associated with hadron jets, where the density of hits will create problems separating particles in the calorimeter.

6.4.4 Pattern Recognition

The hit pattern in the barrel *CRID* is shown in Figure 6.29 for a typical Monte Carlo generated $c\bar{c}$ event. The ovals of approximately 17 cm radius from the liquid rings are clearly visible near the z origin. These ovals quickly become
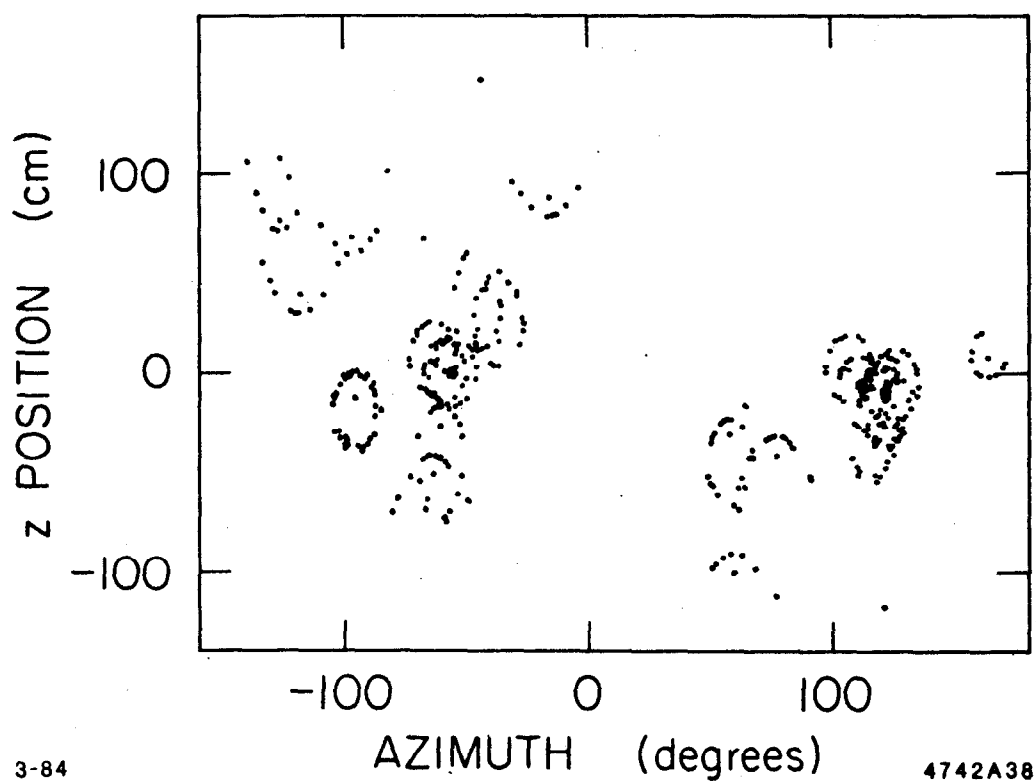
Figure 6.29.   Monte Carlo simulation of a $Z^\circ \rightarrow c\bar{c}$ event as seen by the barrel *CRID*. All measurement errors have been included. The event contains 26 charged particles.

truncated by total internal reflection as z becomes larger. The rings from the gas radiator are about 3 cm or less in radius and appear as point clusters on this scale.

Preliminary studies indicate that it will be relatively straightforward to recognize the Čerenkov rings, even in a dense jet environment.[10] Consider as an example a simple pattern recognition algorithm for the rings produced in the liquid radiator. The information from the central drift chamber helps determine the track parameters at the radiator. For each particle the photon emission point is taken as the center of the radiator. For all measured photoelectrons in the neighborhood, a Čerenkov angle is calculated and error estimated. Figure 6.30 shows the resulting reconstructed Čerenkov angle plots for the dense cluster of 12 tracks near 100° of the event in Figure 6.29. The liquid rings, with angles of about 38°, are clearly observed, although some background exists in the same bins. In one case, Figure 6.30(e), the particle is actually below liquid threshold. Proceeding with the pattern recognition, compare the reconstructed angle for each photon to that expected for each of the potential particle hypotheses, and take as a tentative hypothesis the one which gives the most points for a track. Finally, associate each photon with the single track hypothesis to which it is closest, excluding from consideration points that lie within an estimated four standard deviations of more than one track. As shown by the shaded areas in Figure 6.30, the patterns are now very clear and essentially background free.

6.4.5 Lepton Identification

The lepton identification of the *CRID* nicely complements the calorimeter tagging in the low momentum region, where the calorimeter does need some help. The separation between leptons and pions as a function of energy for both the Čerenkov counter and the calorimeter are shown in Figure 6.31. In the *SLD*, good e/π separation is provided over the full momentum range by combining information from the liquid argon calorimeter and the *CRID*. Because of the closeness of the μ and π masses, the μ/π separation range in the *CRIDs* is quite narrow. However, it helps to cover the low momentum region below 4 GeV/c where the calorimetry deteriorates. Therefore, the complete *SLD* system attains
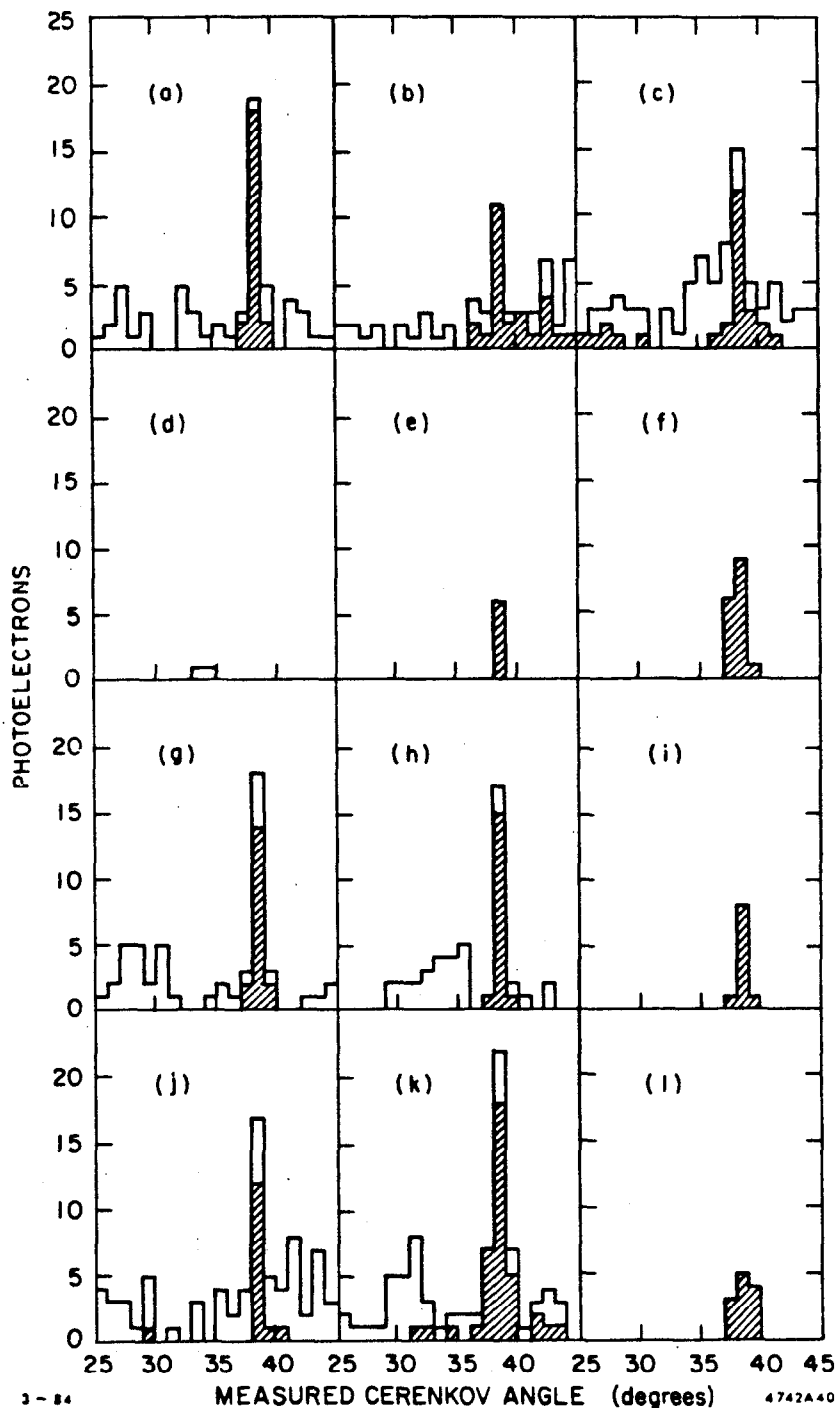
Figure 6.30. Histograms of the number of photoelectrons per bin versus the reconstructed Čerenkov angle for all observed photoelectrons in the vicinity of the 12 tracks in the positive azimuth jet near 100° of the event of Figure 6.29. The shaded areas have been associated with each track using the algorithm discussed in the text.
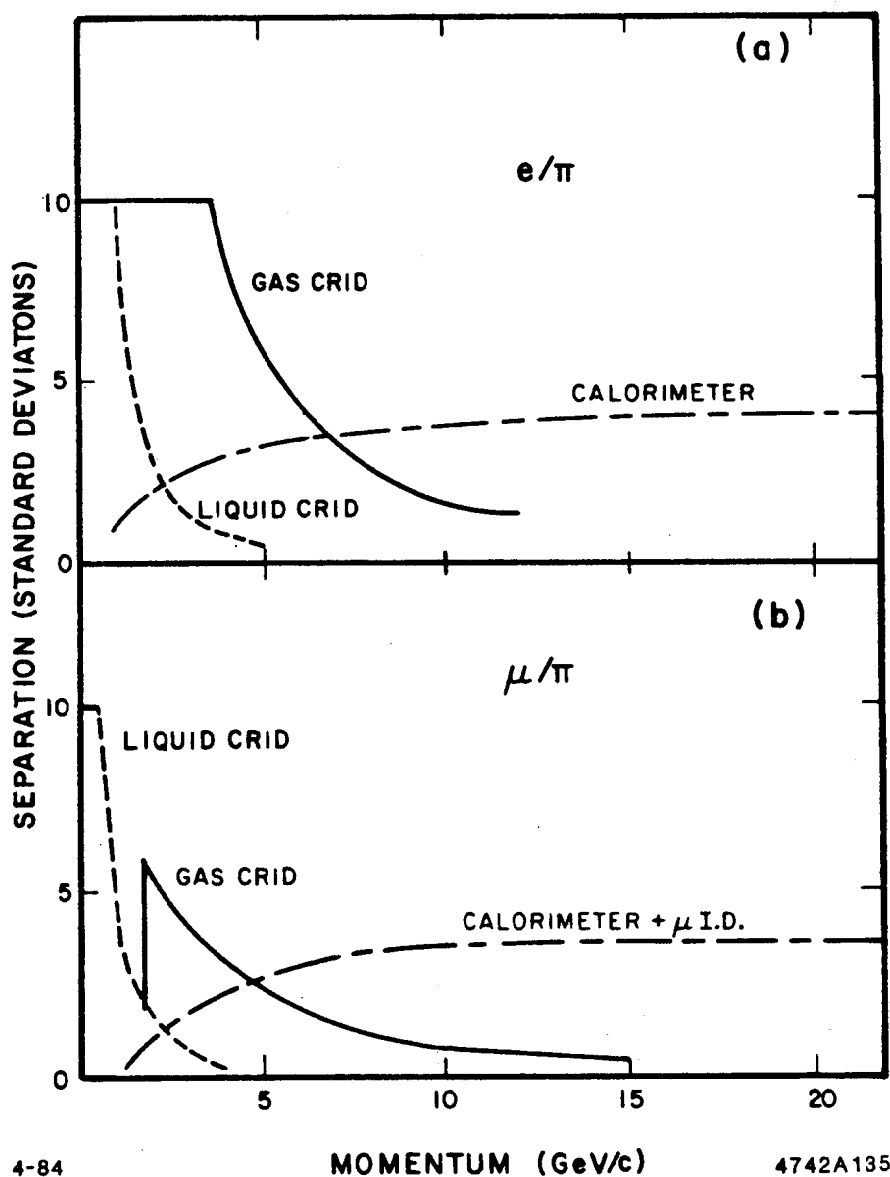
Figure 6.31. The lepton/hadron separation capability for the various components of the *SLD* versus momentum. The calorimetry separation curves assume equal particle populations and 80% efficiency for the wanted particle.

6 - 67

good μ/π separation over essentially the complete momentum range.

6.5 REFERENCES

1. B. Ratcliff, "*D* Meson Reconstruction at the Z^0," *SLD* Note No. 108.

2. A. Roberts, Nucl. Instrum. Methods <u>9</u>, 55 (1960).

3. J. Seguinot and T. Ypsilantis, Nucl. Instrum. Methods <u>142</u>, 377 (1977).

4. (a) *DELPHI: CERN/LEPC/83-3, LEPC/P* 2, 17 May 1983.

   (b) E-605: H. Glass et al., Nucl. Sci. Symp. 1982:30 (*IEEE* Trans. <u>*NS-30*</u>, No. 1, February 1983).

   (c) *LOGIC*: B. Barish et al., *CERN-LEP-LI-(6)*, January 1982, p. 28.

   (d) *OMEGA*: Bonn/Lancaster/Manchester/*RAL*/Sheffield. Proposal No. 231–Addendum 4, *PPESP/82/24*. M. Davenport et al., Nucl. Sci. Symp. 1982:30 (*IEEE* Trans. <u>*NS-30*</u>, No. 1, February 1983).

   (e) *UA-2: RICH* Collaboration (P. Baillon *et al.*), *CERN/SPSC/82-55*, January 1982.

   (f) *SLD*: R. Baltrusaitis et al., *SLC-LI-09*, 1982, p. 59.

5. T. Ypsilantis, Phys. Scr. <u>23</u> 371-376 (1981).

6. D. F. Anderson, *LA-UR-80-3158*.

7. Private communications from Peter Sharp, Rutherford Appleton Laboratory, and Tord Ekelof, *CERN* and Uppsala.

8. G. Charpak et al., Nucl. Instrum. Methods <u>164</u>, 419 (1979).

9. W. Dulinski and T. Ekelof, Nucl. Instrum. Methods <u>217</u>, 244-248, 1983.

10. *SLD* Note No. 74; *DELPHI* 82-32; *CERN/EP/COLLEPS* 82-11.